Master's thesis

NTNU
Norwegian University of Science and Technology
Faculty of Natural Sciences
Department of Materials Science and Engineering

Ingvild Eng Holck

Synthesis and Characterisation of the Plastic Crystal Solid Solution Systems $[(CH_3)_4N]_x[(CH_3CH_2)_4N]_{1-x}[FeBrCl_3]$ (x = 0.7 - 1)

Master's thesis in Nanotechnology
Supervisor: Prof. Mari-Ann Einarsrud
Co-supervisor: Dr. Julian Walker
June 2021

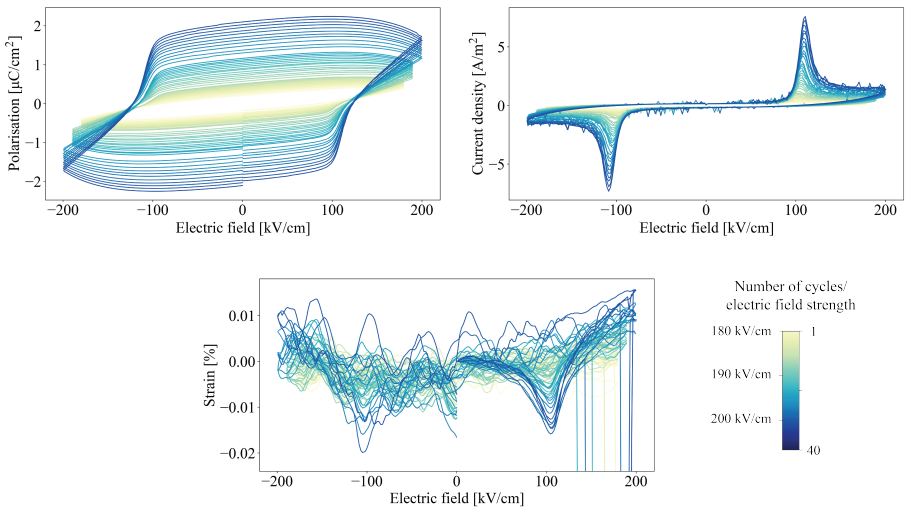

NTNU
Norwegian University of
Science and Technology

Ingvild Eng Holck

Synthesis and Characterisation of the Plastic Crystal Solid Solution Systems $[(CH_3)_4N]_x[(CH_3CH_2)_4N]_{1-x}[FeBrCl_3]$ (x = 0.7 - 1)

Master's thesis in Nanotechnology
Supervisor: Prof. Mari-Ann Einarsrud
Co-supervisor: Dr. Julian Walker
June 2021

Norwegian University of Science and Technology
Faculty of Natural Sciences
Department of Materials Science and Engineering

NTNU
Norwegian University of
Science and Technology

Preface

This project is written and submitted as part of the course *TMT4910 Nanotechnology, Master's Thesis* and is a continuation of the work done in *TMT4510 Nanotechnology, Specialisation Project*.[1] Experimental work was performed by the author (unless explicitly stated otherwise), under the supervision and co-supervision of Prof. Mari-Ann Einarsrud and Dr. Julian Walker.

All figures were made by the author using Adobe Illustrator unless otherwise specified.

Acknowledgements

I first wish to extend a big thank you to my supervisors, Mari-Ann Einarsrud and Julian Walker, without whom this Master's thesis would not have been possible. You have been wonderful supervisors the entire year, always answering my questions with great expertise and understanding, and continuing to keep me motivated and interested throughout all and any setbacks. I am immensely grateful! I would also like to thank the various people at the IMA labs took time out of their day to help me when I was having trouble with instruments, though most did not know who I was, only that I looked confused.

Thank you to my friends in Trondheim, who I have met during the last five years, which you made the best five years of my life. You have changed both my life and me (for the better, luckily) and I appreciate you all so much.

Last, but not least, I wish to thank my family. Thank you for always sticking by me and supporting me in everything I do. An extra thanks in particular to my parents, Haakon, and Fatbardha, for proofreading my thesis (and promptly falling asleep while doing so).

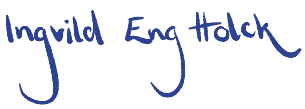

Ingvild Eng Holck
Trondheim, June 2021

Abstract

Ferroelectrics have through their reversible permanent polarisation found use in several avenues of technology, such as in digital memory, filters and sensors. Current standards are metal oxide ceramics, whose brittle nature and high processing temperatures impose hard restrictions on sustainability and development of new functional devices. Emerging as a solution are plastic crystal ferroics, in which a plastic mesophase at moderate temperatures enable low-temperature shaping and exploitation for flexible purposes. Tetramethylammonium and tetraethylammonium bromotrichlorferrate (III), $TMAFeBrCl_3$ and $TEAFeBrCl_3$, are plastic crystals with different cations (TMA^+ and TEA^+), but the same anion ($FeBrCl_3^-$). They both have polar structures, but only $TMAFeBrCl_3$ is ferroelectric, and together they form a system with great potential for solid substitution and tailoring of properties.

The aim of this thesis was to investigate this system further, through surveying the degree of solid solution formation and assessing ferroelectric properties. This was accomplished by synthesising six compositions of $TMA_xTEA_{1-x}FeBrCl_3$ in the range x = 0.7 - 1, via crystallisation from solution and annealing, followed by characterisation. The effect of the annealing step was first reviewed through imaging an structural analysis, which revealed that annealing gave a homogenisation of the crystal structure. Through X-ray diffraction, the Cmcm phase was found as the majority phase for all samples, and for samples with mol% TMA^+ between 97.5 and 90, it was the only phase. Above and below this, Amm2 and $P6_3mc$ respectively appeared as minority phases. From structural analysis as well as differential scanning calorimetry and dielectric measurements, a compositionally induced phase transition in the vicinity of the chemical composition of 90 mol% TMA^+ and 10 mol% TEA^+ is proposed. Hot pressing of powder samples gave only minor changes in phase composition, but showed evidence of structural texturing. High-field ferroelectric testing revealed that characteristic ferroelectric behaviour was present only in the samples with mol% TMA^+ equal to 100 and 97.5. The presence of ferroelectric behaviour in centrosymmetric, non-ferroelectric Cmcm was suggested to be the result of a field-induced transition into the ferroelectric Amm2 phase, and the lack of ferroelectricity in the remaining samples was hypothesised to be due to an increased barrier for this transition.

Sammendrag

Gjennom deres reversible permanente polarisering har ferroelektriske materialer funnet bruksområder innen flere grener av teknologi, som for eksempel digitalt minne, filtre eller sensorer. Dagens konvensjonelle ferroelektriske materialer er metalloksider, men deres sprø egenskaper og behov for prosessering ved høye temperaturer forhindrer utvikling av nye funksjonaliteter og vedlikeholder høye karbonutslipp. En mulig løsning finnes i plastiske ferroelektriske krystaller, der en plastisk mesofase ved moderate temperaturer åpner for bruk i fleksible applikasjoner og forming ved lave temperaturer. Tetrametylammonium- og tetraetylammonium-bromotrikloroferrat(III) ($TMAFeBrCl_3$ og $TEAFeBrCl_3$) har begge polare strukturer, men kun $TMAFeBrCl_3$ er ferroelektrisk. Sammen danner de et system med stort potensiale for fast oppløsning og skreddersying av egenskaper.

Målet med denne oppgaven var å undersøke dette systemet videre, gjennom kartlegging av grad av fast løsning samt utforsking av ferroelektriske egenskaper. Dette ble oppnådd ved å syntetisere seks komposisjoner av $TMA_xTEA_{1-x}FeBrCl_3$ med x = 0,7 - 1, som ble gjort via syntese i løsning og varmebehandling, etterfulgt av karakterisering. Effekten av varmebehandlingssteget ble undersøkt gjennom strukturell analyse og mikroskopi, som avslørte at varmebehandling ga en homogenisering av krystallstrukturen. Gjennom røntgendiffraksjon ble Cmcm-fasen funnet som majoritetsfasen for samtlige prøver, og det var dessuten eneste struktur tilstede i prøver med komposisjon mellom 90 og 97.5 mol% TMA^+. Over og under disse komposisjonene ble henholdsvis Amm2 og $P6_3mc$ separert ut som minoritetsfaser. Strukturanalyse samt termiske og dielektriske målinger indikerte at det i nærheten av en komposisjon på 90 mol% TMA^+ og 10 mol% TEA^+ ligger en faseovergang mellom enkeltfase- og dobbeltfasesystemer. Pressing av pulverprøver ga kun små endringer i fasesammensetning, men viste tegn på teksturering. Gjennom ferroelektrisk testing ved høye elektriske felt ble typisk ferroelektrisk karakteristikk funnet kun i prøver med mol% TMA^+ på 97.5 eller over. Tilstedeværelsen av ferroelektrisk oppførsel i den ikke-ferroelektriske Cmcm-krystallstrukturen ble foreslått å være en konsekvens av en felt-indusert faseovergang til den ferroelektriske Amm2-fasen. Videre ble mangelen på ferroelektrisitet i de gjenværende prøvene hypotetisert til å skyldes en økt energibarriere for denne typen faseovergang.

Contents

Figures

Tables

Abbreviations

BTO Barium titanate, $BaTiO_3$

cif crystallographic information file

DSC differential scanning calorimetry

GOF goodness of fit

MPB morphotropic phase boundary

PZT lead zirconate titanate, $Pb[Zr_xTi_{1-x}]O_3$

SEM scanning electron microscopy

TEA^+ tetraethyammonium cation

TEABr tetraethyammonium bromide

$TEAFeBrCl_3$ tetraethylammonium bromotrichloroferrate(III), $[(CH_3CH_2)_4N][FeBrCl_3]$

TMA^+ tetramethyammonium cation

$TMA_xTEA_{1-x}FeBrCl_3$ tetramethylammonium tetraethylammonium bromotrichloroferrate(III), $[(CH_3)_4N]_x[(CH_3CH_2)_4N]_{1-x}FeBrCl_3$

TMABr tetramethyammonium bromide

$TMAFeBrCl_3$ tetramethylammonium bromotrichloroferrate(III), $[(CH_3)_4N][FeBrCl_3]$

XRD X-ray diffraction

Chapter 1

Background

1.1 Motivation

In the first century since its discovery in the Rochelle salt by Valasek,[2] ferroelectricity has shaped the lives of nearly all humans. By virtue of their reversible permanent polarisation,[3] ferroelectric materials have become an integral part of the hallmark of modern living, namely electronics. The functional properties make ferroelectrics viable for a range of technologies, be they microphones, digital memory or mobile phones. Dominating the current day ferroelectrics market are metal oxide ceramics whose ferroelectric properties were discovered already during the 1940s[4] and 50s,[5,6] barium titanate ($BaTiO_3$, BTO) and lead zirconate titanate ($Pb[Zr_xTi_{1-x}]O_3$, PZT). Initially regarded as pioneer materials, several limitations of these ceramics are now surfacing as society calls for increased functionality, but also sustainability as the ramifications of consumerism are becoming known. In lieu of metal oxide ceramics, replacements must be found to meet the progressively more rigorous demands.

Metal oxide ceramics are hard, brittle materials, averse to use for flexible purposes and requiring immense amounts of energy for production due to high processing temperatures. To achieve the range of functionality required by society, doping with foreign elements such as rare-earth metals is often required, but in doing so the potential for recycling is substantially reduced. Such an increase in elemental footprint, meaning the number of elements used in a compound, limits the degree to which the compound can be recycled, due to the complex and exact blend of elements needed to achieve certain functionalities.[7] Large elemental footprints are also associated with high energy consumption and problematic ethical dilemmas, in particular with relation to mining. As the electronics industry is looking to reduce its carbon footprint yet increase the functionalities of devices, metal oxide ceramics therefore fall short. Thus, new materials fulfilling these requirements while maintaining a performance on par with that of BTO and PZT must be uncovered. A rising contender is found in plastic crystal ferroics.

Plastic crystals are materials with a plastic mesophase between the solid crystalline and liquid phases. The phase is reached at moderate temperatures and with it comes benefits such as malleability and pliability, enabling straightforward processing and shaping of plastic crystals at much lower temperatures than for metal oxide ceramics. The plastic mesophase comes about due to

globular molecules in the lattice structure, capable of rotating at their fixed lattice site to create local disorder while maintaining the long-range order of the material as a whole. An added benefit of plastic crystals can be realised through crystal engineering, where the replacement of chemical species form the basis for tailoring of properties. By utilising variations on the same chemical species in these substitutions, foreign element dopants can be completely avoided and thus functionality without the expense of high elemental footprints or reduced reusability can be achieved. Several plastic crystals also have ferroelectric properties. There are several potential avenues for the use of these plastic crystal ferroics, such as in flexible energy harvesters,[8–10] microelectromechanical systems (MEMS)[8] and sensors.[10,11]

An example of a plastic crystal is found in the organic-inorganic supramolecular compound tetramethylammonium bromotrichloroferrate(III) ($[(CH_3)_4N][FeBrCl_3]$, $TMAFeBrCl_3$). After initial studies performed by Harada et al.,[12] the material is now garnering interest as an emerging candidate for ferroelectric purposes, due to its pertinent electrical properties, in particular a strong piezoelectric coefficient yet low dielectric constant.[12,13] With its five polymorphs, two of which are ferroelectric, $TMAFeBrCl_3$ can be processed in the plastic mesophase at moderate temperatures, yet possess ferroelectric properties at room temperatures. The compound can easily be synthesised through aqueous synthesis using dehydration.[12]

Tetraethylammonium bromotrichloroferrate(III) ($[(CH_3CH_2)_4N][FeBrCl_3]$, $TEAFeBrCl_3$) is also a plastic crystal compound, but with a non-ferroelectric crystal structure.[14] The compound is nevertheless piezoelectric, and the similarity of its chemical species with those of $TMAFeBrCl_3$ sets the stage for a potential solid solution system where properties can be altered with no increase in elemental footprint. Previous studies performed on this tetramethylammonium tetraethylammonium bromotrichloroferrate(III) ($TMA_xTEA_{1-x}FeBrCl_3$) system showed phase separation and lacking ferroelectricity for the majority of the compositional range.[15]

Ferroelectric materials used in industry are usually tailored to suit specific applications and it is therefore crucial to build knowledge of how to do this with plastic crystals, as the approaches might deviate from the conventional methods for metal oxides. Though plastic crystals are emerging as potential ferroelectric materials with many beneficial characteristics, there are currently no clear property development strategies for engineering towards different applications and tailoring of properties. This study therefore explores compositional engineering as a property tailoring method for plastic crystal development and investigates both synthesis and characterisation as a function of chemical composition, thus showing that it is possible to use a solid solution approach.

1.2 Aim

There are two main objectives of this study: To investigate the effect of a thermal processing step in the synthesis on the product's structural composition, and to characterise the electrical properties of the products from this synthesis. Six chemical compositions containing a majority of $TMAFeBrCl_3$ will be investigated. Previous studies[1] indicate that a solid solution should be achievable in this compositional range after a heat treatment, and though a study of the full compositional range[15] found ferroelectric behaviour to not be present at any mixed composition $TMA_xTEA_{1-x}FeBrCl_3$, the production of a solid solution could potentially change this.

To achieve these aims, six crystal compositions are synthesised and investigated using X-ray diffraction (XRD) and differential scanning calorimetry (DSC) to ascertain if they are solid solutions. A substudy on the effect of the annealing step on particle morphology is also performed via scanning electron microscopy (SEM) imaging. Lastly, dielectric spectroscopy and high-field ferroelectric testing are used to determine electrical properties. If a solid solution with favourable ferroelectric properties can be achieved, we are one step closer to realising the full potential of plastic crystal ferroics through crystal engineering.

Chapter 2

Introduction

This thesis details the synthesis and characterisation of the $TMA_xTEA_{1-x}FeBrCl_3$ plastic crystal system. This system is investigated in the hopes of finding a compositional region of a solid solution with favourable electrical properties. Therefore, there are several topics important for the understanding of the following discussion. The introduction first delves into topics such as synthesis, processing and design of crystals. Subsequently it gives a brief presentation of ferroelectricity and ferroelectric properties, plastic crystals and last the $TMA_xTEA_{1-x}FeBrCl_3$ system.

2.1 Crystal synthesis, processing and design

2.1.1 Crystallisation

The crystals in this thesis are synthesised through crystallisation from solution. Crystallisation is the organisation of ions or molecules into highly ordered and symmetric arrangements. When crystallisation happens from liquid solution, solvated ions go from high-energy disordered states to low-energy ordered states in the crystal structure. The driving force for this process is often the solution being in a state of *supersaturation*, with a higher concentration of dissolved solute than at the equilibrium concentration. Supersaturation can be achieved by decreasing the temperature of the solution or by increasing the concentration of solute, e.g. by evaporating solvent or carefully adding solute.[16] In a supersaturated system, ions will cluster together in nuclei (*nucleation*) to minimize the system energy. These nuclei form the basis for further growth until a solid phase is established. The rate of nucleation and growth both depend on the degree of supersaturation and will affect properties of the resulting solid state particles, such as morphology and size distribution.[17,18] With increasing growth rate and supersaturation, particles go from clearly faceted to dendritic surface structures. Dendrites usually form in the early stages of crystallisation, but the structure is often eradicated at later growth stages in favour of more uniform structures, unless the supersaturation is high enough or the structure is favoured by the material.[19]

2.1.2 Diffusion and solid state reactions

In this project, thermal treatments will be used to drive chemical homogenisation of materials through solid state diffusion. Therefore a basic introduction to diffusion will follow. Diffusion describes the motion of atoms, ions and molecules influenced by a driving force, which more often than not is a concentration gradient.[20] The concentration in a solid will often vary throughout the substance, causing what is known as *non-steady-state* conditions of diffusion. The diffusion is then described by *Fick's second law*:

$$\frac{dc_x}{dt} = D^* \frac{d^2 c_x}{dx^2} \tag{2.1}$$

where c_x is the concentration of diffusing species at a distance x from an origin after a time t and D is the *diffusion coefficient*. The diffusion coefficient details the velocity of the diffusing species and is therefore an essential parameter when reporting on diffusion. When the concentration of diffusing species contrarily remains constant at any point x in the substance, the diffusion is termed *steady-state diffusion*. Under these conditions, the diffusion coefficient is obtained from *Fick's first law*,

$$J_i = -D_i \frac{dc_i}{dx} \tag{2.2}$$

where D_i is the diffusion coefficient for species i, x is the position in the solid and c_i is the concentration of species i. J_i is the flux of the species, meaning the net flow through the solid.[20]

When diffusion happens through the body of the solid, it is known as *volume diffusion*. However, diffusion is also possible along dislocations such as surfaces and interfaces between phases. Owing to the discontinuous nature of the crystal structures in these regions, diffusion is often quicker along these paths than through the bulk. Diffusion is generally very slow at room temperature, but can be increased through modification of external parameters, such as raising the temperature.[20]

Solid state reactions are reactions where reagents and product are all in the solid state and no liquid needs be involved in the process.[21] The process involves mixing of the reagents, possibly pressing them together, and heating the mixture at elevated temperatures. Such reactions utilise the diffusion happening at high temperatures to homogenise the material. Chemical gradients in a mixture of two or more solids will cause diffusion across interfaces, using minimisation of energy to drive mass transport of atomic species. There is a chemical reaction due to a decrease in free energy, and a single, homogeneous product is achieved. Several factors influence the properties of the product, such as the reagent mixing, the reaction environment and temperature.[21]

2.1.3 Solid solutions and crystal engineering

This project investigates the formation of solid solutions in $TMA_xTEA_{1-x}FeBrCl_3$, and is an example of crystal engineering. If a molecule or ion can substitute other molecules or ions in a crystal structure, all while retaining the original structure, then the resulting material is a solid solution.[22] Solid solutions differentiate themselves from ordinary mixtures in that there is only *one* structure present, while in a mixture the original components conserve their identity. A divide can be made between *substitutional* and *interstitial* solid solutions, where the former involves the direct replacement of ions in a structure while the latter entails the addition of small atoms or ions into interstitial sites in the original structure. Substitutional solid solutions are most easily formed

when the molecules or ions have similar properties, in particular comparable size and valence. The degree of substitutional solid solutions varies, from *complete* or *continuous solid solutions* where a molecule or ion can completely replace another without causing structural changes, to systems where the components have only limited solubility in each other. The latter is most common, and limits of miscibility will be determined by factors such as size of molecules/ions or correspondence between crystal structures of the end members.[22]

Crystal engineering concerns itself with the design, synthesis and adaptation of crystals and their properties with the aim of optimising the physical and chemical properties for a various purposes.[23,24] Early crystal engineering studies were often directed towards the use of single component molecular structures and alteration of properties through discrete substitutions of building blocks. However, this limits the range of attainable properties. Solid solutions can offer more control through meticulous variations in stoichiometry, and therefore also a continuous spectrum of properties between those of the two end members.[23]

2.2 Introduction to dielectrics and ferroelectrics

The $TMA_xTEA_{1-x}FeBrCl_3$ system is explored with the purpose of finding a solid solution with beneficial ferroelectrical properties for use in industry. Therefore, this section covers relevant topics for the understanding of ferroelectricity, starting with dielectrics and electric polarisation and ending with a definition ferroelectricity and ferroelectric properties.

2.2.1 Dielectrics and electric polarisation

Dielectrics are electrically insulating materials with significant industrial importance in the electronics industry in devices such as capacitors.[25] In dielectrics, outer electrons are bound, inhibiting movement and consequently current flow through the material.[26] However, when exposed to an external field E, negatively and positively charged species in a dielectric will experience oppositely directed forces, resulting in a displacement of these charged species. Two oppositely charged species separated in space together make up a single dipole, and many dipoles present in a material gives rise to a polarisation P of the material, proportional to the field, E.[26]

Dielectrics and their ability to be polarised are described by the dielectric constant of the material, ϵ_r. Also known as the relative permittivity, this quantity is material specific and describes the permittivity of the material relative to that of vacuum, $\epsilon_0 = 8.854\text{x}10^{-12}$ Fm^{-1}.[27] With application of a static external field to a dielectric, polarisation arises and the material can store electrical charge. The dielectric constant is then an important parameter for describing a material's charge storage ability, namely its capacitance C, given as

$$C = \frac{\epsilon_0 \epsilon_r A}{d} \tag{2.3}$$

for a flat material of thickness d with electrodes of area A.

Upon application of an oscillating electric field $E = E_0 \cos\omega t$, where E_0 is independent of the frequency ω, there will be a phase lag δ between applied field and induced polarisation.[27,28] The generation of dipole moment is not instantaneous even when applying a static electric field, but will rather develop at a rate depending on type of charges present. The system will require time to achieve equilibrium with the applied field (formally this time is infinity), but if the field is switched before such equilibrium is obtained, the polarisation never reaches the static value. The dielectric constant also has a frequency dependence and is better described as a complex quantity,

$$\epsilon = \epsilon' + i\epsilon'' \tag{2.4}$$

where ϵ' is the real permittivity describing the component of the polarisation P in phase with E and ϵ'' is the imaginary permittivity, defining the 90° out-of-phase component.[27,28] While ϵ' determines the net separation of charge in the dielectric, ϵ'' is proportional to the energy loss of the dielectric. Work performed by the electric field to establish the dipole moment is either stored in charge separations or used to overcome the friction associated with dipole moment generation. The latter of these is not recoverable, meaning there is an energy loss associated with the dielectric.[27,29] The loss tangent tanδ is often used to describe the energy loss, given as

$$\tan\delta = \frac{\epsilon''}{\epsilon'}. \tag{2.5}$$

where δ is the phase lag, as mentioned above.[28]

The dielectric constant is influenced by the polarisation mechanisms present in the material at the given temperature and frequency, as evident from Figure 2.1. There are four mechanisms, where the first, *electronic* polarisability, is present in all materials and originates in the perturbation of the electron cloud relative to the nucleus of the atom. The remaining three occur in materials depending on the nature of their constituents. *Ionic* polarisability occurs in dielectrics due to displacement of ions whereas *dipolar* polarisability originates in the re-orientation of permanent dipoles. Also possible is *space charge* polarisability, if there are mobile charge carriers in the material.[26,29] These

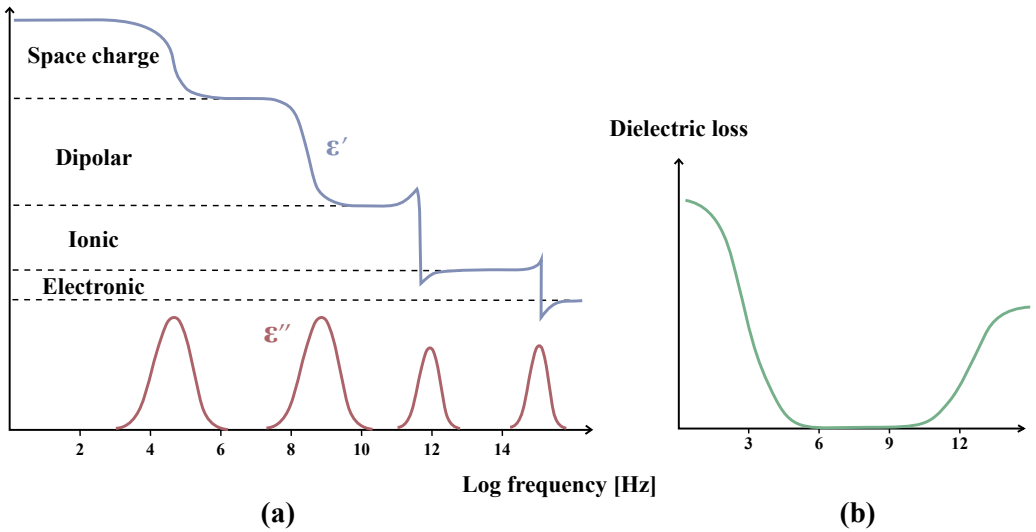

Figure 2.1: (a) Schematic of the frequency dependence of the real and imaginary relative permittivities. Different contributing polarisability mechanisms are included. ϵ' and ϵ'' behaviours are in blue and red, respectively. (b) Schematic of the frequency dependence of the dielectric loss behaviour. Both adapted from [29].

mechanisms do not all contribute equally over the entire frequency range, and at sufficiently high frequencies none are able to keep up with the applied field. In this region, the loss in dielectric permittivity is coupled to an increase in loss tangent, as seen in Figure 2.1 (a) and (b). Most of the low-frequency losses originate in conduction and space charge effects.[29]

2.2.2 Ferroelectric material properties

Crystal structures belong to one of seven categories: triclinic, monoclinic, orthorhombic, tetragonal, trigonal, hexagonal and cubic (listed in order of ascending symmetry). A further division sees crystal structures divided into one of 32 possible *crystal classes* or *point groups* based on their point symmetries.[3] The subcategories of these 32 classes are illustrated in Figure 2.2. Of the 32 classes, 11 possess a centre of symmetry, making them *centrosymmetric*. Conversely, the remaining 21 classes do not, and all but one of these *non-centrosymmetric* structures display electric polarisation when exposed to external stress, more commonly known as the *piezoelectric effect*. Piezoelectric structures can further be divided into two groups based on whether or not they possess a unique polar axis. 10 out of 20 structures do, and these are consequently known as *polar*, as they have a generally temperature-dependent *spontaneous polarisation*. Owing to this temperature-dependence, these structures are also known as *pyroelectric*, exhibiting the *pyroelectric effect* in which temperature changes generate polarisation in the material.[3]

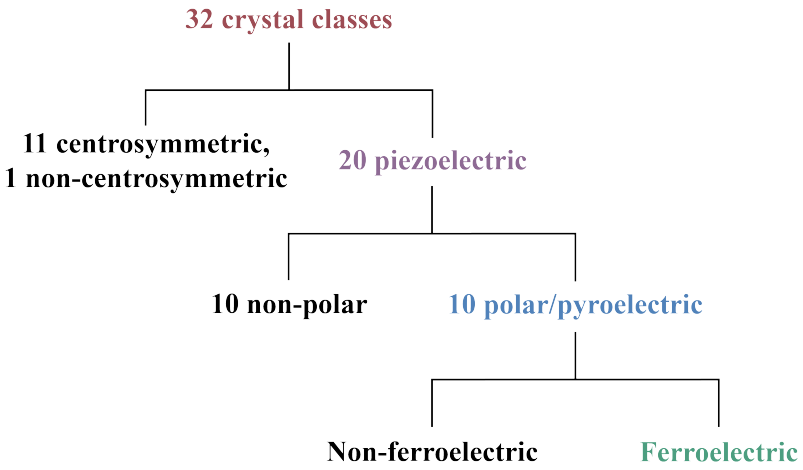

Figure 2.2: Overview of how the 32 crystal classes can be divided into piezo-, pyro- and ferroelectric structures.

Ferroelectric materials are yet another subgroup, differentiating themselves from pyroelectric materials with the switchability of their spontaneous polarisation. These materials have two or more discrete, orientational states, and through application of an electric field, the material can switch between them. This is made possible through the coupling of the field to the polarisation, which alters the relative energy of the states.[30] Furthermore, when the applied electric field is removed, a ferroelectric material will retain its polarisation, whereas pyroelectric materials do not. The cause of ferroelectricity is the breaking of the symmetric environment by the polar displacement of atoms in the unit cell; The ferroelectric crystal structure can in theory be obtained as a small distortion of a high-symmetry reference phase.[30]

Ferroelectric phase transitions and domain structure

Ferroelectric materials usually have a spontaneous polarisation P_s which will decrease when increasing the temperature, until a cricitcal point is reached, at which the polarisation vanishes completely.[3] This point is called the *Curie temperature* T_c and marks the location for the ferroelectric phase transition. Above T_c, the material is in what is known as the *paraelectric phase*, where there is no spontaneous polarisation since the crystal is centrosymmetric.[26] Below T_c, on the other hand, two or more directions appear where spontaneous polarisation can develop, now accessible due to the breaking of the crystal symmetry with reduced temperature. Figure 2.3 illustrates the perovskite ABO_3 structure, where a distortion of only the central ion would result in polarisation. However, this ionic motion is in this material also followed by an elongation of the unit cell and macroscopic dimensional changes for the material as a whole.[31] Examples of such perovskite ferroelectric structures are PZT, where the paraelectric phase is cubic and one of the ferroelectric phases is tetragonal, as illustrated in the figure. PZT will be discussed more thoroughly in a later subsection.

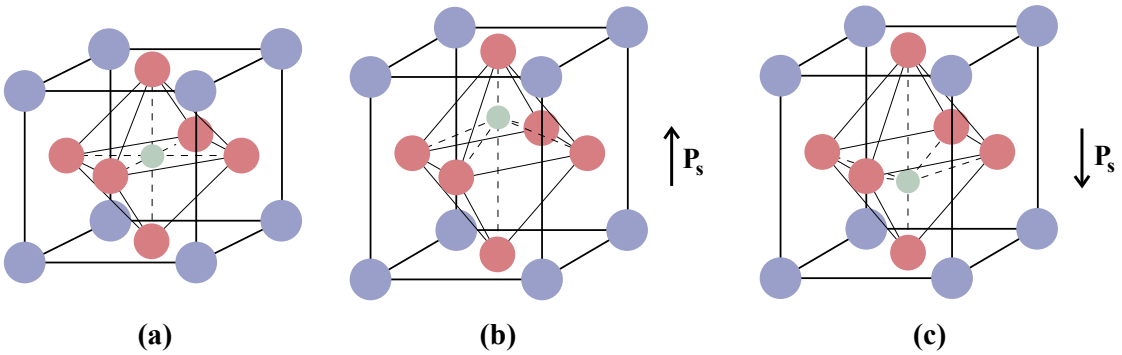

Figure 2.3: Perovskite ABO_3 unit cells in the (a) paraelectric cubic phase and (b), (c) ferroelectric, tetragonal phases. (b) and (c) illustrate two of the six different polarisation directions, possible[31] where switching between the two would require only the application of an electric field in the desired direction of polarisation. Adapted from Figures 4.4 in [32] and 3 in [31].

When a dielectric material is polarised, bound charges appear at the surface of the material, ultimately leading to an internal electric field opposing the spontaneous polarisation.[3,33] This field, known as the *depolarising field*, must be screened for spontaneous polarisation and thus ferroelectricity to be sustained in the material, which can be done through the formation of *ferroelectric domains*. The polarisation will be uniform inside a single domain, but different from neighbouring domains, which ultimately decreases the depolarising field of the material as a whole. Sectioning off the domains are interfaces called *domain walls*, that induce stray fields leading to an increase in the system energy. Therefore, the final domain structure of the material will be that which best minimises the total energy contributions from depolarising fields and stray fields alike.[33] Materials exhibiting this intricate domain structure are known as *ferroics*, and due to energy concerns, they are more common than those maintaining a single, uniform domain throughout the material. A ferroic material will occur naturally with domains arranged such that the overall polarisation is zero or close by.[26]

2.2.3 Field-dependent behaviour

A principal distinguishing feature of ferroelectrics is the reversibility of their spontaneous polarisation. This attribute gives rise to a characteristic behaviour of the ferroelectric material when exposed to alternating electric fields, known as *hysteresis behaviour*.[3,26,32] Several parameters exhibit hysteresis upon variation of the electric field, such as polarisation, current density and strain.

Polarisation-electric field hysteresis

Figure 2.4 (a) shows a typical hysteresis loop of a ferroelectric material together with the behaviour of a typical dielectric with conductivity loss. An ideal linear lossless dielectric would here have only a linear dependence on the electric field with no remaining polarisation when the applied field is zero. However, in a realistic dielectric, this is not the case as the material will experience losses due to e.g. leakage current.[3,34] Ferroelectrics, on the other hand, will give a non-linear response like the one shown in Figure 2.4.

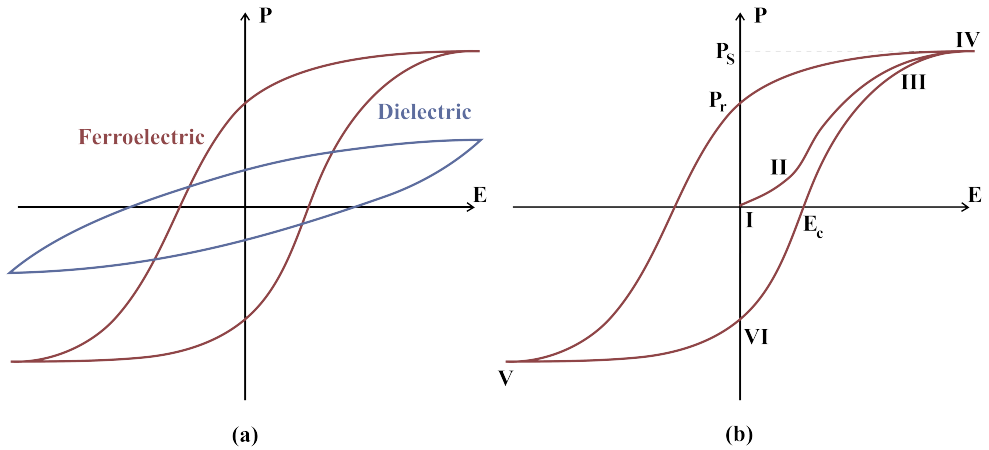

Figure 2.4: Hysteresis curves of ferroelectric materials. (a) Typical hysteresis curve of a ferroelectric material together with the curve of a leaky dielectric. (b) Ferroelectric hysteresis curve annotated with important parameters P_s, P_r and E_c. Adapted from Figures 4.9 and 4.10 in [3] and Figure 11.17 in [26].

Figure 2.4 (b) illustrates the hysteresis loop annotated with important parameters and stages. At zero applied field, a ferroelectric crystal boasts only negligible overall polarisation, since the various domains are oriented such that they cancel each other. However, upon applying an electric field, the material behaves first like a normal dielectric, with a small increase in polarisation (**I**-**II**). As **I** is reached, so is the field required for the domains to be able to switch between polarisation directions. From **II** to **III** the domains increasingly orient themselves in the same direction and yield a rapid growth of polarisation. After a while, all domains are aligned (**III**-**IV**) and the polarisation is "saturated". If conversely the field is reduced, the dipoles will start switching orientations. At zero field the polarisation is now non-zero, instead a certain field in the opposite direction is required to bring it down to zero. By continued increase of the oppositely directed field, the polarisation once again is saturated (**V**), but this time with domains pointing the other way. Reversal of the field leads back to zero polarisation through **VI**, before arrival at **IV**. Important parameters are the remanent polarisation P_r defining the polarisation left at zero field, the coercive field E_c defining the field necessary to decrease polarisation to zero and the spontaneous

polarisation P_s, the intercept of the extrapolated curve from **III**-**IV** with the polarisation axis. It should be noted, however, that for polycrystalline materials, P_s should be called the *saturation* polarisation, since the true spontaneous polarisation corresponding to a single domain can never be fully achieved.

The behaviour of the current density of a ferroelectric material upon application of an external field also exhibits hysteresis, illustrated in Figure 2.5 (a). Seeing as the current density J can be defined as $J = dP/dt$, the hysteresis loop is closely related to that of the polarisation, with peaks at the locations indicated by the coercive field E_c. These peaks give the maximum (in absolute value) current density values, J_{peak}.[35]

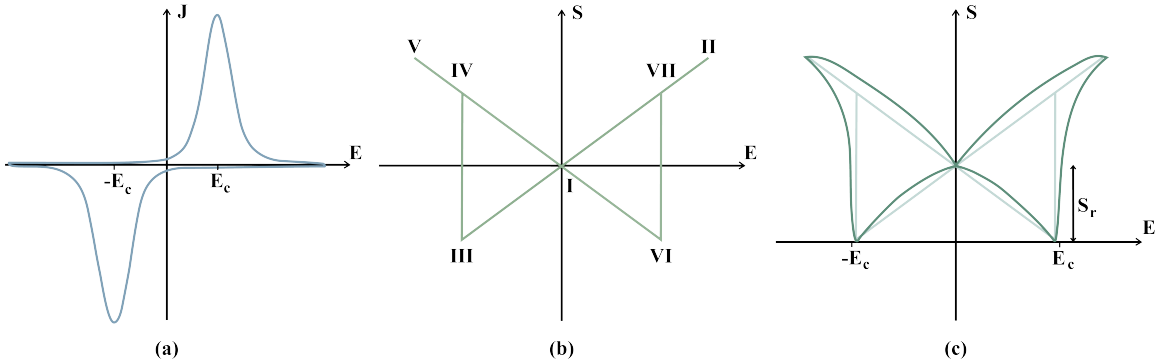

Figure 2.5: J-E and S-E hysteresis curves of ferroelectric materials. (a) Current density vs electric field, peaks marked by ± E_c. Adapted from [35]. (b) Idealised strain vs electric field curve, the so-called "butterfly curve". Adapted from Figure 11 (a) [32]. (c) A more realistic butterfly curve with residual strain S_r after the field is removed.

Strain-electric field hysteresis

Polarisation reversal in a ferroelectric material due to an applied electric field also induces strain-electric field hysteresis. This is caused by the piezoelectric effect, previously discussed, but is also a result of domain wall motion and switching.[32] An idealised strain-electric field hysteresis curve can be seen in Figure 2.5 (b). Starting in point **I**, the application of an electric field parallel with the spontaneous polarisation will lead to linear increase of the strain. The expansion of the crystal will continue so until the maximum field is reached (**II**) and also decrease linearly back to zero. Upon flipping of the field to the opposite direction, the strain will at first decrease linearly as well, until the field reaches a magnitude sufficient for switching the direction of the polarisation. The strain then becomes positive, moving from **III** to **IV**, as the polarisation is once again parallel with the applied field. It will continue its linear increase with increasing field, until reaching the maximum value at **V**. When the field once more is reduced, the strain returns through a linear path to **I**. After this, the strain will follow a similar, mirrored path to the **I**-**III**-**IV** path when the field direction is switched once more (**I**-**VI**-**VII**). The observed linear portion of the strain is produced by the piezoelectric effect.[32]

The idealised strain loop in Figure 2.5 (b), commonly styled the "butterfly loop" is not observed experimentally and is too simplified to properly describe the intricate relationship between strain and applied field. The loop in (c) is on the other hand more realistic. This is because the loop in (b) assumes a monodomain crystal able to be switched in 180°. Ceramic samples often contain multiple domains, where a number can be non-180°. The switching of polarisation direction in

III-**IV** and **VI**-**VII** in real materials is then far from as abrupt as in the idealised material, since the coercive fields of the various domains can vary. It is also possible to observe residual strain after removal of the applied field, if domains do not all switch back to their original positions.[32] It should be noted that the locations of the minima of the strain in the butterfly loop do not necessarily coincide with the coercive field, E_c,[36] yet the field at the stress minima is often taken as an approximation of E_c.[37]

2.2.4 PZT and the morphotropic phase boundary

Perovskite oxides are the most studied family of ferroelectric oxides, and includes ferroelectric giants such as BTO and PZT.[30,38] The family of oxides with composition ABO_3 (illustrated in Figure 2.3) readily forms solid solutions with good miscibilities, opening for great potential for tailoring of properties. Notably, isolectronic substitutions, such as exchanging Ba^{2+} with Sr^{2+} in BTO and Zr^{4+} with Ti^{4+} in $PbZrO_3$, are of particular interest due to the resulting array of insulating materials with shifts in transition temperatures and phase compositions, as well as excellent dielectric and piezoelectric properties.[30]

The PZT solid solution system is one of the most comprehensively researched and technologically important perovskite systems. The antipodes of the phase diagram consist of respectively $PbTiO_3$ and $PbZrO_3$, with drastically different electrical properties. The former is a ferroelectric material initially thought of as a less complicated version of the isomorphic BTO, whereas the latter is antiferroelectric, meaning the dipoles in this material orient themselves in an antiparallel fashion yielding a macroscopic spontaneous polarisation equal to zero.[3] The exchange of Zr^{4+} with Ti^{4+} quickly destabilises the structure which separates into two rhombohedral phases displaying ferroelectric properties already at only 5 mol% $PbTiO_3$. The Ti-rich phase has a tetragonal ferroelectric structure dominating the majority of the high Ti-content part of the phase diagram. An appealing attribute of the solid solution system is the consistently high Curie temperatures across compositions. At approximately 235 °C and 490 °C for $PbZrO_3$ and $PbTiO_3$, respectively, these temperatures form the limits of the Curie temperature for a given composition and open for a wide and high range of operating temperatures.[36,38,39]

The most interesting part of the PZT phase diagram is the near vertical line at 48/52 $PbTiO_3$/$PbZrO_3$ between the ferroelectric rhombohedral and tetragonal phases, known as a *morphotropic phase boundary* (MPB). The MPB is evidently almost independent of temperature, and in its close vicinity several parameters such as piezoelectric coefficients and dielectric permittivity reach a peak in value that persists over large temperature ranges.[32,39] In this region, piezoelectric coefficients are reported between 50-500 pC/N, depending on exact composition.[38] The presence of the MPB is of particular practicality as in this region, transition between the rhombohedral and tetragonal phases is easily achieved by application of an electric field. The domains are here easily switched between the 14 available orientational states. Importantly, this switching is equally simple between rhombohedral and tetragonal states alike, as the free energy of the corresponding phases are equivalent at the MPB. This ease of domain switching causes a maximum in the remanent polarisation of the material close to, but not at, the MPB.[3,32,39] The MPB is defined as a region where the rhombohedral and tetragonal phases coexist (with a small extension from the exact location of the boundary), but more recent studies suggest there in reality exists a monoclinic phase acting as a bridge between the rhombohedral and tetragonal ones.[40–42]

2.3 Plastic crystals

In 1935, Timmermans performed a study of the heat of fusion of several organic compounds, which triggered scientific interest and ultimately resulted in a new class of crystals.[43] By 1961, several contributions had lead to the discovery of the now known *plastic crystals*, compounds of unusually low entropies of melting and fairly high melting points.[44] Plastic crystals have what is known as a plastic mesophase, a hybrid phase between the liquid and solid states, as illustrated in Figure 2.6. When in the solid, crystalline phase, molecules can only vibrate about their equilibrium positions in the lattice, but when the material is in the plastic mesophase, the molecules also gain rotational freedom. Though their centres of mass must stay rooted at lattice positions, the molecules can now rotate in place, generating short-range disorder that does not come at the expense of the bulk crystal's long-range order. This increase in freedom is observed macroscopically in the high entropies of transition accompanying the transition from solid state to plastic mesophase. When the material later, at even higher temperatures, goes into the liquid phase, the entropy of melting is smaller for plastic than for non-plastic crystals, as the molecular species of former already have rotational freedom, while those of the latter do not.[44]

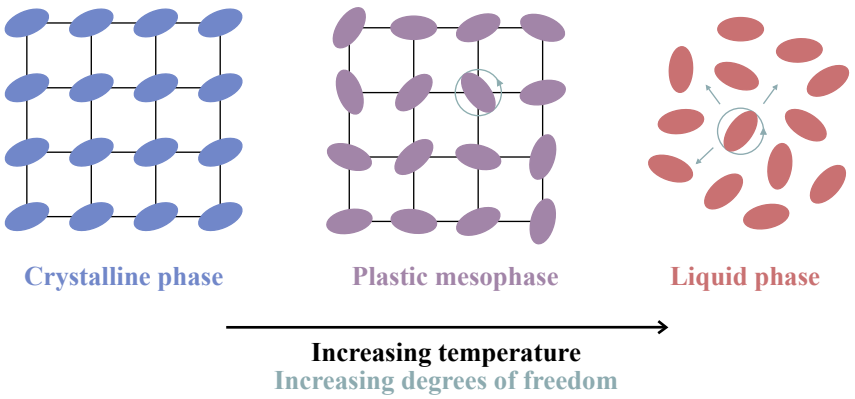

Figure 2.6: Schematic of the transition from solid to liquid phase for a plastic crystal, through the plastic mesophase. With increasing temperature, molecular moieties acquire the ability to first rotate in the mesophase, then move about each other in the liquid phase. The degrees of freedom are visualised with grey arrows. Adapted from [45].

Plastic crystals consist of globular constituents that are either symmetric about their centres or occupy spheres upon rotation.[44,46] These molecular species take up more space than they would were they not globular, which leads to weaker forces between them. Furthermore, this is a reason for the cubic structures found in the majority of plastic crystals, where dislocation slip planes are found in ample numbers, causing the plasticity that is the namesake of the plastic crystals. If all the globular molecules making up the crystal lattice are the same, the plastic crystal is called *simple molecular*. Another possibility is *ionic* plastic crystals, where distinct anions and cations make up the lattice. An important divergence between the two types of plastic crystals appears in their entropy of melting, as molecular plastic crystals have a low entropy of melting,[44,47] whereas ionic plastic crystals can exhibit significantly higher values.[48] This is the case when one of the constituent ions has considerably restricted rotation, since this entails the introduction of rotational freedom also at melting and not only at the transition to the plastic mesophase.

2.4 The $TMAFeBrCl_3$ and $TEAFeBrCl_3$ systems

The $TMA_xTEA_{1-x}FeBrCl_3$ system was chosen for investigation in this study because the constituent molecules are made up of the same atoms, thus complicating the elemental composition by introduction of foreign elements can be avoided. Differentiated only by the length of their cations' alkyl chains, as illustrated in Figure 2.7, the tetramethylammonium (TMA^+) and tetraethylammonium (TEA^+) cations make crystal structures with distinctly different properties when combined with the bromotrichloroferrate ($FeBrCl_3^-$) anion. Yet a similarity of the resulting crystal structures is that they are both polar. This makes the combination of both molecules in the $TMA_xTEA_{1-x}FeBrCl_3$ solid solution system an apt candidate in the search for new plastic crystal ferroics.

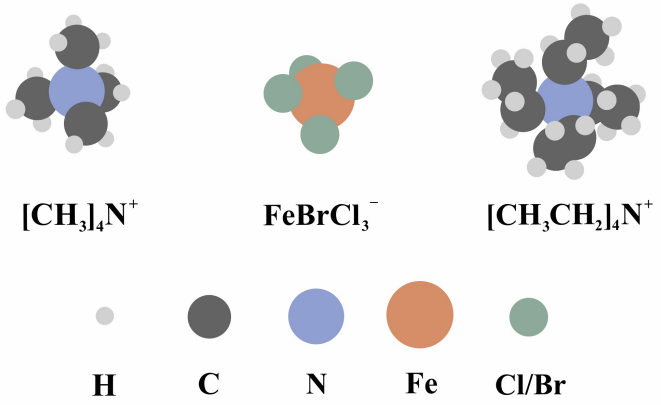

Figure 2.7: Schematic of the TMA^+, $FeBrCl_3^-$ and TEA^+ ions, the constituents of $TMAFeBrCl_3$ and $TEAFeBrCl_3$. The cations differ only in the length of the alkyl chains. Different atoms are illustrated with different colours, relative sizes are not to scale. Retrieved from [1].

2.4.1 TMA bromotrichloroferrate(III)

$TMAFeBrCl_3$ is a supramolecular organic-inorganic plastic crystal currently garnering interest for use in ferroelectric applications.[12,13,49,50] The ionic crystal lattice is made up of the organic cation TMA^+ and the inorganic anion $FeBrCl_3^-$. The crystal structure is temperature-dependent, with five possible polymorphs between -20 and 130 °C,[12] presented in Figure 2.8. Of these five crystal structures, two are centrosymmetric, paraelectric structures (II: Cmcm and V: Pbcm) and another two are non-centrosymmetric ferroelectrics (III: Amm2 and IV: Pma2). The last is the mesophase $Pm\bar{3}m$, which is conventionally called phase number I as it is the highest temperature structure. All the structures below the mesophase are orthorhombic, while the mesophase itself is cubic. The phase transitions between the polymorphs happen at characteristic temperatures, which can be seen in Figure 2.9. The lowest-temperature phase, Pbcm (V), is only stable up to ca. -10 °C, and the following Pma2 (IV) up to just above 20 °C. At room temperature, Amm2 (III) is the stable structure, until a transition into Cmcm (II) below 80 °C. The transition into the mesophase ($Pm\bar{3}m$) takes place at around 111 °C.

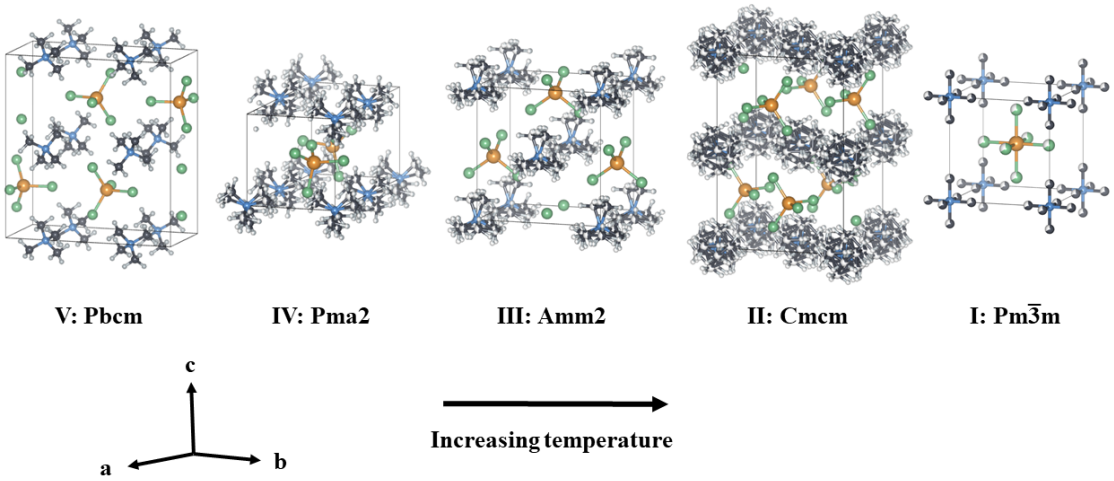

Figure 2.8: Unit cells of the crystal polymorphs of $TMAFeBrCl_3$. With increasing temperature, the material can experience four phase transitions. The structures were made using data files from Harada et al.[12] with VESTA software.[51] The structures take into account the several possible orientations of the molecules.

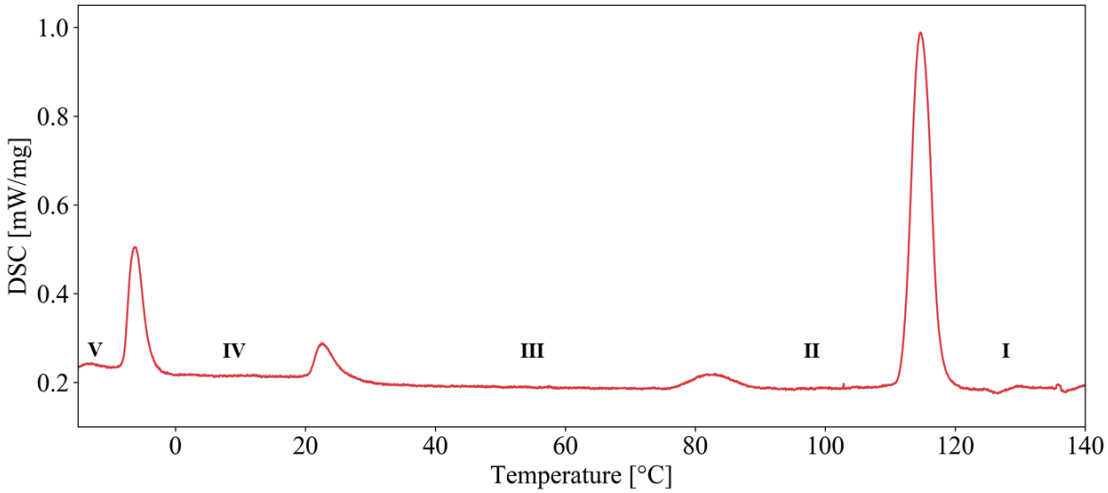

Figure 2.9: Differential scanning calorimetry (DSC) curve of $TMAFeBrCl_3$. Through measuring the heat required to raise the temperature of the material, phase transitions are found (indicated by peaks). The curve is annotated with the structures of the material (presented in Figure 2.8). Based on experimental data.[52]

Harada et al.[12] have reported on the ferroelectric properties of the Amm2 phase of $TMAFeBrCl_3$. They detected multiaxial polarisation, meaning that the material has several possible polarisation axes. This would significantly ease processing requirements as the material can be made polycrystalline, needing only a quick poling process to align domains and gain macroscopic polarisation values on par with those of monodomain single crystals. $TMAFeBrCl_3$ in the Amm2 phase furthermore has high piezoelectric coefficients (~110 pC/N) as well as low coercive fields (67 kV/cm).[12] The low coercive field is explained by the rotation of the globular molecules, as this mitigates the field needed to re-orient them. The Amm2 structure reportedly favours dendritic crystal growth.[13]

2.4.2 TEA bromotrichloroferrate(III)

$TEAFeBrCl_3$ is also an organic-inorganic plastic crystal, but unlike $TMAFeBrCl_3$, it is only polar and has not exhibited ferroelectric behaviour. The compound is not as thoroughly studied as its TMA^+ counterpart, but information on the isostructural $TEAFeBrCl_4$[53–55] can be used to gain insight since all tetraethylammonium tetrahaloferrates ($FeCl_{4-n}Br_n^-$, n = 0-4) can be considered isomorphous.[56] $TEAFeBrCl_4$ crystallises in the hexagonal wurtzite $P6_3mc$ structure at room temperature,[53] but at lower temperatures the material will transition first to hexagonal $P6_3$ followed by orthorhombic $Pca2_1$.[54] In addition to this, thermal analysis has determined approximate positions for phase transitions, but these values are more prone to influence from replacement of Cl^- with Br^-. However, unpublished results from J.Walker (NTNU)[52] indicate a transition into the mesophase at approximately 157 °C, as seen in Figure 2.10. $TEAFeBrCl_3$ does not possess multiaxial polarisation and has a lower piezoelectric coefficient of ~6 pC/N. Though the $P6_3mc$ structure is thought to be a piezoelectric structure only, recent studies suggest uniaxial polarisation is possible based on theoretical calculations.[57] This has however not been experienced in $TEAFeBrCl_3$.

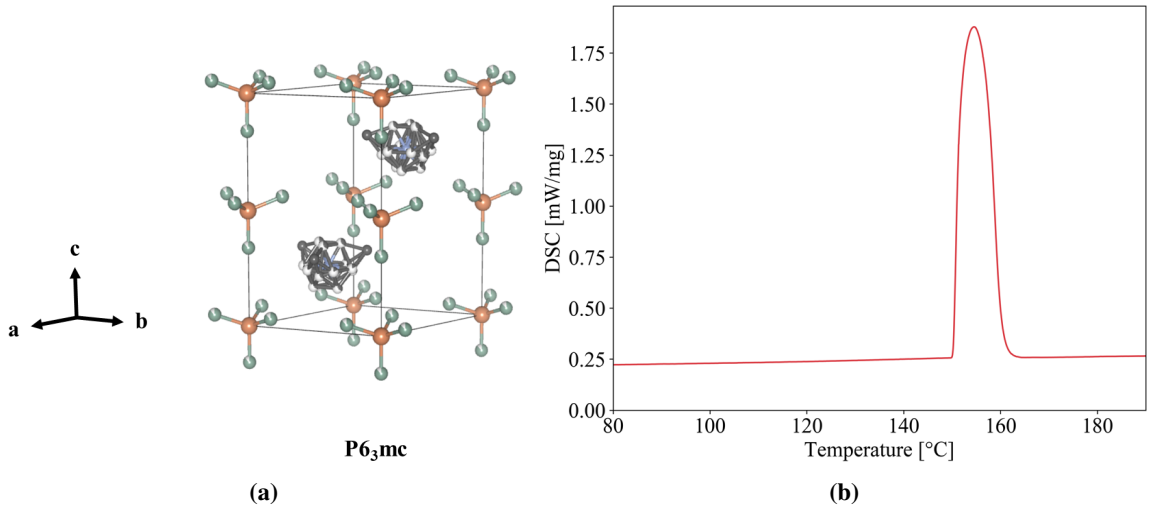

Figure 2.10: (a) The $P6_3mc$ crystal structure, generated with data files from Evans et al.[14] and VESTA software.[51] The structure take into account the several possible orientations of the cations. (b) DSC heating curve of $TEAFeBrCl_3$ from unpublished results from J. Walker (NTNU).[52] A peak at ca. 157 °C can be seen, indicating a phase transition at this temperature.

2.4.3 The solid solution system $TMA_xTEA_{1-x}FeBrCl_3$

$TMAFeBrCl_3$ and $TEAFeBrCl_3$ consist of only the same types of atoms but different numbers of them, yet they nevertheless possess very different properties. By combining the two in a solid solution system, these differences could be used to produce a new compound with the optimum of both end members' features. TMA^+ and TEA^+ have the same valency, but the deviation in the size of the cations complicates the formation a solid solution. TMA^+ and TEA^+ have ionic radii of 3.22 Å and 3.85 Å respectively,[58] thus the formation of substitutional solid solution will require either that TMA^+ fills a lattice position meant for larger molecules or TEA^+ compresses into a lattice site meant for smaller. Consequently, solid solutions are less likely to form when deviating too far from

smaller percentages of cation substitutions and a solid solution system of $TMA_xTEA_{1-x}FeBrCl_3$ is most probably not continuous.

From preliminary work by J. Walker at NTNU,[52] a tentative phase diagram can be drawn for the $TMA_xTEA_{1-x}FeBrCl_3$ solid solution system, as seen in Figure 2.11. This phase diagram indicates that the hexagonal $P6_3mc$ structure of $TEAFeBrCl_3$ will dominate over the majority of the compositional range, with Cmcm appearing as the first of the orthorhombic $TMAFeBrCl_3$ structures in the material simultaneously with $P6_3mc$, i.e. phase separation. Solid substitution of the TEA^+ cation into the $TMAFeBrCl_3$ crystal structures does not occur extensively, but appears to happen only for small amounts of TEA^+. The phase diagram is however not yet completed, and to further elucidate the intricate interplay between phases.

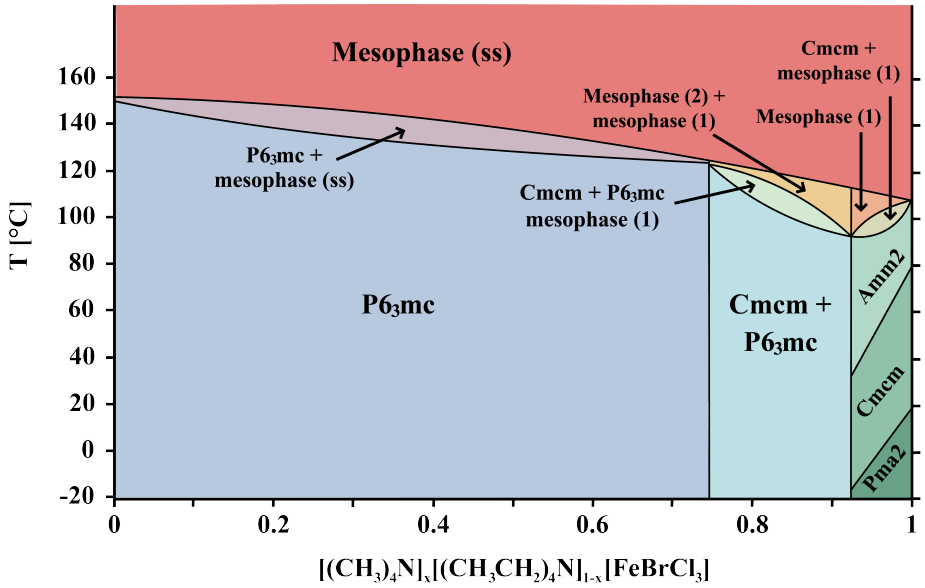

Figure 2.11: Tentative phase diagram of the $TMA_xTEA_{1-x}FeBrCl_3$ system, adapted from an original by J. Walker (NTNU).[52]

Chapter 3

Experimental

3.1 Synthesis of crystalline powders

$TMAFeBrCl_3$ and $TEAFeBrCl_3$ crystals were prepared separately before mixing to produce the array of compositions. Two approaches were used for the synthesis of the $TMAFeBrCl_3$. A schematic of the synthesis is illustrated in Figure 3.1. $TMAFeBrCl_3$ crystals were synthesised by first dissolving TMABr (9.94 g, 98 %, Sigma Aldrich) and $FeCl_3{\cdot}6H_2O$ (17.27 g, 99 %, Sigma Aldrich) in separate beakers of distilled water before combining the two solutions in a round-bottom flask. Water (80 mol%) was evaporated at 70 °C using a water bath (BUCHI Rotavapor R-210) while the sample was under constant agitation. The crystals were then redissolved in approximately 100 mL of ethanol (96 %, VWR International). Crystals recrystallised overnight and were extracted by vacuum filtration. These crystals were named C-TMA1. The leftover ethanol solution from the filtration was evaporated (water bath at 70 °C, constant agitation) to produce another set of crystals named C-TMA2. Both C-TMA1 and C-TMA2 crystals were dried in a vacuum furnace at 70 °C for 8 h and subsequently kept in a desiccator.

$TEAFeBrCl_3$ crystals were made from TEABr (11.52 g, 98 %, Sigma Aldrich) and $FeCl_3{\cdot}6H_2O$ (14.67 g, 99 %, Sigma Aldrich) separately dissolved in distilled water. The two solutions were mixed together in a crystallisation dish and the water was evaporated slowly by covering the dish with aluminium foil with holes and leaving for fourteen days. Resulting crystals, named C-TEA, were crushed with mortar and pestle and kept in a desiccator.

To yield crystals with varying amounts of TMA and TEA cations, the produced $TMAFeBrCl_3$ and $TEAFeBrCl_3$ crystals were first dried for 2 h at 60 °C before they were weighed out and mixed together. Six compositions were made of $TMA_xTEA_{1-x}FeBrCl_3$, with x = 0.7 to 1. Both C-TMA1 and C-TMA2 were used as $TMAFeBrCl_3$ sources for all samples. The mixed powders were then annealed in a high-temperature furnace (Nabertherm P330) at 240 °C for 2 h. The heating rate was approximately 3.55 °C/min and after the finished program, cooling happened slowly and was not controlled. Crystal powder samples were kept in a desiccator. Samples were named C-y where y is the mol% TMA^+: C-100, C-97.5, C-95, C-90, C-80 and C-70. They are listed in Table 3.1 with details about characterisation.

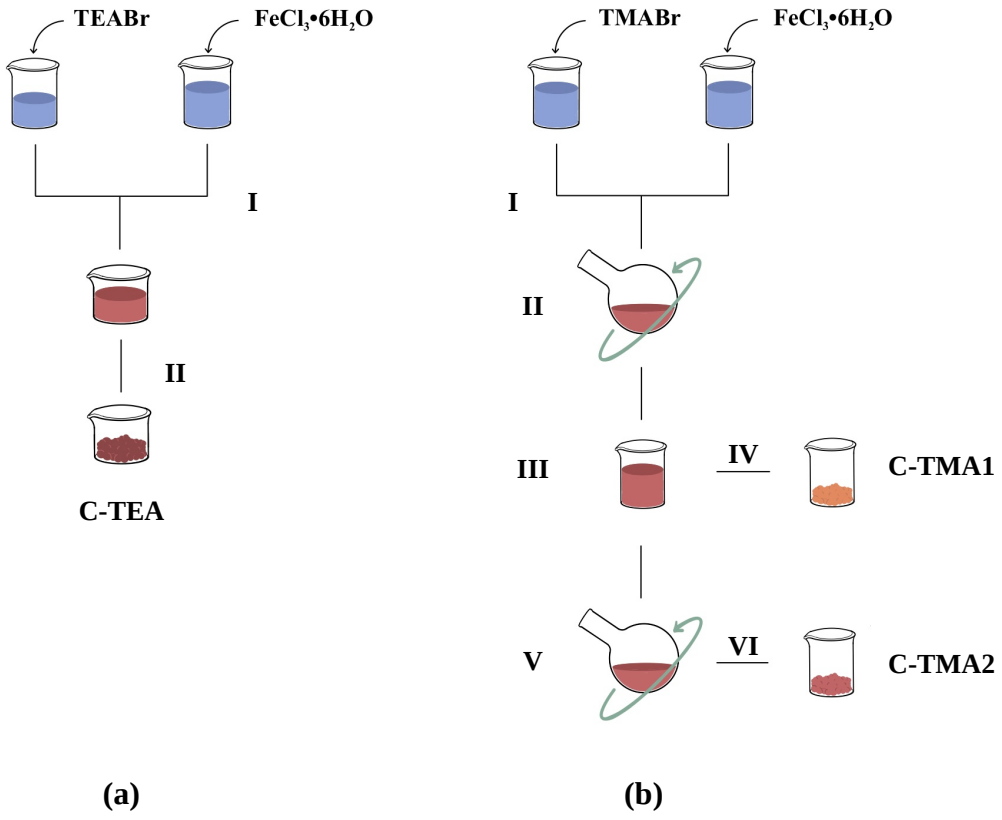

Figure 3.1: Flow chart showing the crystallisation from solution of C-TEA, C-TMA1 and C-TMA2. (a) The process for C-TEA started with dissolution of precursors in water, before mixing the solutions together (**I**). In step **II**, water is slowly evaporated before the product is obtained.
(b) For the C-TMA1 and C-TMA2 synthesis, dissolution of precursors followed by mixing is also the first step (**I**), followed by assisted evaporation of the water (**II**). In step **III**, crystals are dissolved in ethanol. Step **IV** represents recrystallisation from ethanol to give C-TMA1, whereas steps **V** and **VI** show evaporation of remaining ethanol solution, yielding C-TMA2.

3.2 Hot pressing

A pressed pellet sample was prepared from all annealed crystal samples. The pressing process is illustrated with a schematic in Figure 3.2. The crystals were first dried at 60 °C for 2 hours, before 0.2-0.3 g of crystal powder were weighed out and placed on a steel plate (5x5 cm^2) covered by aluminium foil. Another set of steel plate and aluminium foil was then placed on top of the powder, before the entire arrangement was transferred to a hot press (Carver 4122CE) preheated to 140 °C. A pressure of approximately 3.9 MPa was applied for 15 minutes. Due to the lack of horisontal (lateral) confinement, edges of the pressed pellets did not densify and were removed with tweezers before further processing and characterisation. Pressed samples were named P-y (y corresponding to the powder sample they were pressed from): P-100, P-97.5, P-95, P-90, P-80 and P-70. They are also listed in Table 3.1.

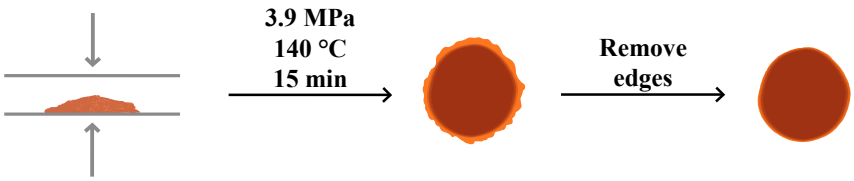

Figure 3.2: Schematic showing the pressing of the crystal powder samples. Powder was weighed out and pressed at 140 °C and 3.9 MPa for 15 minutes. Edges that did not densify were broken off using tweezers.

3.3 Characterisation

3.3.1 Crystal structures

X-ray diffraction (XRD) measurements were performed on all samples (C-90 was measured both before and after annealing) to learn about their crystal structures. The crystal powder samples were first crushed to reduce particle size before transfer to a sample holder. Crystal pellet samples were prepared for measurements using deep sample holders and putty for fixing the pellet in place. A Bruker A25 DaVinci X-Ray Diffractometer was used for the measurements, and diffractograms were recorded in the 5-75° 2θ range for 30 min, using CuK_α radiation and a 0.1° slit opening for C-100 and C-97.5 as well as all pressed samples. C-90, C-80 and C-70 were measured using 5-75° 2θ for 120 min, also with CuK_α radiation and a 0.1° slit opening. The diffractograms of C-90, C-80 and C-70 were normalised by dividing intensities by four. Data for C-95 was taken from [1], where it was measured with the same parameters as C-100 and C-97.5..

Rietveld refinement was done using the DIFFRAC.SUITE TOPAS software. Crystal information files (.cif) from Harada *et al.* [12] and Evans *et al.* [14] were used. The files from Harada *et al.* described a $TMAFeCl_4$ compound and were therefore modified to accommodate the replacement of one of the Cl^- ions with Br^-. Br^- was added to the structure by using the same x, y and z coordinates as the corresponding Cl^-, but with altered occupancy (0.125 and 0.875 for respectively Br^- and Cl^-).

Initial analysis was performed using *hkl* phases to determine approximate crystal lattice parameters, before Rietveld refinement was done to determine phase percentages present. Lattice parameters, microstructure crystal size L and sample displacement were refined first, before increasing the background polynomial order. Finally, preferred orientation was partially accounted for through the spherical harmonics and March Dollase functions.

3.3.2 Crystal morphology

Two samples were imaged in a Hitachi S3400N SEM to investigate the effect of annealing on morphology: C-100 and C-90, both investigated before and after annealing. A sample stub was covered with copper tape before dipping into the crystal powders. A 5 kV electron beam was used for the imaging due to the low conductivities of the crystals.

Table 3.1: List of synthesised and pressed samples, along with descriptions and details about characterisation techniques. C-TMA1, C-TMA2 and C-TEA have SEM marked with * as they were imaged together in a mixture and not separately. C-95 was not prepared during this project, but was taken from [1], and XRD data for this sample was also taken from [1].

Sample	Description	Characterisation
C-TMA1	From recrystallisation in ethanol	XRD, SEM*
C-TMA2	From evaporation of remaining ethanol solution	XRD, SEM*
C-TEA	From slow evaporation	XRD, SEM*
C-100	$TMAFeBrCl_3$	XRD, DSC, SEM
C-97.5	$TMA_{0.975}TEA_{0.025}FeBrCl_3$	XRD, DSC
C-95	$TMA_{0.95}TEA_{0.05}FeBrCl_3$ from [1]	XRD, DSC
C-90	$TMA_{0.9}TEA_{0.1}FeBrCl_3$	XRD, DSC, SEM
C-80	$TMA_{0.8}TEA_{0.2}FeBrCl_3$	XRD, DSC
C-70	$TMA_{0.7}TEA_{0.3}FeBrCl_3$	XRD, DSC
P-100	Pressed C-100	XRD, dielectric and ferroelectric measurements
P-97.5	Pressed C-97.5	XRD, dielectric and ferroelectric measurements
P-95	Pressed C-95	XRD, dielectric and ferroelectric measurements
P-90	Pressed C-90	XRD, dielectric and ferroelectric measurements
P-80	Pressed C-80	XRD, dielectric and ferroelectric measurements
P-70	Pressed C-70	XRD, dielectric and ferroelectric measurements

3.3.3 Phase transitions

Differential scanning calorimetry (DSC) was used to gain information about the phase transitions of the crystal structures. All crystal samples C-100 to C-70 were investigated. Crystal powder (5-10 mg) was added to a pre-weighed aluminium crucible and lid, which were then sealed using a pressing tool. The crucible was placed into the instrument (Netzsch DSC 214 Polyma) along with an empty aluminium crucible reference.

Two heating/cooling cycles were used for all samples. C-100 and C-97.5 were measured using a program cycling between -25 °C and 200 °C with a 10 K heating/cooling rate and a 15 min hold at maximum and minimum temperatures. The program is shown in Figure 3.3. Due to instrument malfunctions during cooling, a modified program was used for the remaining samples. C-95. C-90, C-80 and C-70 were measured with a program heating from room temperature to 200 °C, holding for 15 min before cooling to 35 °C, holding for 15 min and then repeating. 10 K/min was used as the heating rate, but the cooling rate was reduced to 5 K/min. A synthetic air mix was used for the gas flow and N_2 was used as the protective gas. Flow rates were 50 mL/min for both gases.

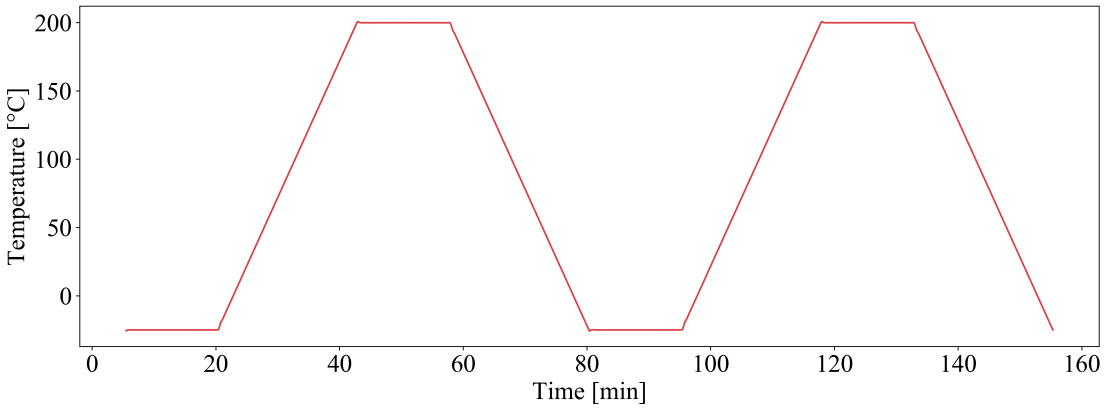

Figure 3.3: DSC temperature program. The program goes between -25 and 200 °C, with heating/-cooling rates of 10 K/min and 15 min holds at maximum and minimum temperatures.

3.3.4 Electrical properties

Before electrical measurements, pressed pellets were cut into pieces of approximately 5 x 5 mm^2 and circular gold electrodes of 10 mm^2 were deposited using a shadow mask and sputter coating (Edwards Sputter Coater S150B). Electrodes were deposited on both sides of the pellet in an Ar atmosphere.

Dielectric properties of all pressed samples were investigated as a function of varying frequency in the 10^{-2} - 10^{7} Hz range. Measurements were performed with a set-up composed of a Novocontrol Alpha-A analyser, Novocontrol BDS 1200 sample cell, Novocontrol ZG4 test interface and Novocontrol WinDETA software. An AC voltage signal V_{rms} = 1 V was used for all measurements.

Ferroelectric testing of all pressed pellets was done using an Aixacct ferroelectric tester and a Trek 10 kV amplifier in combination with a laser interferometer. The electric field was applied using a triangular waveform and the sample was submerged in silicone oil to prevent arcing. Starting at 1 kV/cm and 10 Hz, the field was increased to 10 and then 20 kV/cm, where a frequency sweep from 100 to 1 Hz was performed. After returning to 10 Hz, the field was increased in increments of 10 kV/cm up to 200 kV/cm (only 180 kV/cm for C-100). Below 180 kV/cm, only a single cycle was performed at each field amplitude, however after reaching 180 kV/cm, several cycles were measured at each field amplitude before continued incremental increase. After cycling at 200 kV/cm, another frequency sweep from 100 to 1 Hz was performed at 200 kV/cm. Upon lack of ferroelectric behaviour at 200 kV/cm, higher fields, lower frequencies or a combination of both were attempted for several samples. For P-100, 100 Hz was used while increasing the field amplitude, but cycling at 180 kV/cm was performed at 10 Hz as for the other samples.

Chapter 4

Results

4.1 Synthesis observations

As detailed in Section 3.1, crystals of the end member compositions $TMAFeBrCl_3$ and $TEAFeBrCl_3$ were first synthesised independently before combining to produce more compositions. Two batches of $TMAFeBrCl_3$ crystals (C-TMA1 and C-TMA2) were obtained, as the yield of the first was lower than desired. The yields of the C-TMA1 and C-TMA2 crystals were respectively 1.81 g (9.1 %) and 3.09 g (15.5 %) for a total of 4.90 g (24.6 %). C-TMA1, the batch from recrystallisation in ethanol, consisted of a light orange, flocculated powder of long and thin crystals stuck together in bigger agglomerates. The C-TMA2 crystals, on the other hand, precipitated in a finer, red, agglomerated powder. The C-TEA crystals were produced with a yield of 18.9 g (94.5 %) and had a dark brown, nearly black colour. The crystals formed larger particles than the C-TMA ones, which were powders, and the particles had to be broken up and crushed before using in subsequent processing and characterisation. Pictures of the C-TMA1, C-TMA2 and C-TEA samples are presented in Figure 4.1.

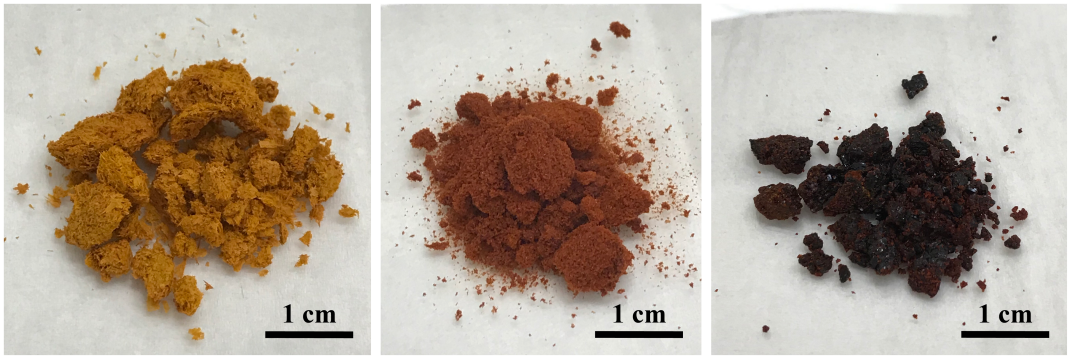

Figure 4.1: Pictures of (a) C-TMA1, (b) C-TMA2 and (c) C-TEA. Scale bars are only approximate.

After annealing, samples developed a darker, more red colour. The exact colour of the samples before annealing would vary depending on the ratios of C-TMA1, C-TMA2 and C-TEA powders used. Figure 4.2 shows the difference in colour for sample C-80 before and after annealing. It should be noted that there is also a difference in the background colour in images (a) and (b), meaning lighting might have contributed to a contrast difference.

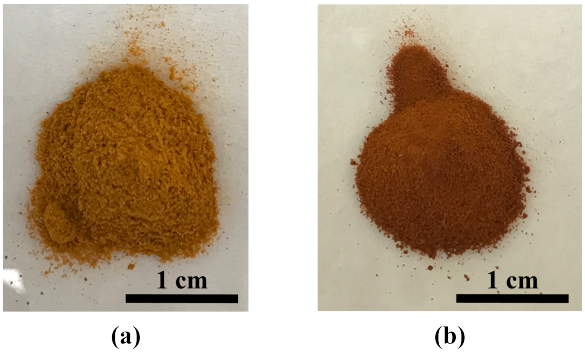

Figure 4.2: Comparison of C-80 before (a) and after (b) annealing. The lighting in the pictures is slightly different, as evident from the background. The scale bars are only approximate.

Pressing the crystal powders gave dark brownish red pellets with orange edges where powder did not densify. Images of all the pressed samples can be seen in Figure 4.3. P-100, P-97.5, P-90, P-80 and P-70 were all opaque samples. Of these, P-97.5 differentiates itself somewhat in that bigger grains are visible due to their lighter colour. Grains are also visible in the other samples, and in these cases they contribute to surface roughness. P-95 was the only sample not completely opaque, but rather faintly transparent. It was also the thinnest sample. The thickness of the samples are displayed in Table 4.1.

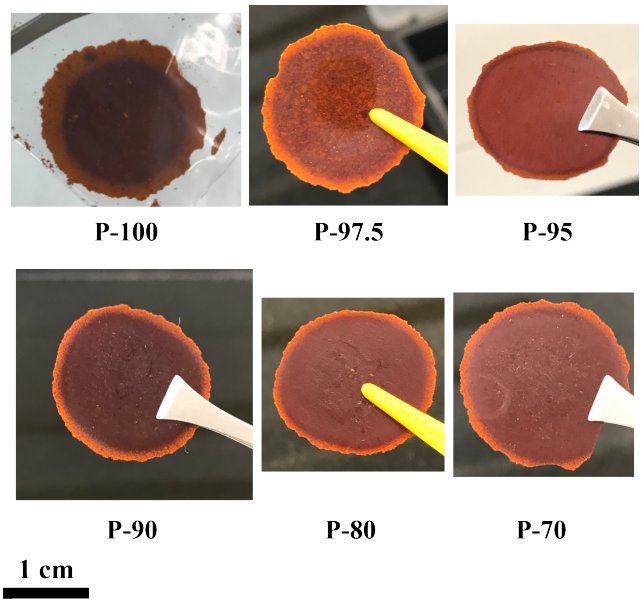

Figure 4.3: Pictures of all pressed pellets P-100, P-97.5, P-95, P-90, P-80 and P-70. The scale bar is only approximate and applies for all.

Table 4.1: Thickness of pressed samples P-100, P-97.5, P-95, P-90, P-80 and P-70 in µm.

Sample	P-100	P-97.5	P-95	P-90	P-80	P-70
Thickness [µm]	450	440	335	480	395	423

4.2 The effect of annealing on surface morphology and phase composition

A change in the colour of the powder samples was observed during the synthesis, from orange (the shade depending on exact composition) to red after annealing. The effect of annealing was also investigated through SEM imaging and XRD. In Figure 4.4, particles from sample C-100 can be seen before ((a), (b)) and after ((c), (d)) annealing. Before annealing, particles have irregular shapes with sharp edges on the surfaces. However, after annealing, the particles have coarsened and there is evidence of necking. On the particle imaged in Figure 4.4 (c), large regions of the surface have smoothened and become flat.

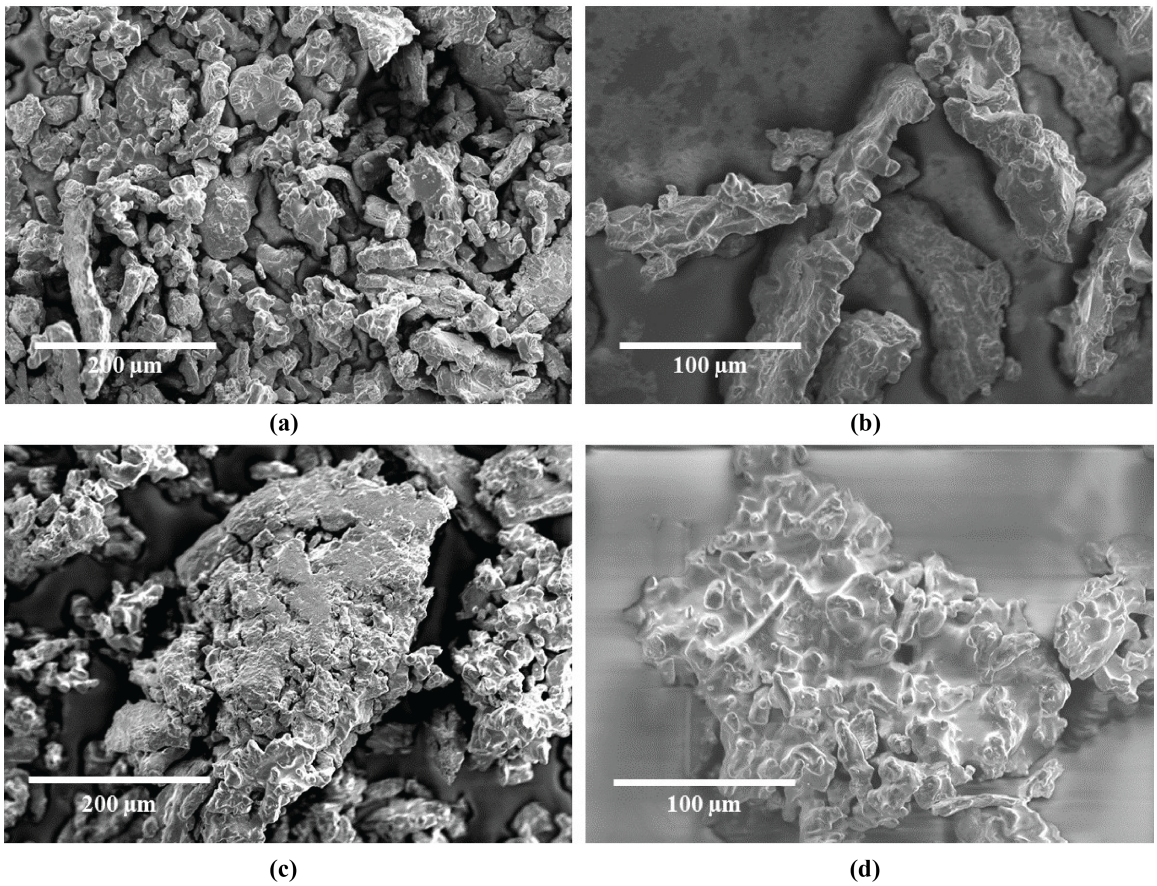

Figure 4.4: SEM micrographs of C-100 before ((a), (b)) and after ((c), (d)) annealing.

Figure 4.5 shows the effects of annealing on the C-90 crystals. In Figure 4.5 (a) a dendritic structure can be seen, which is typical for the Amm2 phase. In (b) a particle consisting of fairly large facets, but also small, sharp and irregular features are seen. These could be smaller particles lying on the surface of a bigger one. There is little evidence of hexagonal crystals, as would be expected from the C-TEA particles since $TEAFeBrCl_3$ reportedly favours the hexagonal $P6_3mc$ structure. After annealing, coarsening and necking is visible. There are fewer sharp edges, and no evidence of smaller particles sitting on top of bigger ones, as is potentially the case in (b). Rather, there are minor protrusions and bumps on the particles, that could be the result of fusion between small and large particles (as in (b)) during annealing. Dendritic structures such as in (a) are also absent after annealing.

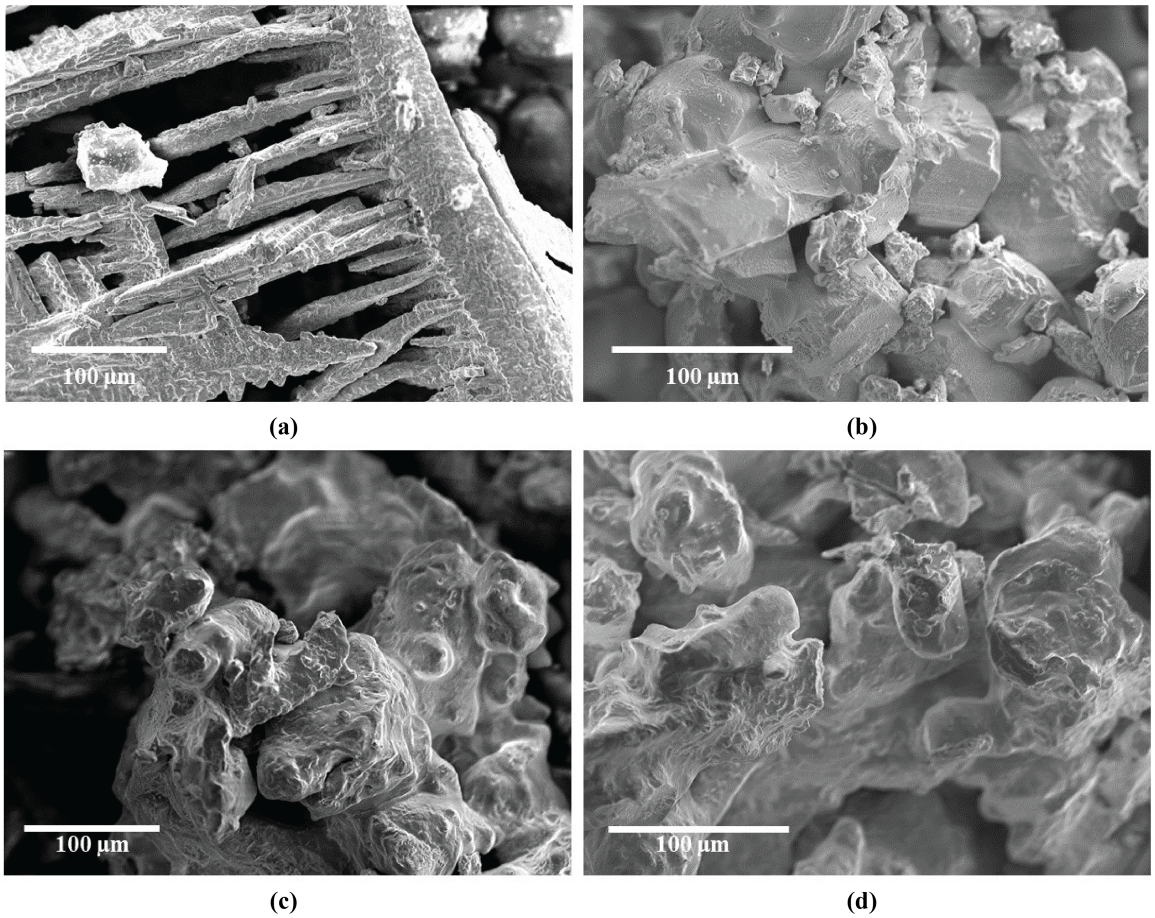

Figure 4.5: SEM micrographs of C-90 before ((a), (b)) and after ((c), (d)) annealing.

The effect of annealing on the phase composition of the C-90 sample is seen through the diffractograms in Figure 4.6. Before annealing, Rietveld refinement indicated that the sample consisted of 94 % Amm2 and 6 % $P6_3mc$, with a *goodness of fit* (GOF) of 1.35. The ratio of phases appears different from what would be expected from the composition, 90 % $TMAFeBrCl_3$ and 10 % $TEAFeBrCl_3$, however, a 10 % uncertainty associated with laboratory XRD must be kept in mind. After annealing, the suggested composition was 100 % Cmcm, from a fit with GOF 1.45.

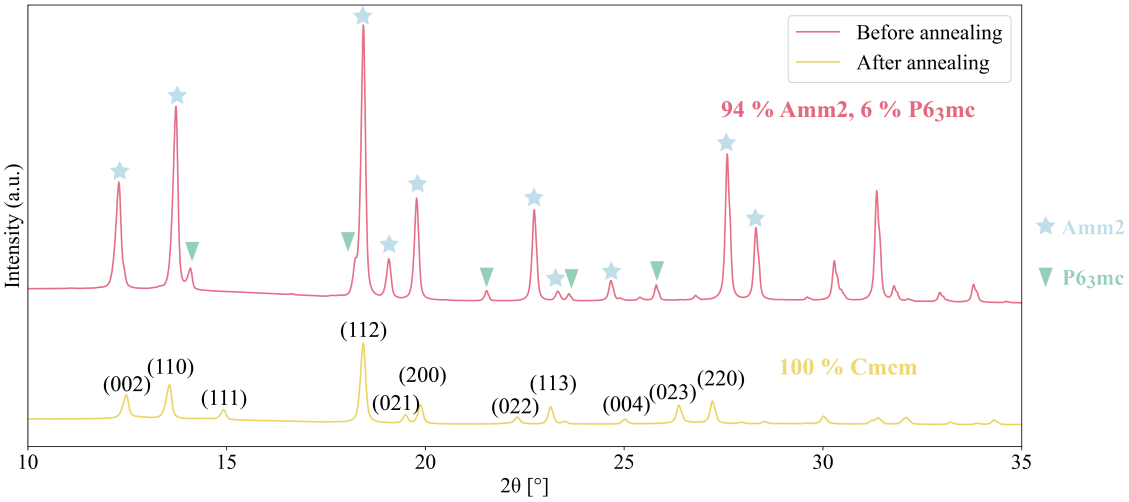

Figure 4.6: X-ray diffractograms of C-90 before and after annealing. The GOF for the two fits was respectively 1.35 and 1.45. Peaks associated with Amm2 and P6$_3$mc are labeled with symbols, while the Cmcm peaks of the annealed sample are labeled with Miller indices.

4.3 Crystal structures and phase compositions

The crystal structures of all samples, powders and pressed, were investigated using XRD. The C-TMA1, C-TMA2 and C-TEA samples were also studied, and the diffractograms are presented in Figure 4.7, where Miller indices are also noted. The samples were found to be 100 % Amm2, Amm2 and P6$_3$mc, respectively. The lattice parameters were a = 7.212(5) Å, b = 8.980(6) Å and c = 9.297(7)Å for C-TMA1, while for C-TMA2, a = 7.232(9) Å, b = 8.998(6) Å and c = 9.317(2) Å. The P6$_3$mc lattice parameters of C-TEA were found to be a = 8.263(5) Å and c = 13.316(7) Å. The first uncertain digit is given in parenthesis, based on the error estimation in TOPAS.

4.3.1 Crystal structure as a function of composition

Figure 4.8 shows the X-ray diffractograms of all the crystal powders of chemical compositions between 100 % and 70 % TMA^+. Also included are the phase percentages from Rietveld refinement, written over each diffractogram in matching colour. The analysis revealed that Cmcm was the majority phase for all compositions, but the presence of a minority phase varied with composition. For C-100, refinement determined that a Cmcm was the majority phase at 88 % with a minority Amm2 phase (12 %). For C-97.5, C-95 and C-90, Cmcm was suggested to be the only phase present. At 80 and 70 % TMA^+, a minority P6$_3$mc phase appears. The amount of this phase increases (at the expense of the Cmcm phase) with increased addition of TEA^+. An overview of majority and minority phases as well as GOF and majority phase lattice parameters for each powder sample is summarised in Table 4.2. Individual diffractograms for all crystal samples C-100 to C-70, containing observed data, calculated refinement fits and the difference between them can be found in Appendix A.

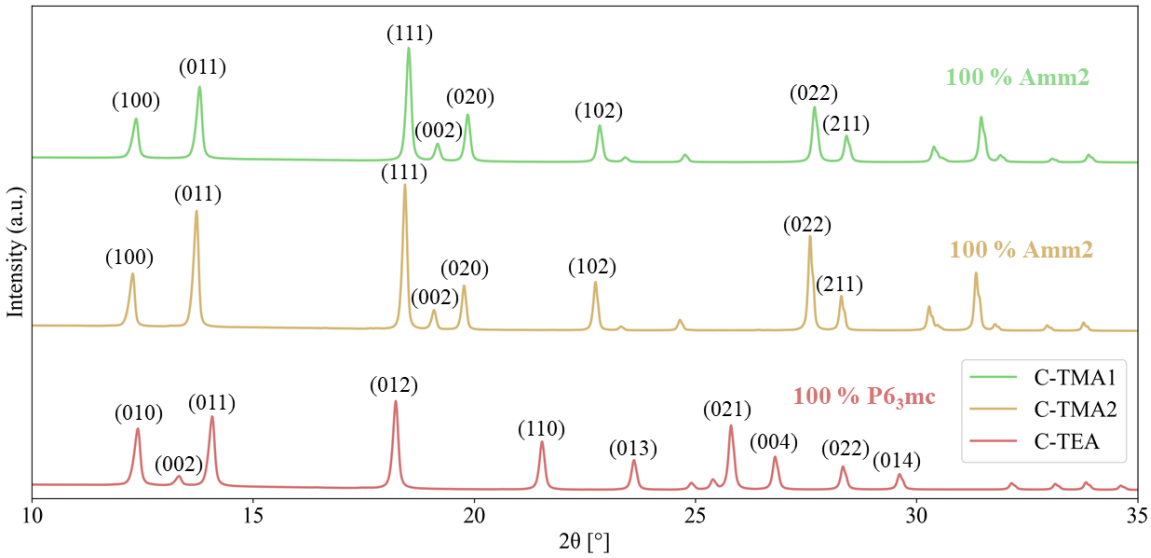

Figure 4.7: X-ray diffractograms of C-TMA1, C-TMA2 and C-TEA. C-TMA1 and C-TMA2 were both found to be 100 % Amm2, while C-TEA was 100 % P6$_3$mc. The GOF were respectively 1.25, 1.47 and 2.38 for the three samples.

Table 4.2: XRD Rietveld refinement results summarised for powder samples C-100 to C-70. The lattice parameters are those of the majority Cmcm phase. The first uncertain digit of the lattice parameters is given in parenthesis.

Sample	Majority phase	*a* [Å]	*b* [Å]	*c* [Å]	Minority phase	GOF
C-100	Cmcm (88 %)	8.927(8)	9.614(6)	14.250(9)	Amm2 (12 %)	1.32
C-97.5	Cmcm (100 %)	8.930(8)	9.617(2)	14.250(6)	-	1.38
C-95	Cmcm (100 %)	9.118(6)	9.76(9)	14.39(9)	-	1.26
C-90	Cmcm (100 %)	8.971(0)	9.653(0)	14.283(3)	-	1.45
C-80	Cmcm (87 %)	8.962(1)	9.643(9)	14.25(3)	P6$_3$mc (13 %)	1.49
C-70	Cmcm (75 %)	8.97(0)	9.65(0)	14.24(4)	P6$_3$mc (25 %)	1.58

Comparing the peak intensities of the different diffractograms also gives information about changes in the phases present at different compositions. When going from C-90 to C-70, there is a decrease in the intensity of the peaks associated with Cmcm occurring simultaneously with emerging peaks for P6$_3$mc. This, together with refinement, suggests that there is a P6$_3$mc phase increasing in amount at the expense of the Cmcm phase. However, peak intensities are also readily affected by preferential orientation, and should not be used as the only basis for an argument concerning phase content. Since the C-90, C-80 and C-70 samples were measured with longer measurement times to help with peak deconvolution and diffractograms had to be normalised, care must be taken when comparing the intensities between these three normalised and other non-normalised diffractograms.

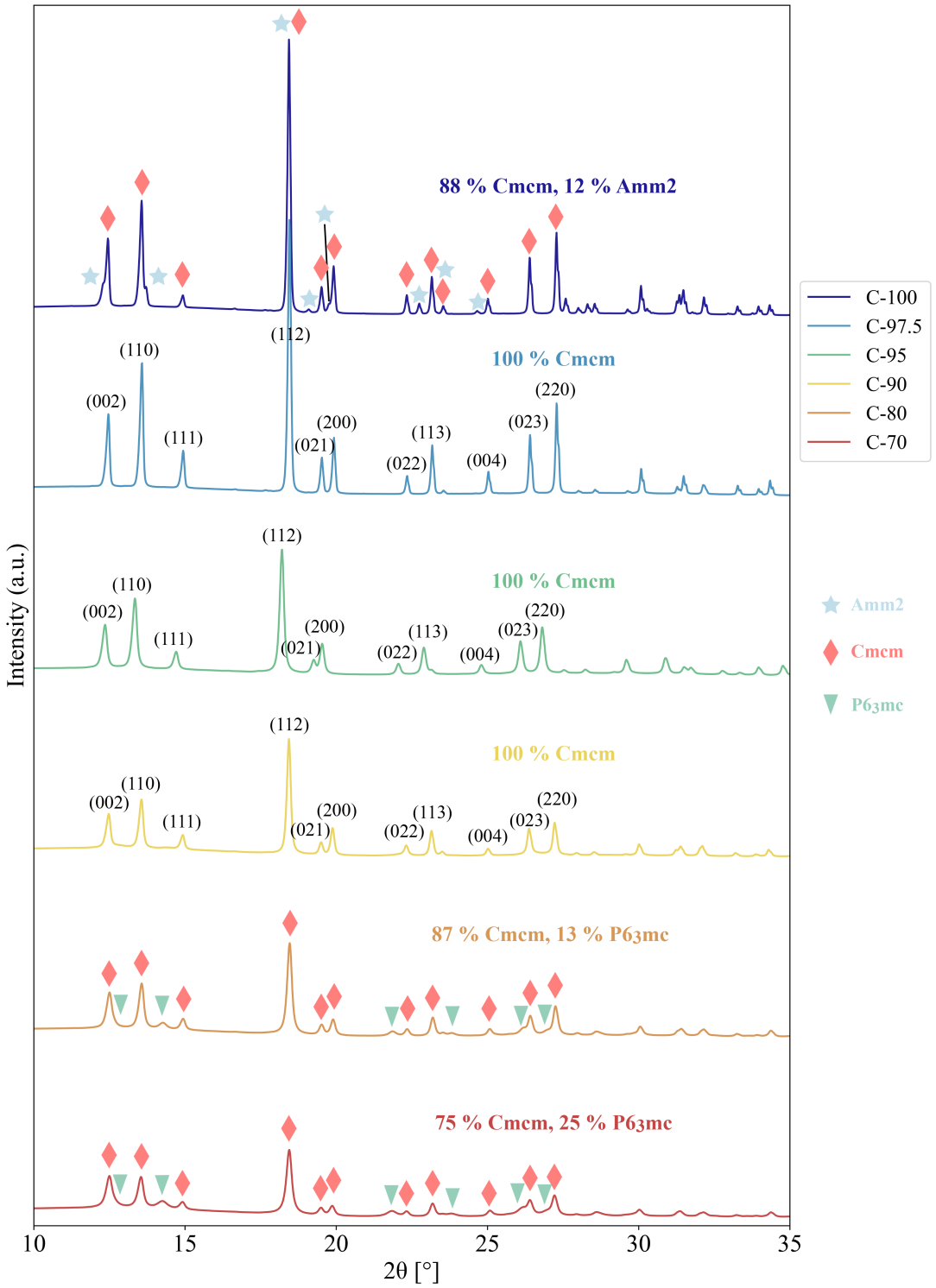

Figure 4.8: X-ray diffractograms of all crystal powder samples C-100, C-97.5 C-95, C-90, C-80 and C-70. Peaks are labeled with Miller indices (C-97.5, C-95 and C-90) or symbols (C-100, C-80 and C-70). Estimated phase percentages are indicated over each diffractogram.

4.3.2 Crystal structure of pressed samples

In order to ensure the crystal structures were not affected by the hot pressing progress, the structures of the pressed samples were analysed with XRD. In Figure 4.9, the diffractograms of all the pressed samples P-100 to P-70 are plotted along with suggested phase percentages from Rietveld refinement. Individual diffractograms for all pressed samples can also be found in Appendix A, along with those of the powder samples. The results are overall similar to those from the powder samples. For C-97.5, C-95 and C-90, Cmcm was found to be the only phase present. As presented in Table 4.3, the Cmcm lattice parameters were suggested to be largest for C-95, despite single phase Cmcm in C-90 demanding more substitution of TEA^+ into positions of TMA^+ than required for C-95. Both C-80 and C-70 were found to have a combination of Cmcm and $P6_3mc$ phases. Rietveld refinement indicated 92 % Cmcm and 8 % Amm2 for C-80, while for C-70 the numbers were 79 % and 21 %.

The refinement of the P-100 diffractogram was inconclusive. Cmcm was determined to be the majority phase, but both refinements with and without an Amm2 minority phase produced reasonable results, with GOF of respectively 1.32 and 1.34. Due to extensive overlap between the peaks of the Cmcm and Amm2 phases, determining exact phase percentages is especially challenging for the combination of these crystal structures. Nevertheless, the refinement indicates that the amount of Cmcm might lie between 66 and 100 %, and the Amm2 content between 0 and 34 %.

Table 4.3: XRD Rietveld refinement results summarised for powder samples P-100 to P-70. The lattice parameters are those of the majority Cmcm phase. The first uncertain digit of the lattice parameter estimates is given in parenthesis. For P-100, lattice parameters and GOF are taken from the refinement using both Cmcm and Amm2.

Sample	Majority phase	*a* [Å]	*b* [Å]	*c* [Å]	Minority phase	GOF
P-100	Cmcm (100-66 %)	8.924(8)	9.61(7)	14.24(9)	Amm2 (0-34 %)	1.32
P-97.5	Cmcm (100 %)	8.930(0)	9.61(5)	14.24(7)	-	1.28
P-95	Cmcm (100 %)	9.106(6)	9.76(8)	14.37(5)	-	1.28
P-90	Cmcm (100 %)	8.99(1)	9.67(9)	14.28(3)	-	1.46
P-80	Cmcm (92 %)	9.06(0)	9.71(8)	14.29(6)	$P6_3mc$ (8 %)	1.44
P-70	Cmcm (79 %)	9.01(1)	9.68(2)	14.23(4)	$P6_3mc$ (21 %)	1.41

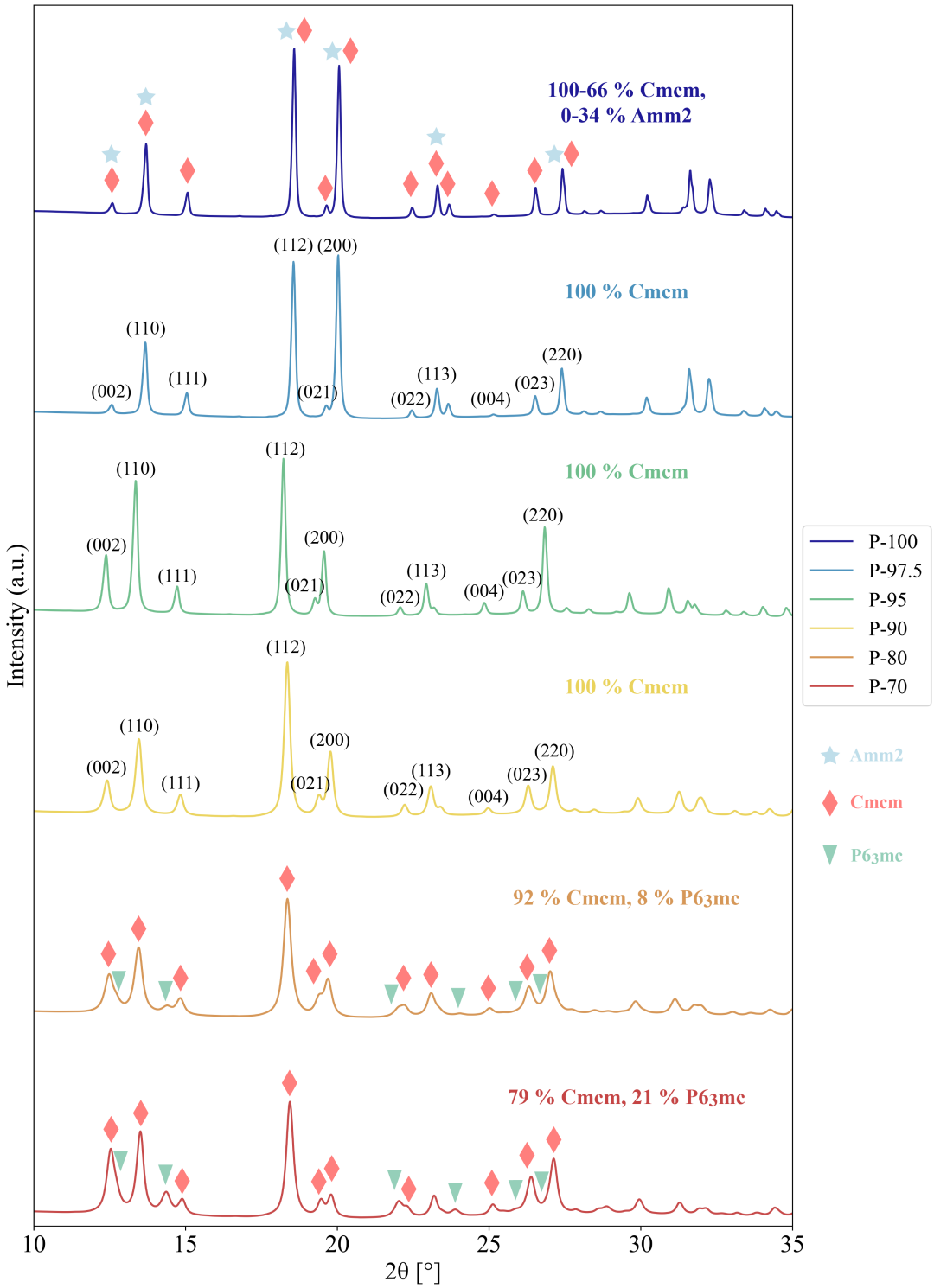

Figure 4.9: X-ray diffractograms of all pressed crystal samples P-100, P-97.5, P-95, P-90, P-80 and P-70. For P-97.5, P-95 and P-90, peaks are labeled with Miller indices. For P-100, P-80 and P-70, contributions from phases are annotated with symbols. Estimated phase percentages are also included.

4.4 Phase transitions

Phase transitions were investigated in all powder samples C-100 to C-70 through DSC measurements since the mesophase transition is a fingerprint characteristic of a plastic crystal and hence a useful feature to study the effect of chemical composition. Due to instrument malfunctions, the cooling rate was not able to be controlled despite being reduced from 10 to 5 K/min as described in Section 3.3.3. The actual experienced temperature programs can be seen in Appendix B. Consequently data could only be taken from heating. The data from heating between 60 and 140 °C for all samples C-100, C-97.5, C-95, C-90, C-80 and C-70 is presented in Figure 4.10. The peak indicating a phase transition is located at ~115 °C for samples C-100 and C-97.5, though with a slight shift to a lower temperature for the latter. The peak also broadened and reduced in intensity for C-97.5 compared to C-100. Samples C-95 to C-70 all show a DSC peak at ~100 °C. For C-90 the peak broadened and reduced in intensity, before it narrowed and increased again for C-80 and C-70. Also for C-80 and C-70, a shoulder and eventually a second peak appeared at slightly higher temperatures, between 105 and 120 °C, which could be associated with the appearance of another phase in the material.

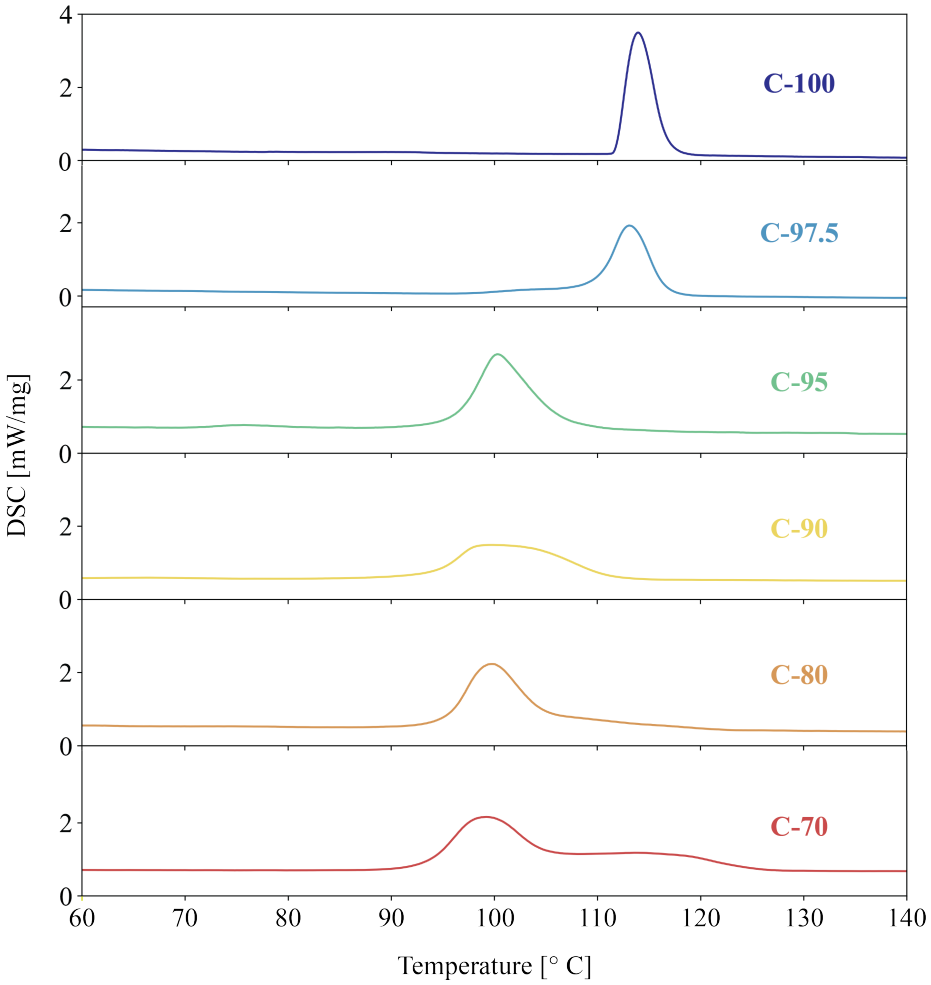

Figure 4.10: DSC curves between 60 and 140 °C for all powder samples: C-100, C-97.5, C-95, C-90, C-80 and C-70.

To estimate the enthalpy of the phase transitions, the area under the peaks in in Figure 4.10 was calculated for each composition, and the resulting enthalpies are plotted in Figure 4.11. When excluding the shoulder and second peak appearing for C-80 and C-70, the enthalpy reaches a maximum for C-95, whereas when the shoulder is included, the enthalpy follows an overall trend of increasing with decreasing mol% TMA^+.

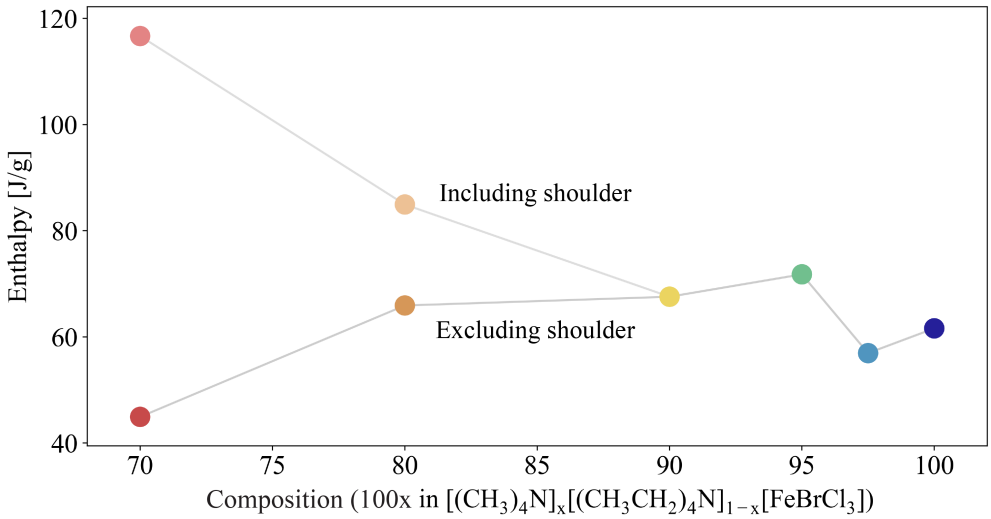

Figure 4.11: Estimated enthalpy as a function of chemical composition for all samples C-100 to C-70. Calculated from the area under the peaks in Figure 4.10. Data from both including and excluding the shoulders for C-70 and C-80 is shown.

4.5 Low-field electrical response

The low-field electrical response of a material gives information on dielectric properties, and is therefore useful for comparing materials as a function of chemical composition. The real part of the permittivity and the loss tangent were measured for all pressed samples P-100 to P-70 through impedance spectroscopy. Figures 4.12 and 4.13 show the results for respectively the real permittivity and the loss tangent. Both figures contain the entire range from 10^{-2} to 10^{6} Hz, and Figure 4.12 also has an inset with a close-up. The values displayed are the mean values from 2 or 3 pieces measured from the same pressed pellet. Error bars showing the standard deviation have also been included.

The measured real relative permittivities of all samples P-100 to P-70 all had a long plateau for most of the frequency range before increasing in value at lower frequencies. In the plateau region, values were between 40 and 60 for the different samples, with no strict trend as a function of composition. The measured permittivity decreased first from P-100 to P-95, the latter of which gave the lowest measured values, but increased to the highest values measured (in the plateau) for P-90. After this, the measured permittivity decreased for P-80, but increased again for P-70. It should be noted that the standard deviation was significantly higher for P-100 than for any other sample, and all other mean values but those for P-95 and P-90 lie within the span of the error bars of P-100 in the plateau region.

The loss tangent overall increased with decreasing frequency for all samples. The measured values diverged at higher and lower frequencies, but remained fairly similar in the range 10^0 to 10^2 Hz. At high frequencies (e.g. 10^5 Hz), the loss tangent was measured to be between 10^{-4} and 10^{-2} for all samples, while at low frequencies such as 10^{-2} Hz all values are greater than 1. Looking at the regions of higher and lower frequencies, the loss tangent is slightly lower with higher content of TEA^+, but this is no strict trend and standard deviations in these regions are also significantly large.

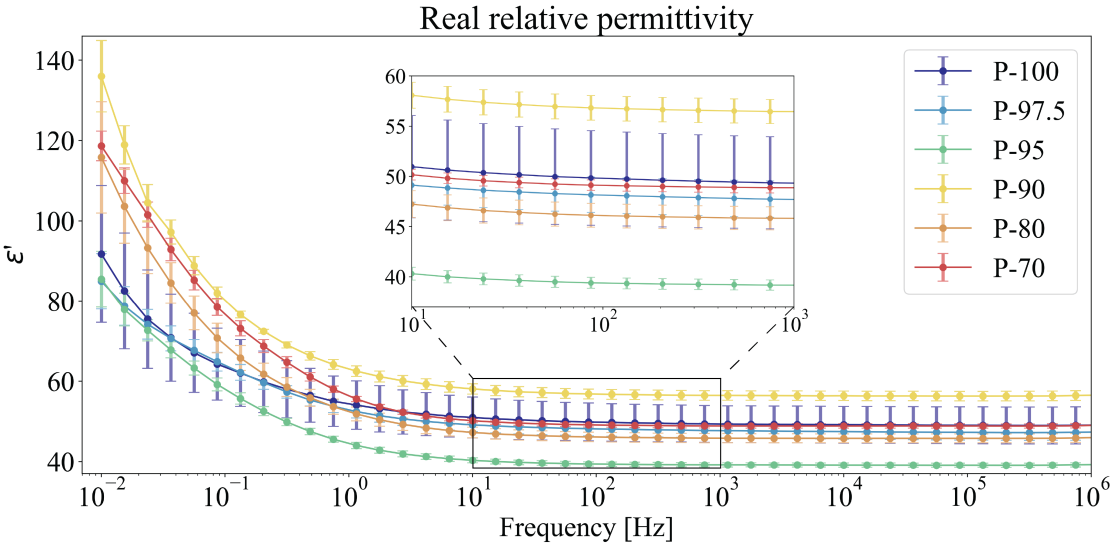

Figure 4.12: Real relative permittivity as function of frequency for all pressed samples P-100 to P-70 in the 10^{-2} to 10^6 Hz range. Error bars show standard deviations.

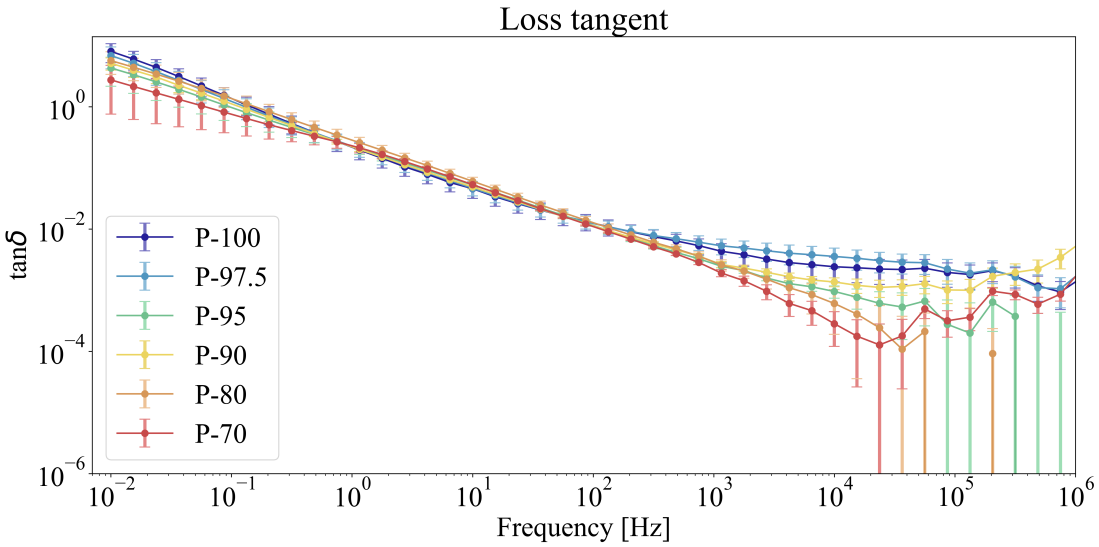

Figure 4.13: Loss tangent as function of frequency for all samples P-100 to P-70 in the 10^{-2} to 10^6 Hz range. Error bars show standard deviation, and at high frequencies have they been cut off.

4.6 Polarisation and polarisation switching

High-field electrical measurements were performed to determine whether the various compositions were ferroelectric and identify any potential trends in ferroelectric properties with composition. Characteristic hysteresis behaviour was induced only in P-100 and P-97.5. The hysteresis curves of the respective samples can be seen in Figures 4.14 and 4.15. Several cycles at 180 kV/cm were neccessary to open up the polarisation loop for P-100, which at first displayed only linear dielectric behaviour. After starting to show ferroelectric behaviour, the polarisation continued to increase with persisting cycling, but the increase appeared to slow down after 10 cycles. The J-E loop developed its characteristic peaks simultaneously with the opening of the polarisation hysteresis loop. The S-E field measurements displayed only an S-shape at the early stages of cycling, but eventually evolved into the characteristic butterfly-shape with increased number of cycles. The small sharp peaks in the J-E loops are most likely the result of leakage current events.

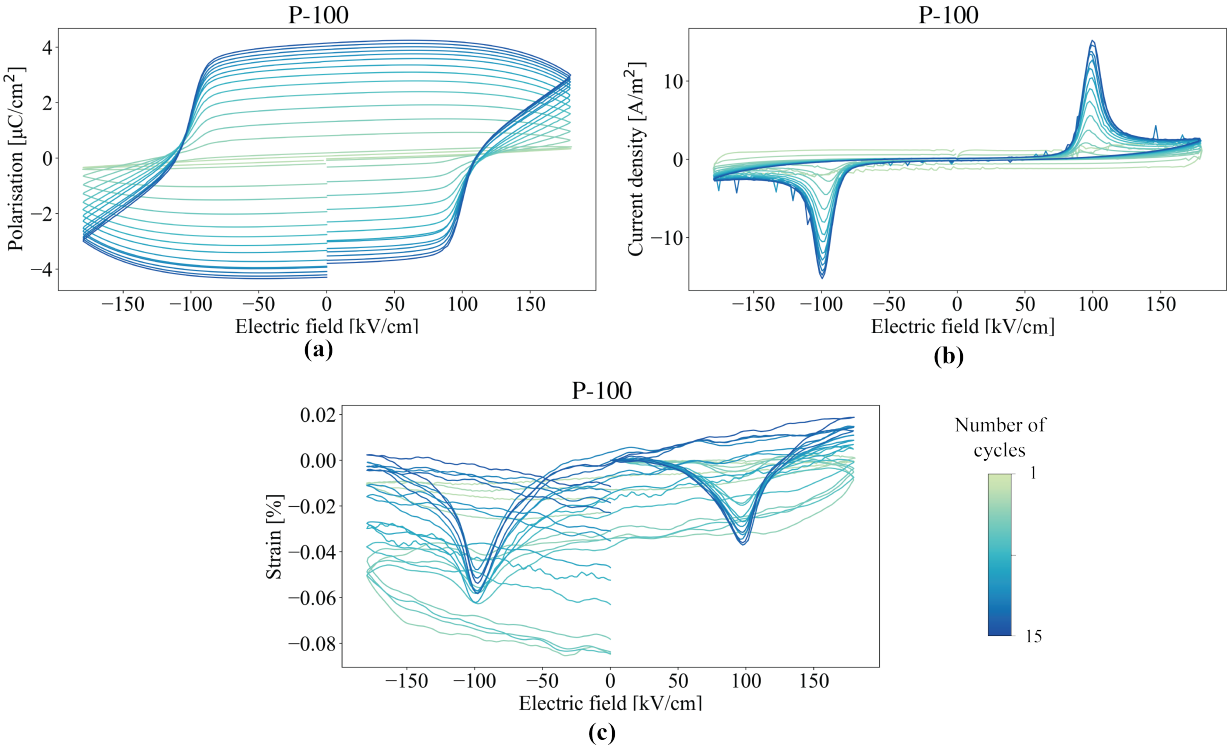

Figure 4.14: (a) P-E, (b) J-E and (c) S-E hysteresis curves for the P-100 sample after repeated cycling at 180 kV/cm.

To induce ferroelectric behaviour in the P-97.5 sample, higher fields than 180 kV/cm were required and the field was therefore driven up to 200 kV/cm. As can be seen in the P-E loops in Figure 4.15 (a), indications of a polarisation loop can be seen already at 180 kV/cm, but at this stage the peaks in the J-E loop (in (b)) were very low and the S-E curve (in (c)) was only noise. With cycling at 190 and eventually 200 kV/cm, polarisation and peak current density increased. At 190 kV/cm, the butterfly loop was very asymmetrical and at negative field amplitudes the strain signal did not "dip" as it did for positive field amplitudes. However, after cycling at 200 kV/cm, the full characteristic butterfly loop was eventually achieved. The S-E plot is cut off at -0.02 % despite

lower measured values, as these are not considered physical measurements but rather to be a result of the equipment set-up. More leakage current events (arcing) are visible for the P-97.5 sample compared to P-100.

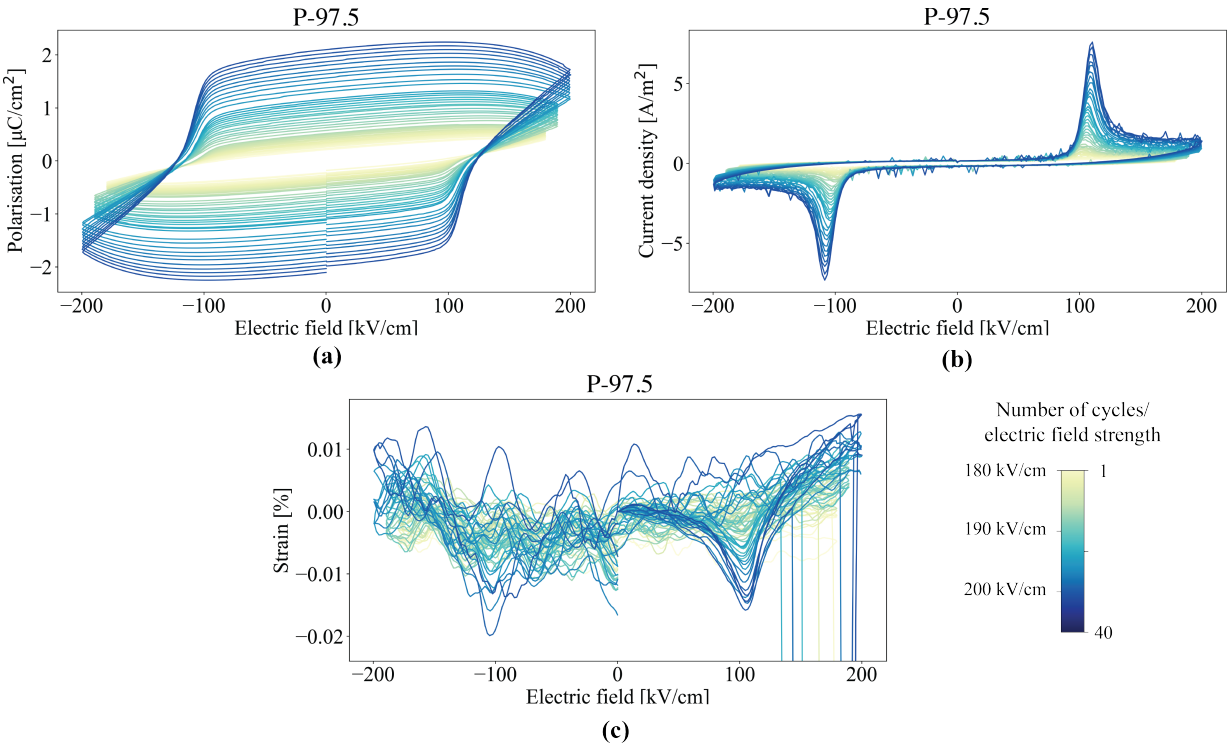

Figure 4.15: (a) P-E, (b) J-E and (c) S-E hysteresis curves for the P-97.5 sample after repeated cycling at 180 to 200 kV/cm kV/cm.

Important ferroelectric parameters are summarised for the P-100 and P-97.5 samples in Table 4.4. For P-100, the remanent polarisation at positive and negative field amplitudes was respectively 4.14 and -4.30 μC/cm^2, while for P-97.5 these parameters had decreased to ±2.10 μC/cm^2. The same was the case for the peak current densities (from 15.20/-15.25 to 7.59/-7.32 A/m^2) and the peak-to-peak strain (0.055 to 0.037 %). The coercive field, however increased with more than 10 kV/cm from P-100 to P-97.5.

Table 4.4: Electrical parameters of P-100 at 180 kV/Cm and P-97.5 at 200 kV/cm.

Sample	P_{r+} [μC/cm^2]	P_{r-} [μC/cm^2]	E_{c+} [kV/cm]	E_{c-} [kV/cm]	J_{p+} [A/m^2]	J_{p-} [A/m^2]	S_{pp} [%]
P-100	4.14	-4.30	110.0	-110.5	15.20	-15.25	0.055
P-97.5	2.10	-2.10	123.3	-122.0	7.59	-7.32	0.037

The remaining samples, P-90 to P-70, did not produce ferroelectric hysteresis loops even after extensive cycling at high field amplitudes. At 200 kV/cm, all four samples had the same loop indicative of a leaky dielectric. These loops are plotted together in Figure 4.16 (a). There is little variation between the loops both in remanent polarisation and peak-to-peak polarisations, the latter of which is plotted as a function of composition in Figure 4.16 (b). Though the variation is minor, a maximum can nevertheless be found for P-90. J-E and S-E measurements of these samples

similarly did not display characteristic ferroelectric behaviour. Appendix C shows the full plots with increasing number of cycles at 200 kV/cm for P-E, J-E and S-E measurements of P-95, P-90, P-80 and P-70.

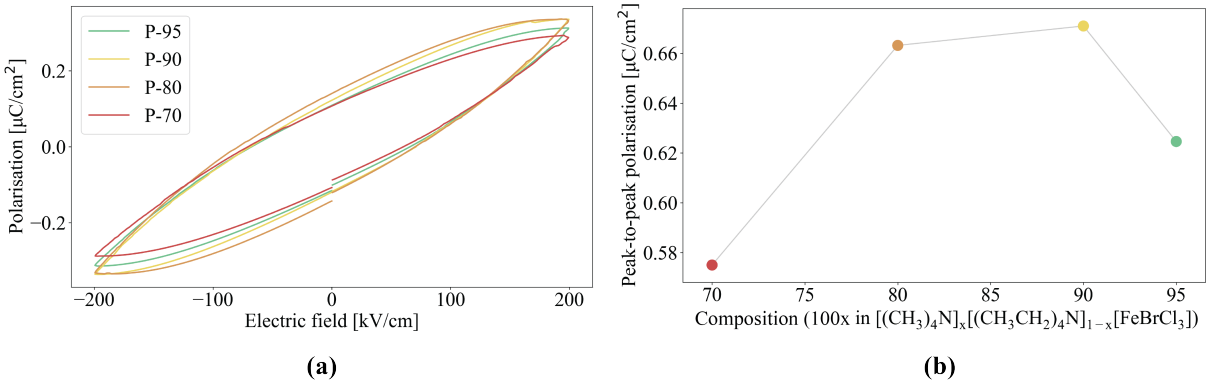

Figure 4.16: P-E loops for P-95 to P-70 and peak-to-peak polarisation (P_{pp} for the same samples. A maximum in P_{pp} was found for P-90.

For the P-95, P-90, P-80 and P-70 samples, field amplitudes were also driven higher and lower frequencies were used in an attempt to induce ferroelectric behaviour. The samples nevertheless retained dielectric behaviour. Figures 4.17 and 4.18 show the polarisation and current density loops for P-95 at field amplitudes up to 290 kV/cm at 10 Hz, and P-80 at field amplitude 260 kV/cm but with frequency diminishing from 10 to 1 Hz. The large noise in the current density measurements is due to leakage behaviour, and is expected at high fields. The increase in polarisation for P-80 between 10 and 1 Hz was larger than it was for P-95 between 200 and 290 kV/cm. The maximum field amplitude applicable was limited by instrument and the thickness of the samples, and therefore varied for the individual samples: 290 kV/cm was the maximum for P-95, while 260 kV/cm was the maximum for P-80. The values for P-90 and P-70 were even lower, as indicated by their thickness (Table 4.1).

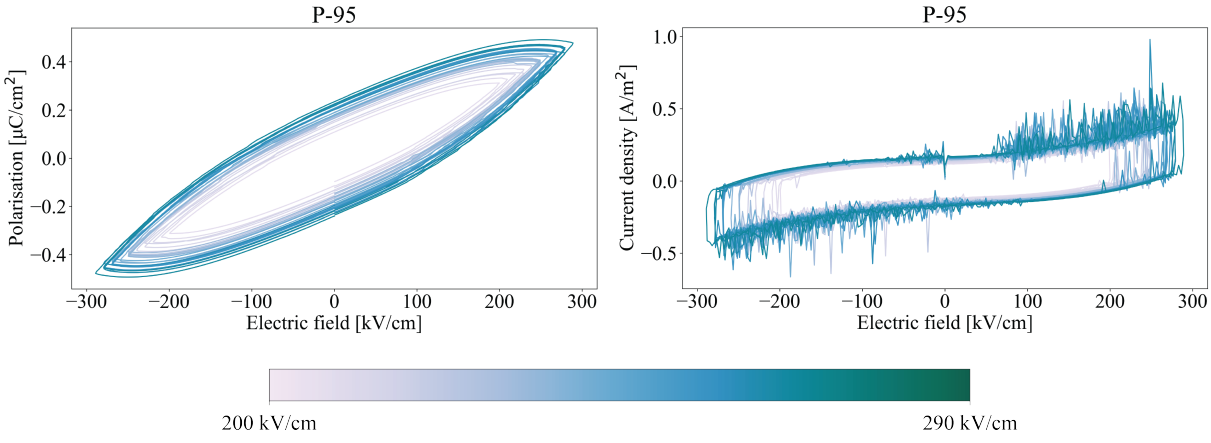

Figure 4.17: P-E and I-E loops for P-95 with increasing field amplitudes at 10 Hz.

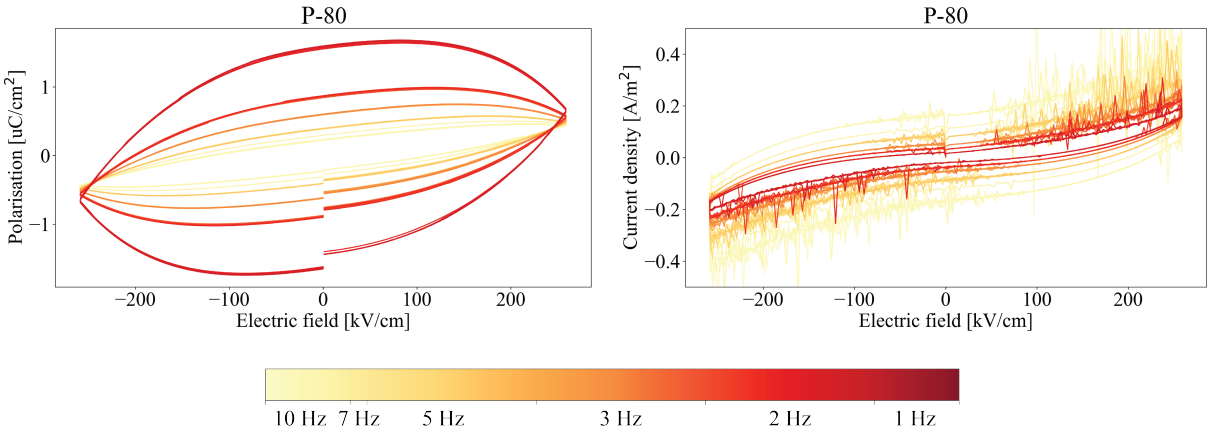

Figure 4.18: P-E and I-E loops for P-90 at 260 kV/cm with diminishing frequencies.

Frequency sweeps between 100 and 1 Hz were performed before and after driving the samples to high fields, for all pressed samples but P-100. Figure 4.19 shows the resulting polarisation curves for P-97.5 and P-90. For P-97.5 ((a) and (b)) there is an increase in apparent polarisation for all frequencies after cycling. The difference is more pronounced at higher frequencies. For all the dielectric samples (P-95 to P-70), there was no difference before and after cycling, as demonstrated for P-95 in Figure 4.19 ((c) and (d)).

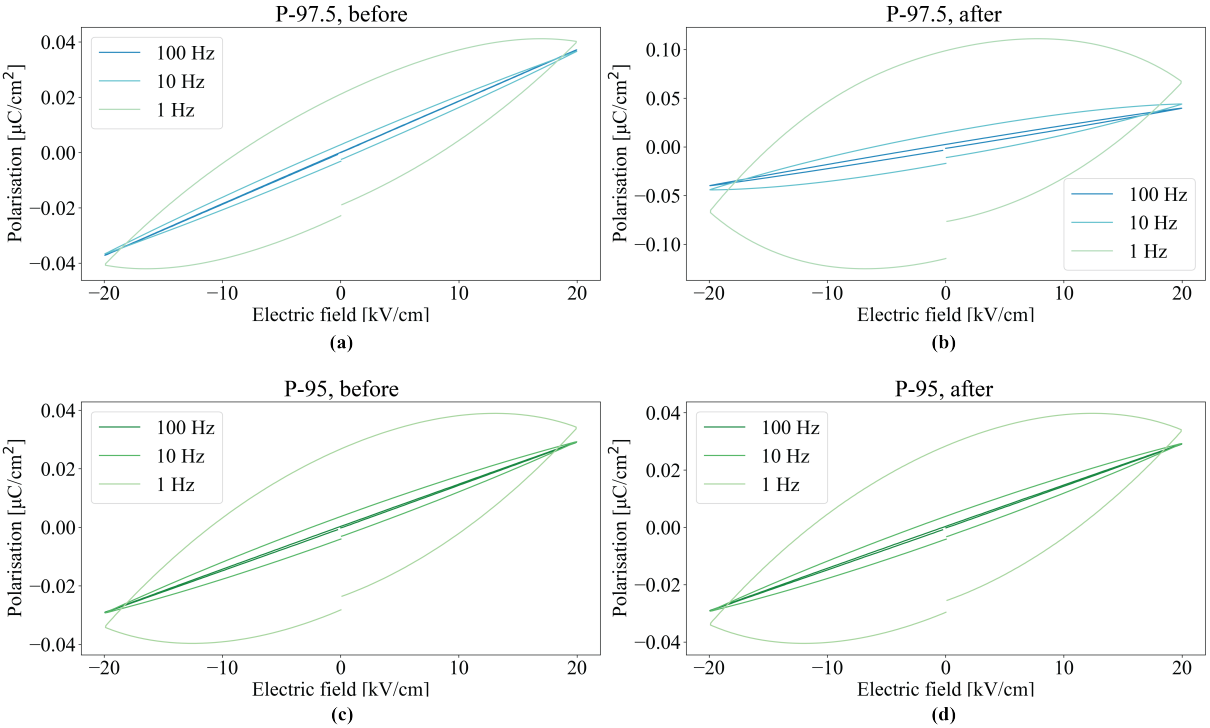

Figure 4.19: Frequency sweeps before ((a) and (c)) and after ((b) and (d)) high-field cycling for P-97.5 and P-95.

Chapter 5

Discussion

This thesis has, through several characterisation techniques, studied the synthesis, structure and functional properties of $TMA_xTEA_{1-x}FeBrCl_3$ (x = 1 - 0.7). The findings can be grouped into three main categories: The effect of annealing on morphology and crystal structure, phase composition as a function of chemical composition and pressing, and electrical properties. The subsequent discussion will therefore share a similar division: First, general observations from synthesis and annealing will be discussed. An in-depth discussion of the crystal properties will follow, divided into sections on crystal structure and electrical properties.

5.1 Considerations from synthesis: Yields and the effect of annealing

Two different synthesis methods were utilised to produce crystals of end members $TMAFeBrCl_3$ and $TEAFeBrCl_3$, where the yield for the latter was significantly higher than for the former. The low yield is believed to be a result of using 96 % ethanol during synthesis rather than 99.9 %. The majority of the impurity in the 96 % ethanol, meaning the remaining 4 % that are not ethanol, is made up of water. Considering that the $TMAFeBrCl_3$ crystals are much more soluble in water than ethanol,[15] this water impurity is believed to be the cause of the reduced yield during crystallisation. The use of highest purity ethanol can therefore be considered a requirement for efficient production through this synthesis route, with maximised yield. $TMAFeBrCl_3$ crystals can also be crystallised slowly, as the $TEAFeBrCl_3$ crystals were, but previous studies[15] experienced a slowing of the process (compared to that of $TEAFeBrCl_3$) and the presence of amorphous material in the final product, making this synthesis route less beneficial.

As a part of the synthesis route, mixtures containing C-TMA1, C-TMA2 and C-TEA were annealed at 240 °C. SEM imaging of mixtures before and after the annealing step revealed information about what happened during the high-temperature processing, but also about the morphologies of the pure $TMAFeBrCl_3$ and $TEAFeBrCl_3$ crystals. Dendritic crystals were present in the C-90 sample, as expected since the mixture contained Amm2, which favours this structure. The C-100 mixture had been more thoroughly crushed before imaging, which could explain why dendrites were not as easily found here. However, long rod-shaped particles such as the one in Figure

4.4 (b) could be the remanents of a dendrite where the branches had been broken off due to the crushing process. The C-90 mixture imaged before annealing curiously lacked clear hexagonal structures, which would have been indicative of $P6_3mc$. Previous studies on the crystallisation of $TEAFeBrCl_3$ crystals[15] indicate that slow crystallisation should result in faceted particles with clear hexagonal geometry, while quicker crystallisation is more prone to give irregularly shaped particles. The lack of faceted, hexagonal particles in the mixture could be due to the limited sample volume investigated, or could come as a result of the crushing process.

Before annealing, the particles of the mixture had irregular surfaces with sharp edges. After annealing, the particles had coarsened and sharp edges become round. This could be indicative of surface diffusion processes happening during annealing, as these processes are expected to be activated at these temperatures. However, during the annealing the material also transitions into the plastic mesophase (transition at 110-120 °C for $TMAFeBrCl_3$). Thus, plastic deformation could occur, which could explain changes in morphologies, but not the coarsening of the particles. The evidence of necking seen after annealing is another sign of diffusion and solid state reactions, suggesting that diffusion across the interface between particles happened and a more homogeneous product was achieved. This is also supported by the XRD analysis of C-90 before and after annealing: Before annealing, the sample consisted of a majority Amm2 and minority $P6_3mc$ phase, while after, the only phase of C-90 was suggested to be the Cmcm phase. This supports the theory that the particles underwent solid state reactions to a homogeneous product, as was indicated by necking. Furthermore, it is in line with observations from studies of a similar composition ($TMA_{0.95}TEA_{0.05}FeBrCl_3$) at the same annealing temperature.[1]

5.2 Crystal structure of powder and pressed samples

5.2.1 Crystal structure as a function of composition

All compositions were found to have a majority Cmcm phase after annealing, however, three out of six crystal samples also had a minority phase present. For the C-100 crystals, this minority phase had the Amm2 structure, which as mentioned in Section 2.4.1 is the stable structure of $TMAFeBrCl_3$ at lower temperatures than Cmcm. The presence of the Amm2 minority phase could be explained by the sensitivity of the Cmcm to Amm2 transition on external parameters. This has been highlighted in earlier studies that show the transition temperature on cooling is slow and diffuse.[59] As this diffuse transition begins near room temperature, phase mixtures of Amm2 and Cmcm in materials that have been thermally cycled is not uncommon. Moreover, the cooling rate after annealing was not controlled and was very slow, which could have given a prolonged period during which Amm2 could precipitate out. Interestingly, when introducing TEA^+ cations into the structure, the Cmcm structure is stabilised as the only phase after annealing despite an equally long cooling time, as seen in C-97.5, C-95 and C-90.

Cmcm being the only phase present in the C-97.5, C-95 and C-90 samples, as indicated by Rietveld refinement, would imply that a solid solution was obtained in this compositional range, with TEA^+ filling lattice sites of TMA^+ in the crystal structure of the latter. This would also mean that Cmcm is stabilised over a larger temperature range than for pure, undoped $TMAFeBrCl_3$. As seen in Table 4.2 and reiterated in Figure 5.1, the Cmcm lattice parameters increase very slightly from C-100 to C-97.5, when TEA^+ ions are incorporated into the structure. There is however a much

more significant leap in lattice parameters between C-97.5 and C-95, simultaneously with continued addition of these ions. The lattice parameters decrease significantly between C-95 and C-90, despite theoretically having incorporated more TEA^+ ions into the lattice. The GOF of the C-90 XRD refinement was also slightly higher than the previous ones. A refinement including $P6_3mc$ was also attempted for this composition, but it produced only marginally better numbers and all peaks in the diffractogram were fitted to Cmcm even when including a second phase. Therefore the refinement with only Cmcm was used. The reduced GOF shows that the structure does not match pure Cmcm as well as the 95 mol% composition does, despite the inability to identify any other phase. However, the reduced lattice parameters suggest that something more complex could be happening. Thus it is possible that the structure at 90 mol% resides close to a compositionally induced phase boundary or a solubility limit for TEA^+ in $TMAFeBrCl_3$. This would give an explanation for the observations made in both the structure and the phase transition, as discussed below.

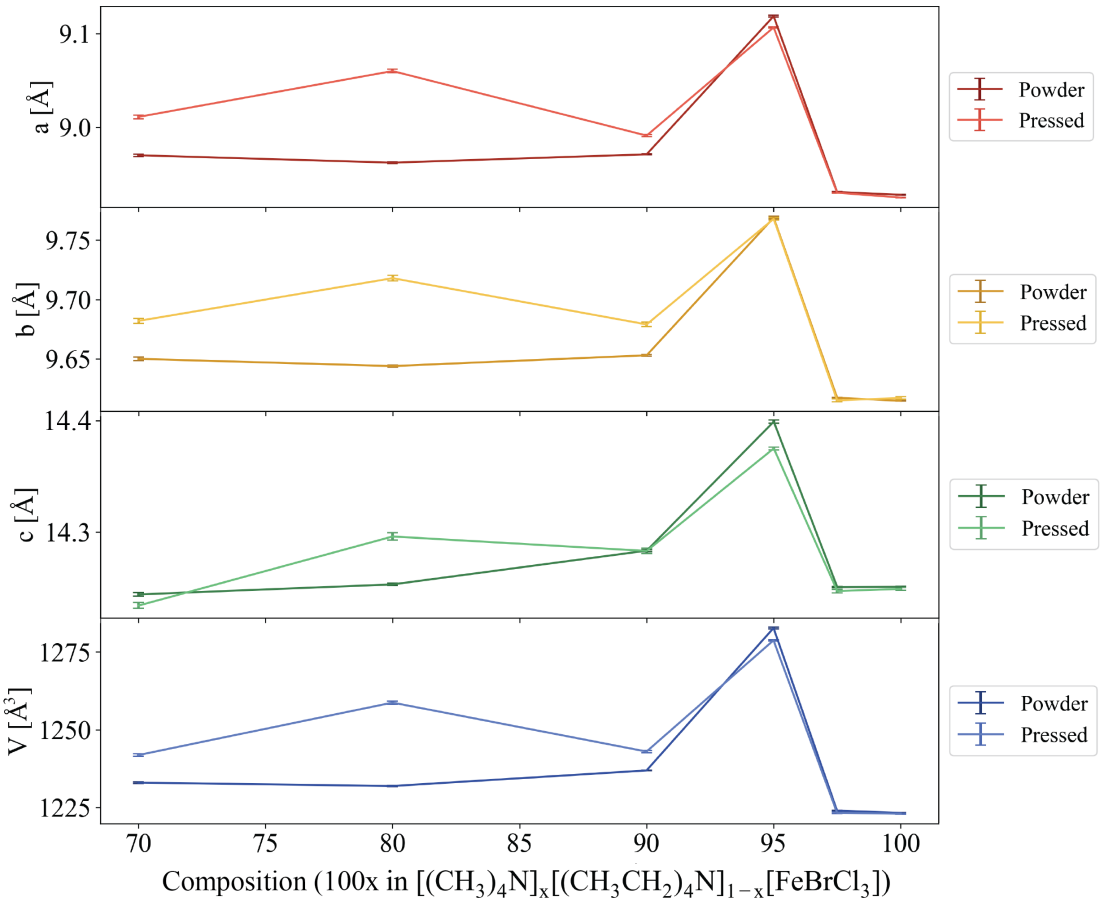

Figure 5.1: Estimated Cmcm lattice parameters of all powder and pressed samples from Rietveld refinement. Error bars are based on error estimates from TOPAS.

Below 90 mol% TMA^+ cations, the system once more separates into two phases, with $P6_3mc$ appearing in addition to Cmcm. This is not unexpected, as this structure is favoured by $TEAFeBrCl_3$ and we have shifted so far away from the $TMAFeBrCl_3$ end member that the making of solid substitutions become challenging. The system is now more likely to separate into phases of the respective end members. This is reflected in the correspondence between the suggested phase percentages of the crystals and the chemical compositions, 87/13 compared to 80/20 and 75/25

compared to 70/30 Cmcm/$P6_3mc$ for C-80 and C-70 respectively. The DSC data supports the suggested increase in $P6_3mc$, as the shoulder appearing in the data for C-80 grows significantly larger for C-70. If this peak is attributed to the emerging $P6_3mc$ phase, a larger peak means more material will go through a transition, and consequently more of the crystals should be in the $P6_3mc$ phase in C-70 compared to C-80.

When considering the emergence of $P6_3mc$ in the C-80 and C-70 samples along with the decrease in lattice parameters between C-95 and C-90, this could be an indication that the transition from single phase Cmcm to double phase Cmcm and $P6_3mc$ occurs in the vicinity of the 90 mol% TMA^+ chemical composition. Since laboratory XRD would not be able to detect trace amounts of a $P6_3mc$ structure, it is not possible to completely dismiss the possibility that the phase separation has commenced already here. Moreover, DSC and dielectric measurements can also be used to argue this case. The peak for the phase transition in the C-90 sample was different from both preceding and succeeding samples, with a broader and lower peak. This could be an indication that the system is unstable at this composition, and that phase separation is becoming likely. The dielectric data could also point to this, as the measured P-90 real permittivity is much higher than the measured values for other samples.

Comparing the structural information gained from XRD and indicated by DSC and dielectric data to the tentative phase diagram presented in Section 2.4, we find discrepancies in several regions. The tentative phase diagram suggests phase separation happening already before the 90 mol% composition, as well as $P6_3mc$ being the only phase present at 70 mol% TMA^+. The findings in this thesis rather point towards relocating the line between single phase Cmcm and the phase separated system Cmcm + $P6_3mc$ in proximity to 90 mol% TMA^+, and pushing the eventual line between the Cmcm + $P6_3mc$ and pure $P6_3mc$ systems to a place below 70 mol%. However, the synthesis method forming the basis for the tentative phase diagram and the one utilised in this thesis are not the same, so direct comparison with this phase diagram should not be a focus.

5.2.2 The effect of pressing on crystal structure

XRD analysis of the pressed samples largely displayed good correspondence with that of the powder samples, as phases present in the powder samples were also detected in the pressed samples. Furthermore, the phase percentages remained relatively consistent across pressing. The biggest deviation is found in samples C-100 and P-100. While before pressing, phase percentages for the Cmcm and Amm2 phases were elucidated without particular complications, the diffractogram from the pressed samples was not as easily analysed. The shoulders and several peaks found in the diffractogram for C-100 indicative of Amm2 were not present in P-100, and therefore analysis of the pressed sample was not as conclusive. Since a fit for only Cmcm was as good as one also including Amm2, it is possible that the Amm2 phase disappeared during pressing. This would concur with previous studies of the effect of pressing on $TMAFeBrCl_3$, where 100 mol% Amm2 samples during pressing to varying extent transitioned into the Cmcm phase.[59] Thus, it is likely that the amount of Amm2 diminished after pressing, since no peaks for the phase were present and similar materials have exhibited such behaviour.

The remaining samples had phase compositions comparable to those of the corresponding powder samples. P-97.5, P-95 and P-90 consisted of only single phase Cmcm, meaning the pressing had no effect on the phase composition for these samples. For P-80 and and P-70, the estimated number

for the Cmcm phase percentage is slightly higher after pressing, but the increase is not significant and within the error associated with laboratory XRD. No conclusion can therefore be met regarding the exact effect of pressing on these samples. Moreover, the diffractograms for the P-90, P-80 and P-70 samples were of a lesser quality than the other samples, with high noise, which complicates the refinement process.

The estimated lattice parameters of the pressed samples are plotted together with those of the powder samples in Figure 5.1. The overall trend is that while there is little to no change for the C-100, C-97.5, P-100 and P-97.5 samples, the unit cell volume decreases for P-95 and increases for P-90, P-80 and P-70. The individual parameters vary, meaning distortion of unit cells happened during pressing. Such distortions could be a result of the pressure and plastic deformation of crystals during hot pressing.

Comparing X-ray diffractograms of C-97.5 and P-97.5 (Figure 5.2) illustrates another possible effect of the pressing process: Grain texturing, i.e. distribution of crystallographic orientations. Relative intensities decreased in many reflections, in particular (002), (110) and (112), while a large increase is visible for the (200) reflection. The substantial reduction in the (002) and (112) peaks give a strong indication that there is a change in the texture of the *c* lattice parameter. The reduction points towards the *c* lattice parameter likely orientating preferentially in the plane. Previous studies have suggested that structural orientation is a possible side-effect of the pressing process.[13] Considering this for the P-97.5 sample, a preferred [200] orientation can be suggested. This outcome could unlock great potential for the engineering of electrical or electromechanical properties such as dielectric constants and piezoelectric coefficients, as these have strong orientational dependencies.[60,61] However, the preferred orientation after pressing is not the same for all pressed samples, meaning a way must first be found to control the orientational preference in order to utilise benefits thereof.

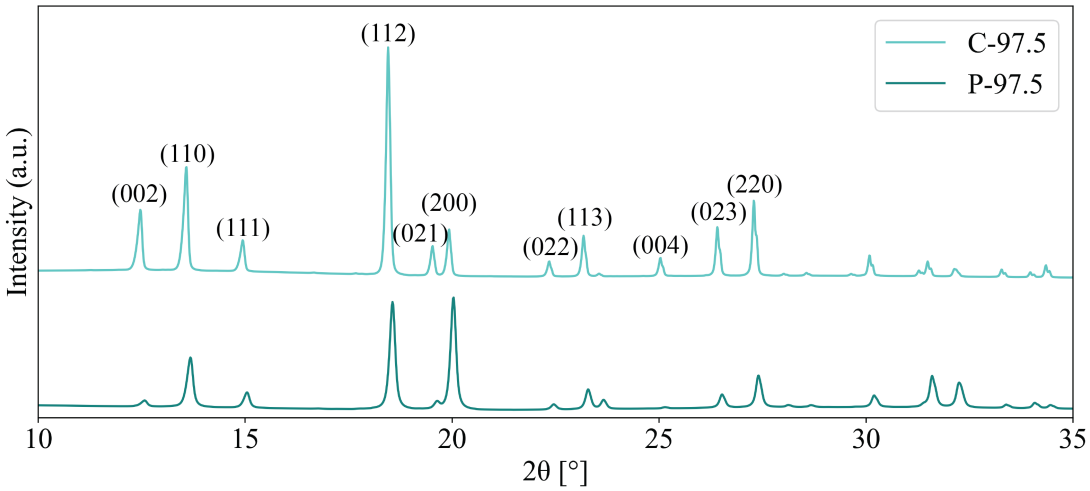

Figure 5.2: X-ray diffractograms of C-97.5 and P-97.5. Peaks are labelled with Miller indices of the Cmcm space group.

5.3 Electrical properties

The current section discusses the results from the electrical measurements in more detail and will be divided into two subsections, each devoted to either dielectric spectroscopy (low-field) or ferroelectric testing (high field).

5.3.1 Low-field electrical response

The measured permittivities in this thesis ranged from 40 to 60 for most of the frequency range. These values deviate significantly from reported values of $\lesssim 20$[12,13] and 15-30[15] for materials of the same compositions. It should be noted that the materials characterised in this thesis have been synthesised via a different method than ones from similar studies. Comparing values at lower frequencies, e.g. 10^2-10^3 one finds correlation between values reported here and by Walker et al.[13] As seen in Figure 5.3, at 10^2 Hz the permittivities were measured to be 40-60, however, these values are the same also at higher frequencies. The measured permittivities of Walker et al.[13] at 10^2 Hz come after an increase associated with relaxation, meaning the permittivities are lower at higher frequencies. The discrepancy between the measured magnitude of the permittivity in this project compared to reported literary values could be related to the need for a low permittivity range calibration during measurements, however, this needs to be investigated further in future work. The use of the same instruments for all samples means measurements are self-consistent and relative variations between samples of different chemical compositions are valid.

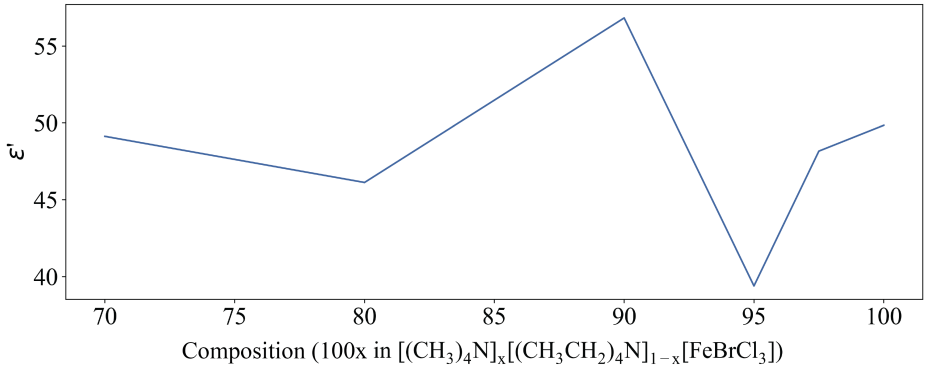

Figure 5.3: Real relative permittivity at 10^2 Hz as function of chemical composition.

There was little variation between the measured permittivities of the samples, and the points of several samples were located within the error bars of others (in particular of P-100). The relative permittivity first decreased with increase of TEA^+ content, an observation that corresponds decently with those of other studies.[15] The highest values of all chemical compositions were measured for P-90. As previously discussed, this might be the location of a compositionally induced phase transition from a single to double phase system. This could provide an explanation for the increase in permittivity, as that would be expected based on literature surrounding MPBs in ferroelectric materials (Section 2.2.4). When the sample has phase separated into Cmcm and $P6_3mc$, permittivities are measured to be higher than for the solid substitution in P-95, yet lower than for the transition point in the vicinity of P-90. When several phases are present, the contributions to the permittivity arise from the various phases present. Since $P6_3mc$ has a higher permittivity than

Amm2 or Cmcm, this explains the increase in permittivity for P-80 and P-70. Furthermore, the difference in texturing of the pressed samples is also expected to cause variations in measured permittivity, but additional work is necessary to deconvolute the impact this has on the measured values.

The loss tangents measured for all the pressed samples P-100 to P-70 were consistently similar in the 10^0 to the 10^2 Hz range, however, above and below they deviate from each other. The reason for this is not known. There is indication of a tendency for the loss tangent to decrease with increasing amount of TEA^+ at both higher and lower frequencies, however this is no strict trend and the error bars in these regions are large for many samples.

5.3.2 Polarisation and polarisation switching

Ferroelectric behaviour was found in the P-100 and P-97.5 samples, while the remaining samples had dielectric behaviour at all obtainable field amplitudes. Coercive fields were found to be respectively 110.3 and 122.7 kV/cm, while remanent polarisation was 4.22 and 2.10 μC/cm^2. Comparing these values to those of bulk perovskites, where values may range from 0.5 to 150 kV/cm and 20-50 μC/cm^2,[34] the reported coercive field values can be considered high and the remanent polarisation values low. The values of P-100 are more comparable to those reported for similar materials.[50] The remanent polarisation values of P-97.5 are smaller than reported for similar materials ($TMAFeBrCl_3$) at the same field strength (200 kV/cm)[50], and also lower than reported values from investigations at lower fields such as 3.3 μC/cm^2 at 120 kV/cm^2,[12] or 2.9 μC/cm^2 at 80 kV/cm^2.[13]

Ferroelectric behaviour is expected from the orthorhombic, non-centrosymmetric Amm2 structure, however, it is not for the centrosymmetric Cmcm structure. For the P-100 sample, where the Amm2 phase may or may not be present after pressing (as discussed in Section 5.2.2), the ferroelectric behaviour of the sample could have been used as an argument for the existence of an Amm2 phase. However, this argument falls short when taking also P-97.5 into account, where in a single phase Cmcm structure, ferroelectric behaviour nevertheless was induced. Previous studies have suggested that a field-induced transition from Cmcm to Amm2 is possible.[59] This would explain how a material believed to have a completely centrosymmetric structure could be ferroelectric.

Previously discussed was the possibility that introducing TEA^+ cations into the structure stabilised the Cmcm structure as the most stable structure at room temperature. Looking also into the electrical properties, this argument could be taken one step further: Given that the ferroelectric behaviour of P-97.5 is indeed a result of a field-induced transition into the Amm2 phase, this should have theoretically been possible also for P-95 and P-90, both of which are single phase Cmcm. However, this is not observed, and a possible explanation could be that these structures are more stable than the one in P-97.5. Higher field amplitudes (200 kV/cm) and a large number cycles (in total 40 between 180 and 200 kV/cm) were necessary to induce ferroelectric behaviour in the P-97.5 sample compared to P-100 (15 cycles at 180 kV/cm), which might be a result of there being a higher barrier for a field-induced transition for this sample. Furthermore, when ferroelectric behaviour ultimately was induced in P-97.5, ferroelectric parameters such as P_r and S_{pp} were lower than for the P-100 sample. This could mean there are fewer domains aligned to produce ferroelectricity, which could come as a consequence of there being fewer domains in total. A hypothesis

can therefore be made that a field-induced transition happened to a smaller extent for P-97.5 than P-100 due to increased stability of the structure and consequently a higher barrier for transition. The lack of ferroelectricity in P-95 could then be explained through increased stability and an even higher barrier for transition, that could not be overcome even after cycling at 290 kV/cm.

A composition of 90 mol% TMA^+ and 10 mol% TEA^+ cations was previously contemplated to be the location of a transition from a single to double phase system, therefore calling the structure of the P-90 sample more stable than that of P-97.5 might be considered erroneous. However, for this sample, a phase separation into Cmcm and $P6_3mc$ is likely more preferable than the formation of an Amm2 phase. An explanation for the missing ferroelectric behaviour in this sample despite a plausible lower stability than both P-95 and P-97.5 could therefore be that a phase separation into Cmcm and $P6_3mc$ and thus a stabilisation of the material happens before a field-induced transition into Amm2 can take place.

Common for both P-100 and P-97.5 is that the remanent polarisation was greater than the polarisation at maximum field amplitude (P_{max}). These parameters are plotted together in Figure 5.4 for all pressed samples (P-100 to P-70). A remanent polarisation higher than the polarisation at maximum field amplitude is often indicative of leakage currents contributing to the measured polarisation. When this is the case, the term *apparent remanent polarisation*, P_r^*, is better suited to describe the polarisation at zero applied field. Both P-100 and P-97.5 produced bloated P-E loops, meaning there was a substantial polarisation contribution from leakage currents in the samples.

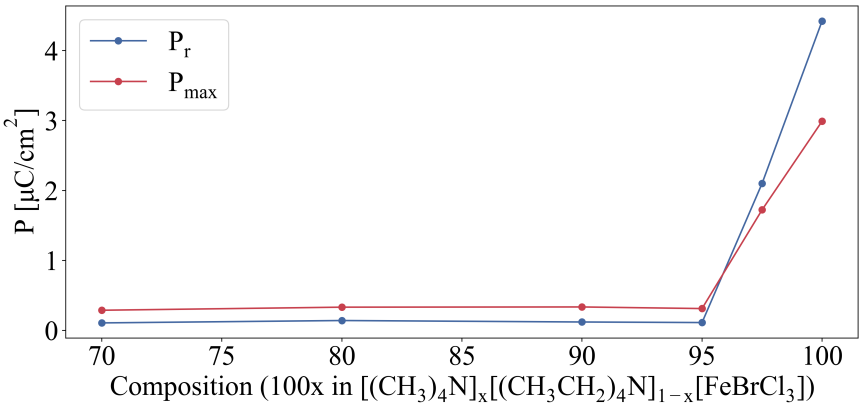

Figure 5.4: Remanent polarisation and polarisation at maximum field amplitude for all pressed samples P-100 to P-70.

For dielectric samples (P-95 to P-70), the remanent polarisation was lower than the polarisation at maximum field amplitude when applying a field with a frequency of 10 Hz. However, this changed with decreasing frequency, as evident from Figure 4.18. This increase in remanent polarisation can also be attributed to increasing leakage current contributions and has been observed also in other studies.[13]

Leakage currents also increased for the ferroelectric P-97.5 sample with decreasing frequency. This was the case both before and after cycling at high fields, but the increase was even higher after, suggesting an overall increase in leakage currents after high-field cycling. This is also visible in the high-field polarisation loops: When the starting and ending points for the applied field amplitude do not meet, this is an indication of conductivity in the sample.[34] Evident in both P-100 and P-

97.5 (but especially P-100) is an increasing gap between starting and ending fields with increasing number of cycles, meaning the conductivity of the sample is increasing already during the high-field cycling. This sort of fatigue is impractical for use in electronics, where the repetitive nature of device usage requires consistent and predictable behaviour over long time spans.

Chapter 6

Conclusion

This study sought to investigate the plastic crystal $TMA_xTEA_{1-x}FeBrCl_3$ solid solution systems with respect to structure, specifically phase composition, and functional electrical properties. Six compositions in the $TMAFeBrCl_3$-rich side of the system were synthesised through crystallisation from solution followed by solid state reactions through annealing. The effect of the annealing step was assessed through SEM imaging of samples before and after the heat treatment. Characterisation of phase composition and the effect thereof on electrical properties was done for all samples by means of XRD analysis, DSC measurements, dielectric spectroscopy and high-field ferroelectric testing.

Thermal treatment lead to a homogenisation of crystal compositions, indicated from XRD analysis as well as SEM imaging. Particle coarsening and evidence of necking suggested mass diffusion occurred during heating, facilitating a homogenisation of the crystal structure, that is, the formation of a single phase structure for most of the compositions. XRD analysis indicated the formation of a majority Cmcm phase for all powder samples.

Solid solutions were obtained at chemical compositions of 97.5, 95 and 90 mol% TMA^+ cations, where the structure of the samples were all single phase Cmcm. Above and below this compositional range, respectively minority Amm2 and $P6_3mc$ phases appeared, suggested to be the result of thermally sensitive transitions and a solid solubility limit of the TEA^+ cation in the orthorhombic $TMAFeBrCl_3$ structure, thus leading to phase separation. A compositionally induced phase transition from single to double phase system is proposed to lie in the vicinity of 90 mol% TMA^+, due to observations of anomalous dielectric and thermal behaviour. Hot pressing of powder samples produced pellets of mostly similar phase compositions, where there was evidence of grain texturing. The preferred orientation after pressing varied for different samples.

Electrical measurements revealed ferroelectric behaviour in two of the six samples: P-100 and P-97.5. P-97.5 was single phase Cmcm, while analysis of P-100 suggested the possibility of both single phase Cmcm and majority Cmcm with a minority Amm2 phase. The ferroelectric behaviour of P-97.5 is suggested to be the result of a field-induced transition to Amm2 at high field amplitudes. The same transition may or may not have occurred in P-100. The proposed reason for lacking ferroelectric behaviour in remaining samples is an increasing barrier for this field-induced transition, due to the stabilisation of the centrosymmetric Cmcm phase and the appearance of $P6_3mc$ phase, in which ferroelectricity has not yet been observed.

This project endeavoured to survey the functional properties of the $TMA_xTEA_{1-x}FeBrCl_3$ system in the $TMAeBrCl_3$ rich region, and attempt to produce solid solutions. A route to solid solutions for the investigated system has been distinguished, and the functional electrical properties identified. This work thus shows that it is indeed possible to create a homogenised plastic crystal solid solution in some compositional ranges and is the first demonstration of this approach in a plastic crystal ferroelectric. Thus this study is contributing to laying the foundations for the engineering of other plastic crystal compositions through a solid solution approach.

Chapter 7

Further work

While the results in this thesis have contributed to the understanding of the $TMA_xTEA_{1-x}FeBrCl_3$ solid solution systems, in particular regarding the formation of solid solutions and electrical properties, much research remains before the system is completely understood. The work performed also highlights some potential avenues for further investigation.

First and foremost, an extended part of the system should be investigated. The $TEAFeBrCl_3$ side of the phase diagram has during the current research remained completely untouched, but could present interesting opportunities for solid solutions with slightly different properties than those investigated here. Furthermore, probing more chemical compositions close to 90/10 TMA^+/TEA^+ would yield valuable data to be able to more accurately place the transition from single to double phase system.

Doing full DSC measurements, including both heating and cooling, would give further insight into the anomaly observed for C-90 and what happens to the entropy around the phase transition hypothesised in this region.

To delve deeper into the theory of a field-induced phase transition, finding a way to perform XRD analysis on samples as a function of electrical history, or in situ whilst applying an electric field, would give invaluable information. Another option is the production of thinner pressed samples from C-95 and C-90. If a thinner pressed sample upon application of higher field amplitudes show ferroelectric behaviour, it could be an argument for the validity of the theory.

Bibliography

[1] I. E. Holck, *Synthesis and investigation of the plastic crystal* $[(CH_3)_4N]_{0.95}[(CH_3CH_2)_4N]_{0.05}FeBrCl_3$. TMT4510 Nanotechnology Specialisation Project, NTNU, 2020.

[2] J. Valasek, 'Piezo-electric and allied phenomena in rochelle salt,' *Phys. Rev.*, vol. 17, pp. 475–481, 4 1921.

[3] M. E. Lines and A. M. Glass, *Principles and Applications of Ferroelectrics and Related Materials*. Clarendon Press: Oxford, 1977.

[4] A. von Hippel, R. Breckenridge, F. Chesley and L. Tisza, 'High dielectric constant ceramics,' *Industrial & Engineering Chemistry*, vol. 38, no. 11, pp. 1097–1109, 1946.

[5] S. Roberts, 'Dielectric properties of lead zirconate and barium-lead zirconate,' *Journal of the American Ceramic Society*, vol. 33, no. 2, pp. 63–66, 1950.

[6] G. Shirane and A. Takeda, 'Phase transitions in solid solutions of $PbZrO_3$ and $PbTiO_3$ (i) small concentrations of $PbTiO_3$,' *Journal of the Physical Society of Japan*, vol. 7, no. 1, pp. 5–11, 1952.

[7] A. King, 'Our elemental footprint,' *Nature materials*, vol. 18, no. 5, pp. 408–409, 2019.

[8] H.-C. Song, P. Kumar, D. Maurya, M.-G. Kang, W. T. Reynolds Jr., D.-Y. Jeong, C.-Y. Kang and S. Priya, 'Ultra-low resonant piezoelectric mems energy harvester with high power density,' *Journal of Microelectromechanical Systems*, vol. 26, no. 6, pp. 1226–1234, 2017.

[9] C. Bowen, H. Kim, P. Weaver and S. Dunn, 'Piezoelectric and ferroelectric materials and structures for energy harvesting applications,' *Energy & Environmental Science*, vol. 7, no. 1, pp. 25–44, 2014.

[10] A. S. Tayi, A. Kaeser, M. Matsumoto, T. Aida and S. I. Stupp, 'Supramolecular ferroelectrics,' *Nature chemistry*, vol. 7, no. 4, p. 281, 2015.

[11] S. A. Wilson, R. P. Jourdain, Q. Zhang, R. A. Dorey, C. R. Bowen, M. Willander, Q. U. Wahab, S. M. Al-hilli, O. Nur, E. Quandt *et al.*, 'New materials for micro-scale sensors and actuators: An engineering review,' *Materials Science and Engineering: R: Reports*, vol. 56, no. 1-6, pp. 1–129, 2007.

[12] J. Harada, N. Yoneyama, S. Yokokura, Y. Takahashi, M. Miura, N. Kitamura and T. Inabe, 'Ferroelectricity and piezoelectricity in free-standing polycrystalline films of plastic crystals,' *J. Am. Chem. Soc.*, vol. 140, pp. 346–354, 2018.

[13] J. Walker, R. Miranti, S. L. Skjærvø, T. Rojac, T. Grande and M.-A. Einarsrud, 'Supercoercive electric field hysteresis in ferroelectric plastic crystal tetramethylammonium bromotrichloroferrate (iii),' *Journal of Materials Chemistry C*, vol. 8, no. 9, pp. 3206–3216, 2020.

[14] D. Evans, A. Hills, D. Hughes and G. Leigh, 'Structures of tetraethylammonium tetrachloroferrate (iii) and the mixed halide iron (iii) complex, $[NEt_4][FeBrCl_3]$,' *Acta Crystallographica Section C: Crystal Structure Communications*, vol. 46, no. 10, pp. 1818–1821, 1990.

[15] S. Scherrer, *Synthesis, structure and properties of the organic-inorganic plastic crystal solid solution system $[(CH_2CH_3)_4]_x[(CH_3)_4]_{1-x}[FeCl_3Br]$*. M.S. thesis, Technische Universität Wien, 2020.

[16] J. W. Mullin, *Crystallization*. Butterworth-Heinemann, 2001, ch. 3: Solutions and solubility, pp. 123–125.

[17] J. W. Mullin, *Crystallization*. Butterworth-Heinemann, 2001, ch. 5: Nucleation.

[18] J. W. Mullin, *Crystallization*. Butterworth-Heinemann, 2001, ch. 6: Crystal growth.

[19] J. W. Mullin, *Crystallization*. Butterworth-Heinemann, 2001, ch. 1: The crystalline state.

[20] R. J. D. Tilley, *Understanding Solids: The Science of Materials*. John Wiley and Sons, 2004, ch. 7: Diffusion and ionic conductivity.

[21] A. R. West, *Solid state chemistry and its applications*, 2nd ed. John Wiley & Sons, 2014, ch. 4: Synthesis, processing and application methods.

[22] D. W. Richerson and W. E. Lee, *Modern ceramic engineering: properties, processing, and use in design*. CRC press, 2018.

[23] M. Lusi, 'Engineering crystal properties through solid solutions,' *Crystal Growth & Design*, vol. 18, no. 6, pp. 3704–3712, 2018.

[24] G. T. Desiraju, 'Crystal engineering: From molecule to crystal,' *J. Am. Chem. Soc.*, vol. 135, pp. 9952–9967, 2013.

[25] B. Viswanathan, *Structure and Properties of Solid State Materials*. Alpha Science, 2006.

[26] R. J. D. Tilley, *Understanding Solids: The Science of Materials*. John Wiley and Sons, 2004, ch. 11: Insulating Solids.

[27] L. Dissado, *Springer Handbook of Electronic and Photonic Materials*, 2nd ed., S. Kasap and P. Capper, Eds. Springer, 2017, ch. 10: Dielectric Response.

[28] H. Fröhlich, *Theory of Dielectrics*, 2nd ed. Clarendon Press, 1958.

[29] S. Trolier-McKinstry and R. E. Newnham, *Materials Engineering: Bonding, Structure, and Structure-property Relationships*. Cambridge University Press, 2018, ch. 28: Dielectrics and Ferroelectrics.

[30] K. M. Rabe, M. Dawber, C. Lichtensteiger, C. H. Ahn and J.-M. Triscone, 'Modern physics of ferroelectrics: Essential background,' *Physics of Ferroelectrics*, pp. 1–30, 2007.

[31] G. H. Haertling, 'Ferroelectric ceramics: History and technology,' *J. Am. Chem. Soc.*, vol. 82, no. 4, pp. 797–818, 1999.

[32] D. Damjanovic, 'Ferroelectric, dielectric and piezoelectric properties of ferroelectric thin films and ceramics,' *Reports on Progress in Physics*, vol. 61, no. 9, p. 1267, 1998.

[33] J. Guyonnet, *Ferroelectric Domain Walls*. Springer Theses, 2014.

[34] L. Jin, F. Li and S. Zhang, 'Decoding the fingerprint of ferroelectric loops: Comprehension of the material properties and structures,' in *Progress in Advanced Dielectrics*, World Scientific, 2020, pp. 21–104.

[35] Y. A. Genenko, J. Glaum, M. J. Hoffmann and K. Albe, 'Mechanisms of aging and fatigue in ferroelectrics,' *Materials Science and Engineering: B*, vol. 192, pp. 52–82, 2015.

[36] G. Helke and K. Lubitz, 'Piezoelectric PZT ceramics,' in *Piezoelectricity*, Springer, 2008, pp. 89–130.

[37] S. Hwang, C. Lynch and R. McMeeking, 'Ferroelectric/ferroelastic interactions and a polarization switching model,' *Acta Metallurgica et Materialia*, vol. 43, no. 5, pp. 2073–2084, 1995, issn: 0956-7151.

[38] B. Jaffe, W. R. Cook Jr. and H. Jaffe, *Piezoelectric Ceramics*. Academic Press, 1971.

[39] L. E. Cross, 'Ferroelectric materials for electromechanical transducer applications,' *Japanese journal of applied physics*, vol. 34, no. 5S, p. 2525, 1995.

[40] B. Noheda and D. Cox, 'Bridging phases at the morphotropic boundaries of lead oxide solid solutions,' *Phase Transitions*, vol. 79, no. 1-2, pp. 5–20, 2006.

[41] B. Noheda, D. Cox, G. Shirane, J. Gonzalo, L. Cross and S. Park, 'A monoclinic ferroelectric phase in the $Pb(Zr_{1-x}Ti_x)O_3$ solid solution,' *Applied physics letters*, vol. 74, no. 14, pp. 2059–2061, 1999.

[42] B. Noheda, D. Cox, G. Shirane, R. Guo, B. Jones and L. Cross, 'Stability of the monoclinic phase in the ferroelectric perovskite $Pb(Zr_{1-x}Ti_x)O_3$,' *Physical Review B*, vol. 63, no. 1, p. 014 103, 2000.

[43] J. Timmermans, 'Researches in stoichiometry. 1. heat of fusion of organic compounds,' *Bull. Soc. Chim. Belg.*, vol. 44, pp. 17–40, 1935.

[44] J. Timmermans, 'Plastic crystals: A historical review,' *J. Phys. Chem. Solids*, vol. 18, no. 1, pp. 1–8, 1961.

[45] R. Brand, P. Lunkenheimer and A. Loidl, 'Relaxation dynamics in plasic crystals,' *Journal of Chemical Physics*, vol. 116, no. 23, pp. 10 386–10 401, 2002.

[46] J. M. Pringle, P. C. Howlett, D. MacFarlane and M. Forsyth, 'Organic ionic plastic crystals: Recent advances,' *Journal of Materials Chemistry*, vol. 20, pp. 2056–2062, 2010.

[47] J. Golding, N. Hamid, D. R. MacFarlane, M. Forsyth, C. Forsyth, C. Collins and J. Huang, 'N-methyl-n-alkylpyrrolidinium hexafluorophosohate salts: Novel molten salts and plastic crystal phases,' *Chem. Mater.*, vol. 13, pp. 558–564, 2001.

[48] D. R. MacFarlane, P. Meakin, N. Amini and M. Forsyth, 'Structural studies of ambient temperature plastic crystal ion conductors,' *J. Phys: Condens. Matter*, vol. 13, pp. 8257–8267, 2001.

[49] J. Harada, T. Shimojo, H. Oyamaguchi, H. Hasegawa, Y. Takahashi, K. Satomi, Y. Suzuki, J. Kawamata and T. Inabe, 'Directionally tunable and mechanically deformable ferroelectric crystals from rotating polar globular ionic molecules,' *Nature chemistry*, vol. 8, pp. 946–52, 2016.

[50] J. Walker, S. Scherrer, N. S. Løndal, T. Grande and M.-A. Einarsrud, 'Electric field dependent polarization switching of tetramethylammonium bromotrichloroferrate (iii) ferroelectric plastic crystals,' *Applied Physics Letters*, vol. 116, no. 24, p. 242 902, 2020.

[51] K. Momma and F. Izumi, '*VESTA3* for three-dimensional visualization of crystal, volumetric and morphology data,' *Journal of Applied Crystallography*, vol. 44, no. 6, pp. 1272–1276, Dec. 2011. doi: 10.1107/S0021889811038970. [Online]. Available: https://doi.org/10.1107/S0021889811038970.

[52] J. Walker, Unpublished work at NTNU Plastic crystals group, 2021.

[53] Z. Warnke, E. Styczeń, D. Wyrzykowski, A. Sikorski, J. Kłak and J. Mroziński, 'Structural and physico-chemical characteristics of tetraethylammonium tetrachloridoferrate(iii),' *Struct. Chem.*, vol. 21, pp. 285–289, 2010.

[54] M. Lutz, Y. Huang, M.-E. Moret and R. J. M. Klein Gebbink, 'Phase transitions and twinned low-temperature structures of tetraethylammonium tetrachloridoferrate(iii),' *Acta. Cryst.*, vol. 70, pp. 470–476, 2014.

[55] K. Ben Brahim, M. Ben Gzaiel, A. Oueslati and M. Gargouri, 'Electrical conductivity and vibrational studies induced phase transitions in $[(C_2H_5)_4N]FeCl_4$,' *RSC Adv.*, vol. 8, pp. 40 676–40 686, 2018.

[56] C. A. Clausen and M. L. Good, 'Mössbauer and far-infrared studies of tetrahaloferrate anions of the type $FeCl_{4-n}Br_n^-$,' *Inorganic Chemistry*, vol. 9, no. 2, pp. 220–223, 1970.

[57] H. Moriwake, A. Konishi, T. Ogawa, K. Fujimura, C. A. Fisher, A. Kuwabara, T. Shimizu, S. Yasui and M. Itoh, 'Ferroelectricity in wurtzite structure simple chalcogenide,' *Applied Physics Letters*, vol. 104, no. 24, p. 242 909, 2014.

[58] D. H. Aue, H. M. Webb and M. T. Bowers, 'A thermodynamic analysis of solvation effects on the basicities of alkylamines. an electrostatic analysis of substituent effects,' *Journal of the American Chemical Society*, vol. 98, no. 2, pp. 318–329, 1976.

[59] N. S. Løndal, *Effects of material structure on the electrical properties of ferroelectric plastic crystal tetramethylammonium bromotrichloroferrate(III)*. M.S. thesis, NTNU, 2020.

[60] H. G. Yeo, T. Xue, S. Roundy, X. Ma, C. Rahn and S. Trolier-McKinstry, 'Strongly (001) oriented bimorph pzt film on metal foils grown by rf-sputtering for wrist-worn piezoelectric energy harvesters,' *Advanced Functional Materials*, vol. 28, no. 36, p. 1 801 327, 2018.

[61] M. Deluca, 'Microscopic texture characterisation in piezoceramics,' *Advances in Applied Ceramics*, vol. 115, no. 2, pp. 112–122, 2016.

Appendix A

X-ray diffractograms

In this appendix, X-ray diffractograms of all powder samples (C-100 to C-70) as well as pressed samples (P-100 to P-70) can be found. In the diffractograms, observed data is plotted together with the calculated fit from the Rietveld refinement. Differences between observed data and calculated fits are also included.

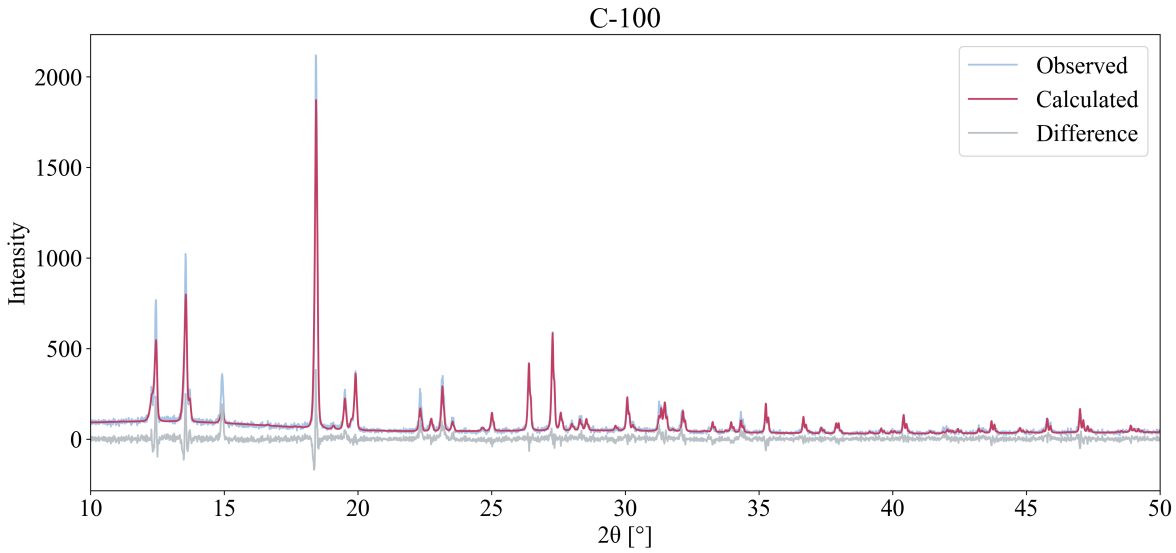

Figure A.1: X-ray diffractogram of C-100.

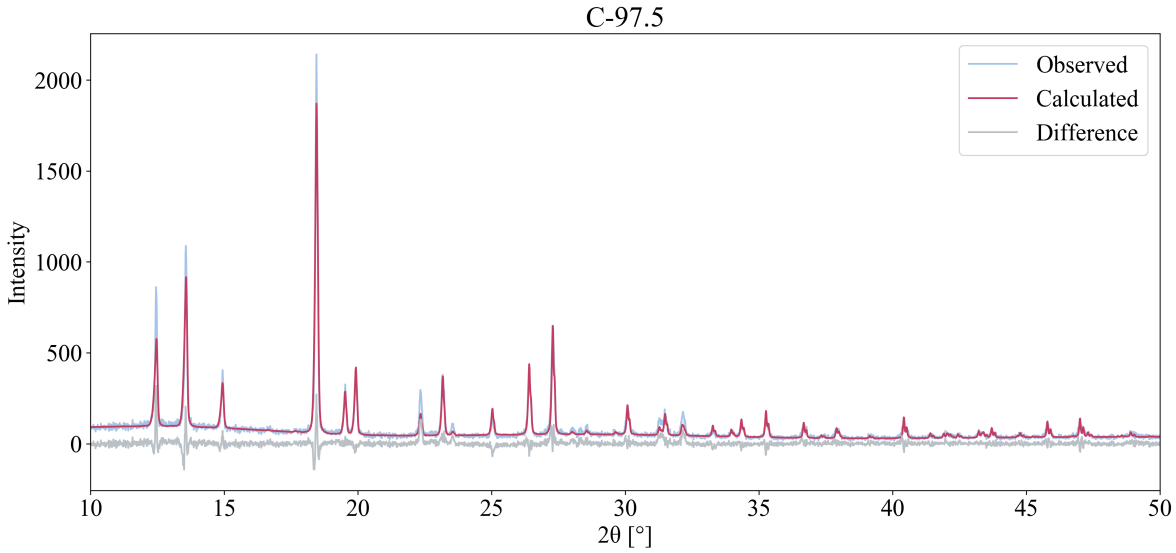

Figure A.2: X-ray diffractogram of C-97.5.

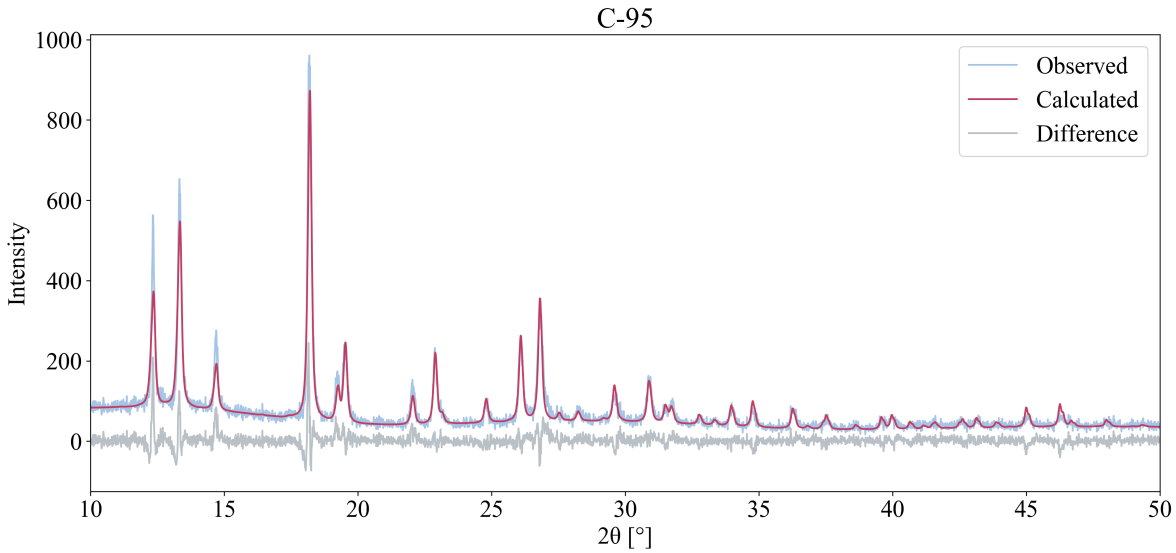

Figure A.3: X-ray diffractogram of C-95.

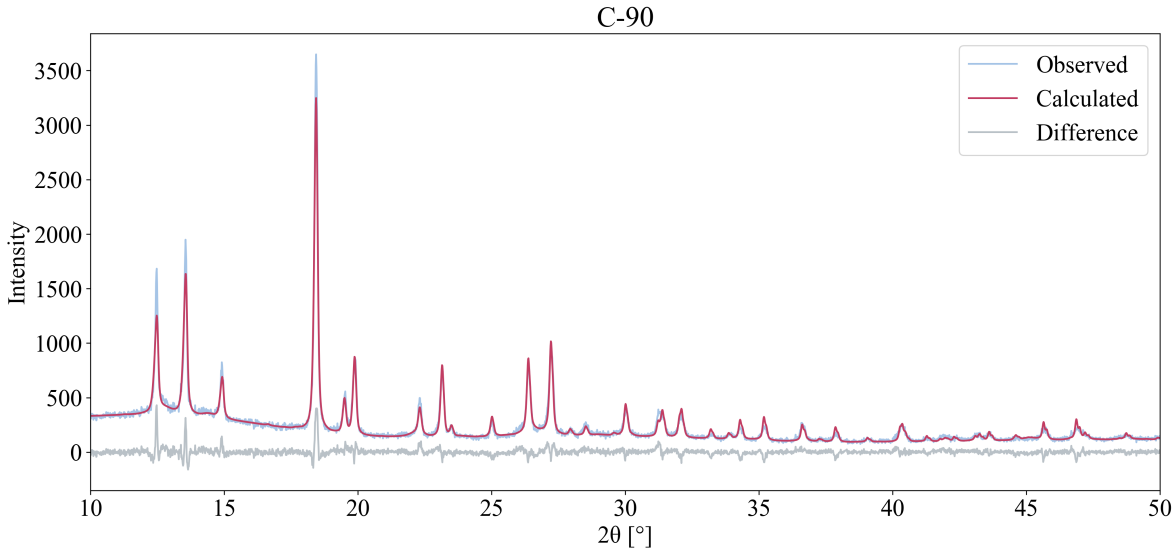

Figure A.4: X-ray diffractogram of C-90.

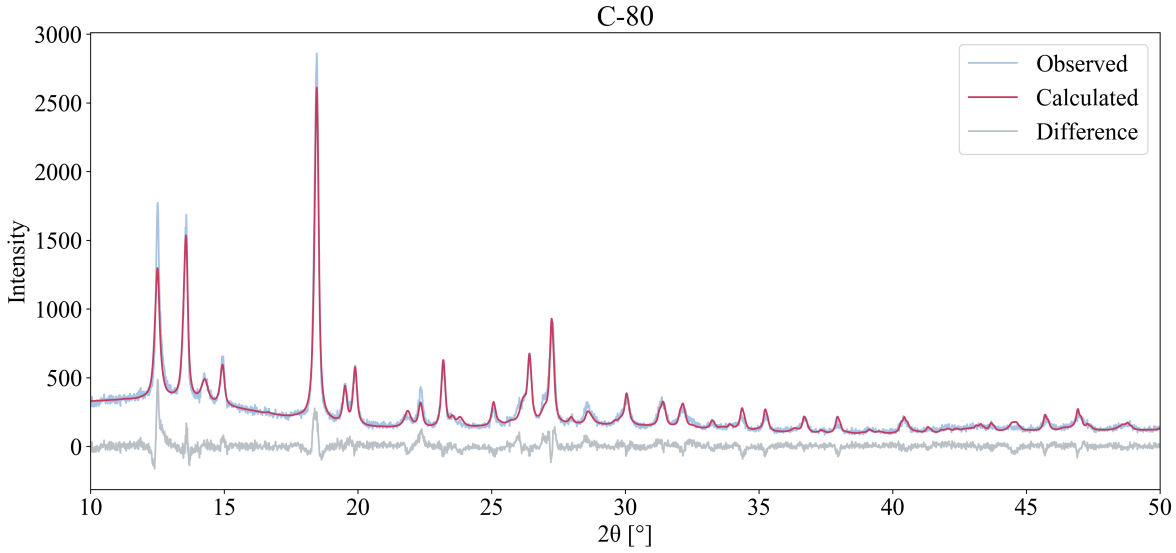

Figure A.5: X-ray diffractogram of C-80.

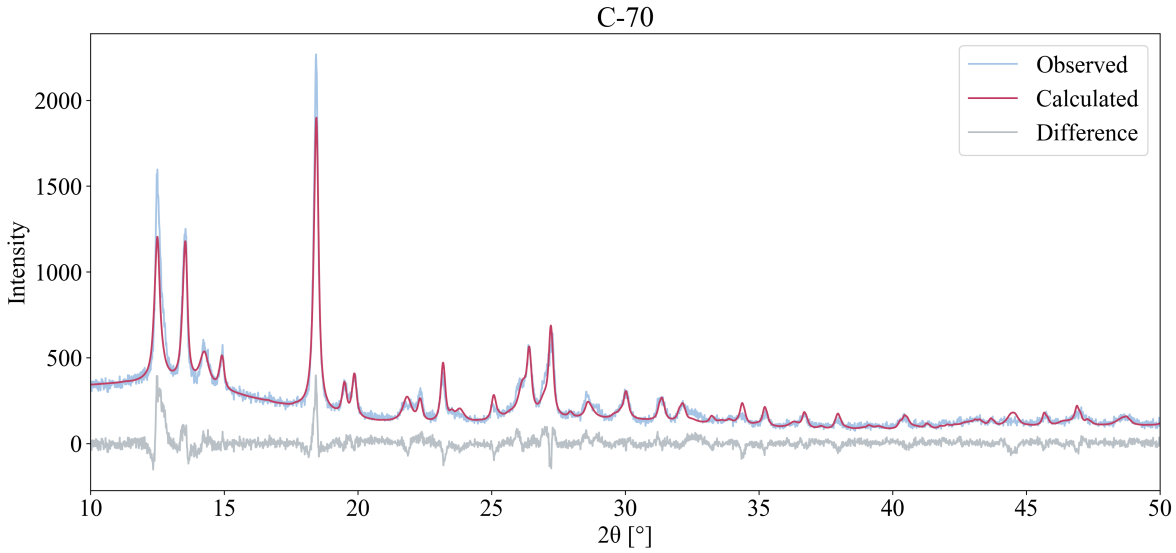

Figure A.6: X-ray diffractogram of C-70.

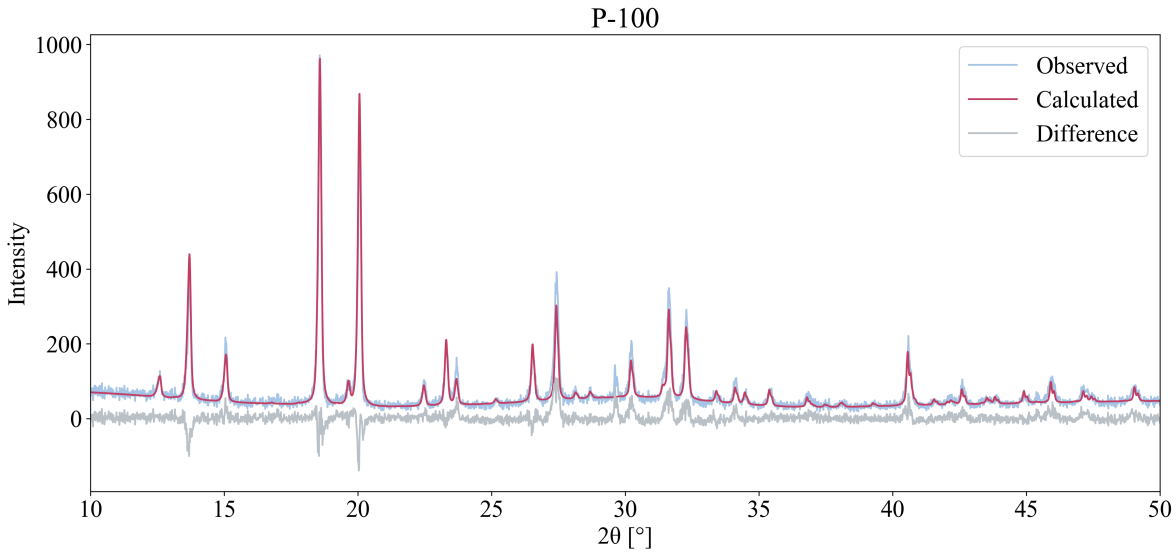

Figure A.7: X-ray diffractogram of P-100.

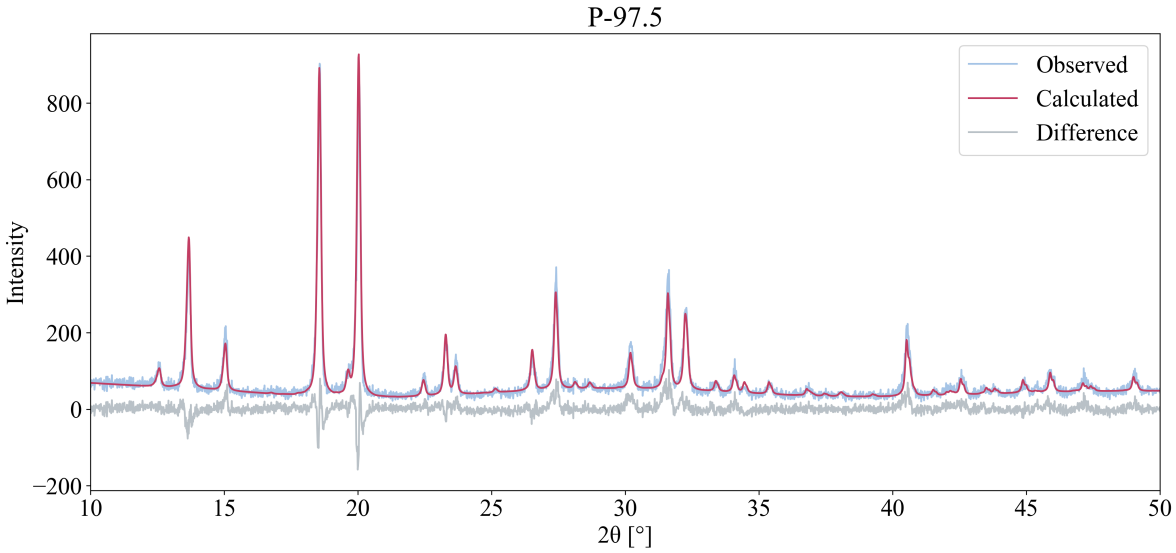

Figure A.8: X-ray diffractogram of P-97.5.

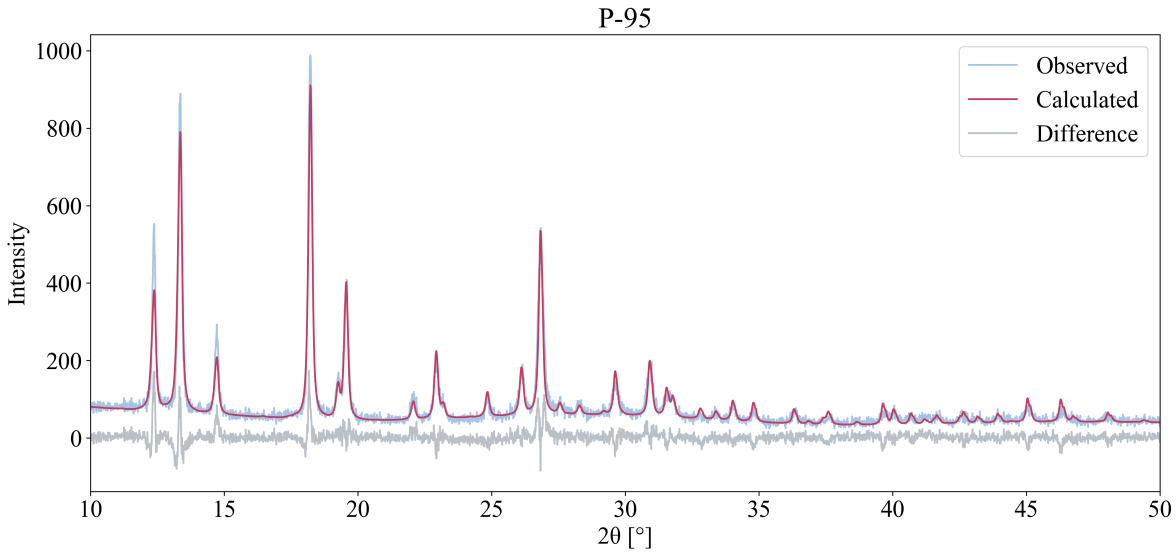

Figure A.9: X-ray diffractogram of P-95.

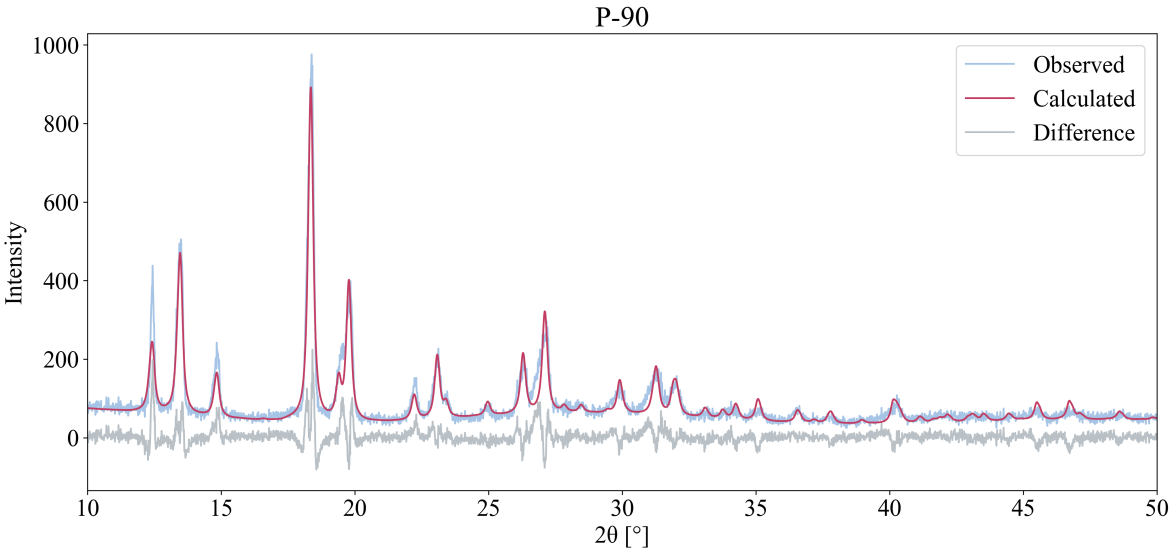

Figure A.10: X-ray diffractogram of P-90.

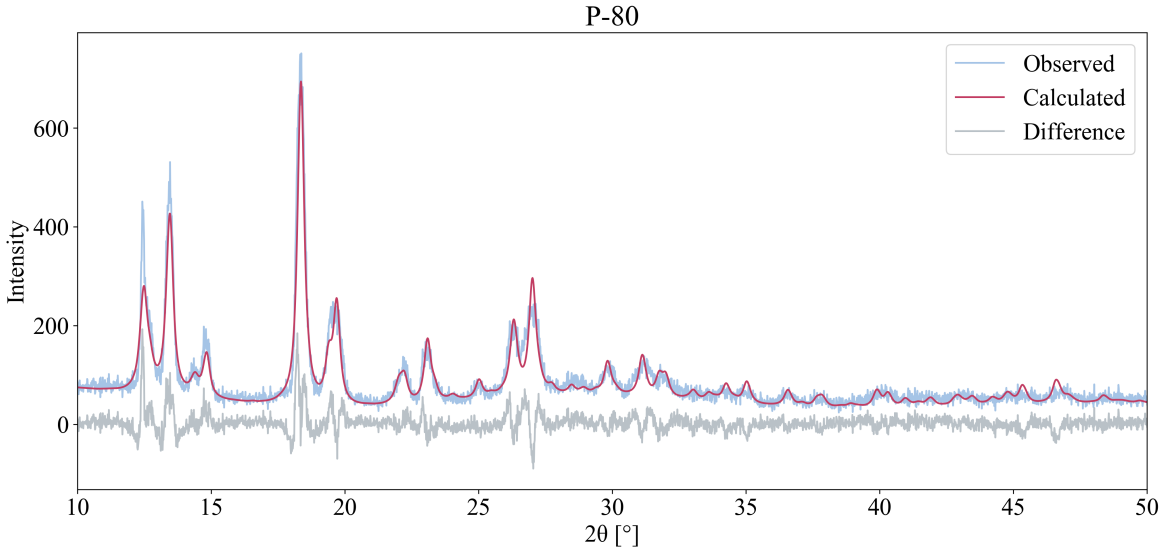

Figure A.11: X-ray diffractogram of P-80.

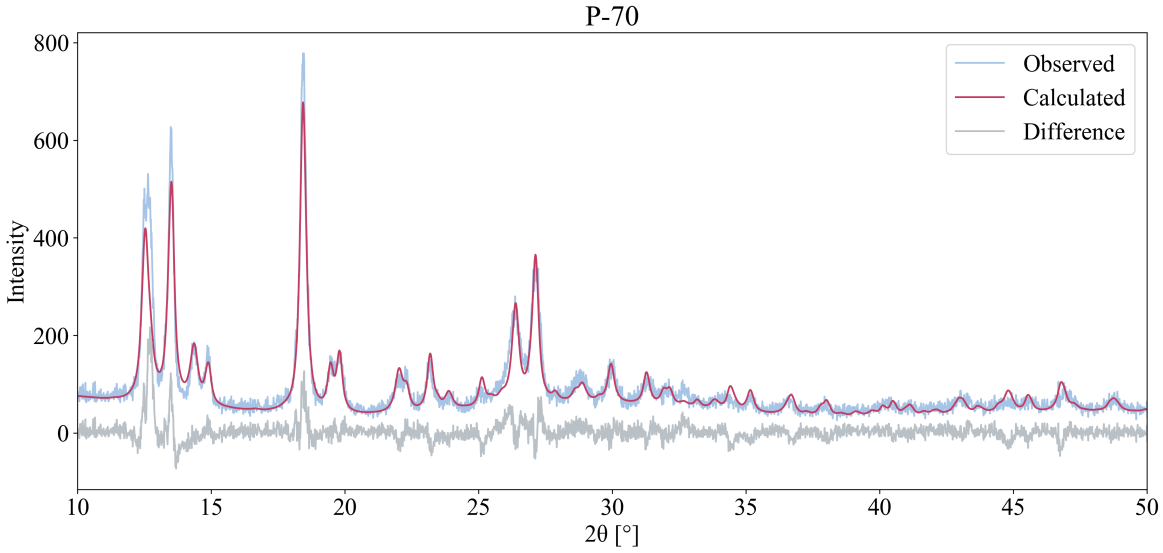

Figure A.12: X-ray diffractogram of P-70.

Appendix B

Malfunctioning DSC temperature programs

Due to instrument malfunctions, the cooling rate was not maintained during the thermal cycling programs. Instead, the rate slowed down as the temperature was decreased. Furthermore, negative temperatures could not be achieved. In this Appendix, the temperature programs experienced are included to give the reader a better understanding of how this malfunction prohibited the collection of physical data. The intended temperature program is also included once again for reference, and is found also in Section 3.

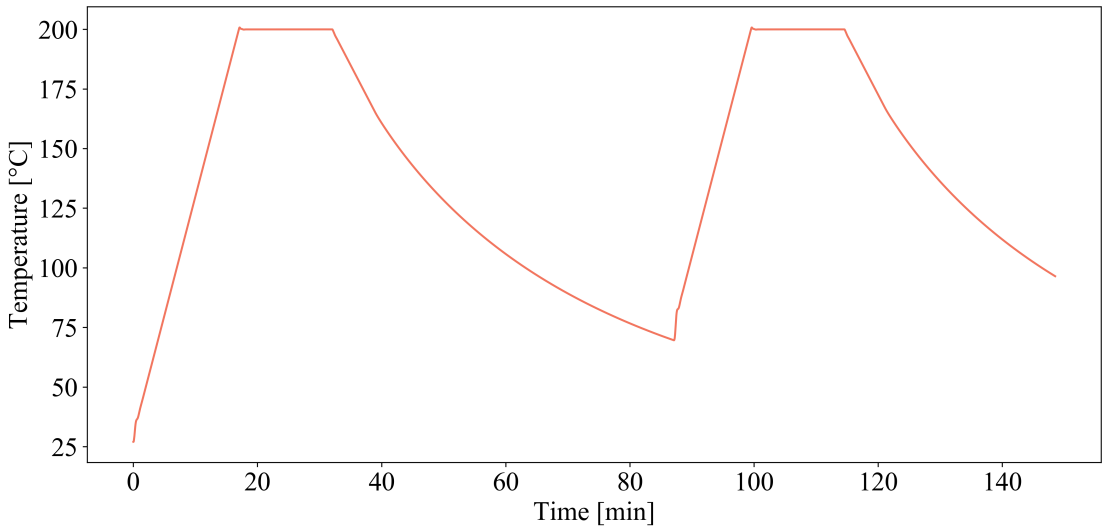

Figure B.1: Observed temperature program between 35 and 200 °C. The cooling rate was not maintained but slowed down when the temperature was lowered.

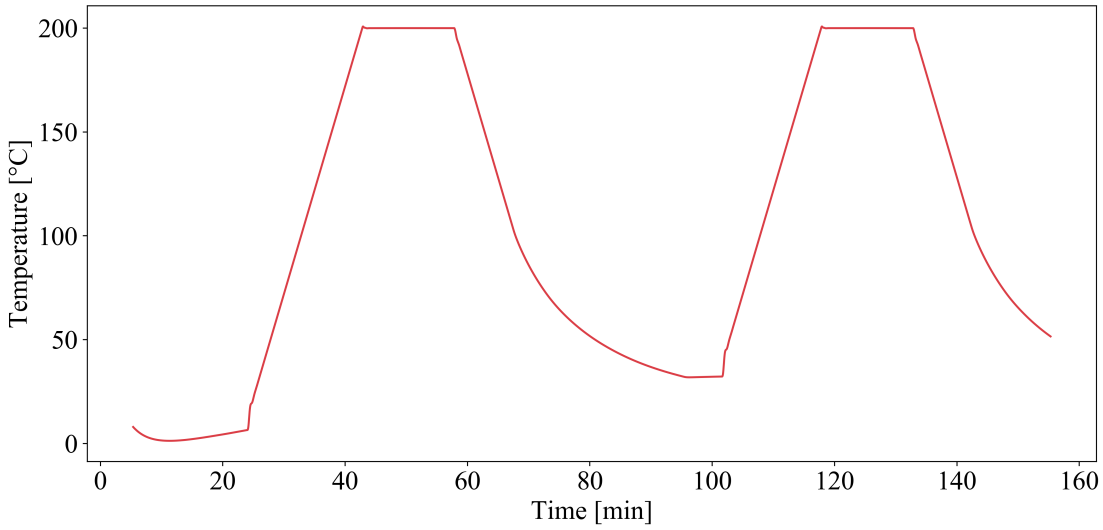

Figure B.2: Experienced temperature program supposed to have gone between -25 and 200 °C. The cooling rate slowed down and negative temperatures could not be achieved.

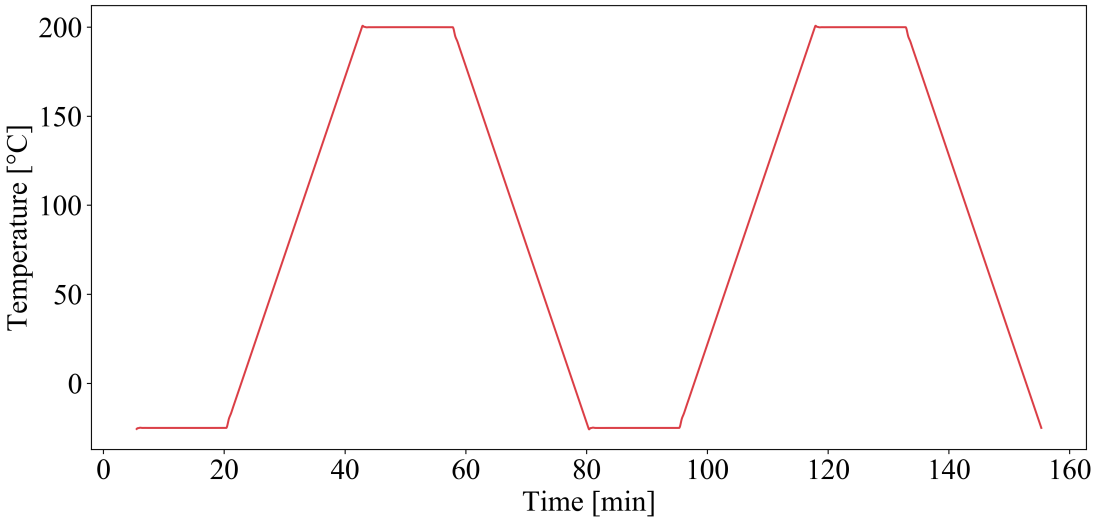

Figure B.3: Intended temperature program between -25 and 200 °C. Here the rate is constant throughout the cooling processes.

Appendix C

High-field electrical data

Here, polarisation-electric field, current density-electric field and strain-electric field data is presented for the P-95, P-90, P-80 and P-70 samples.

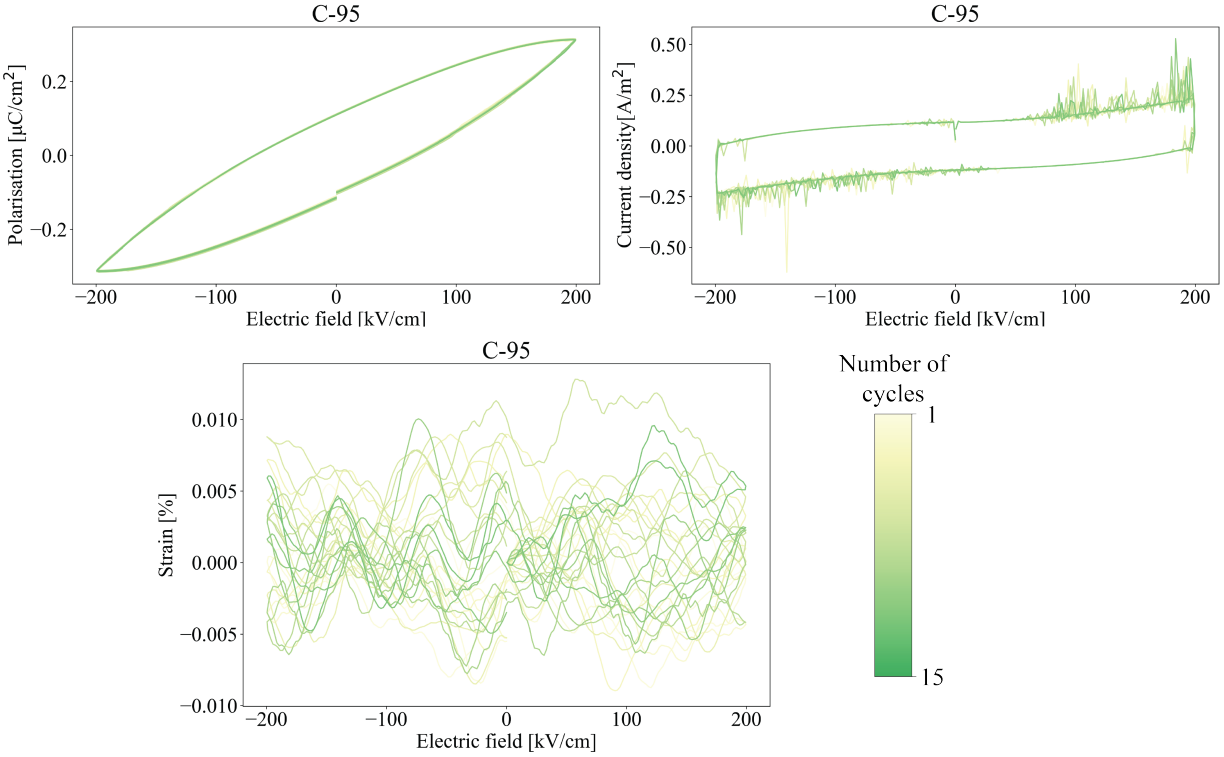

Figure C.1: P-E, J-E and S-E data for P-95 at 200 kV/cm.

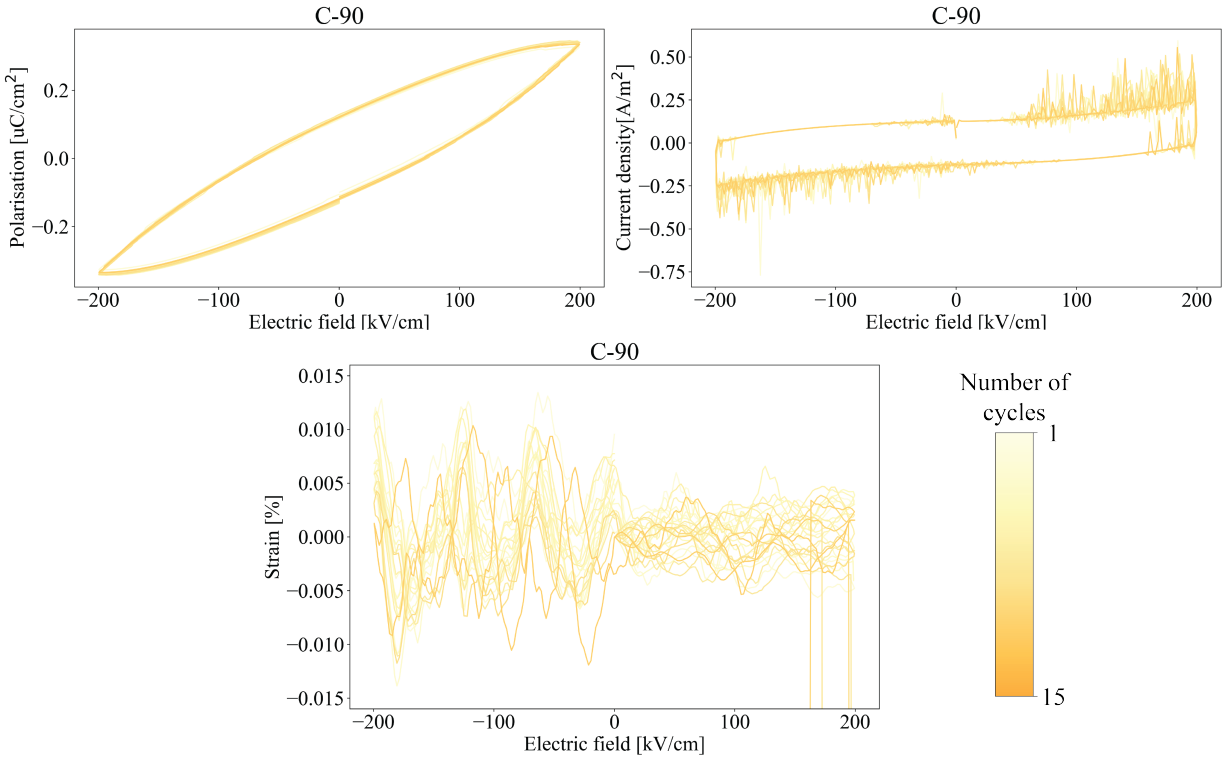

Figure C.2: P-E, J-E and S-E loops for P-90 at 200 kV/cm.

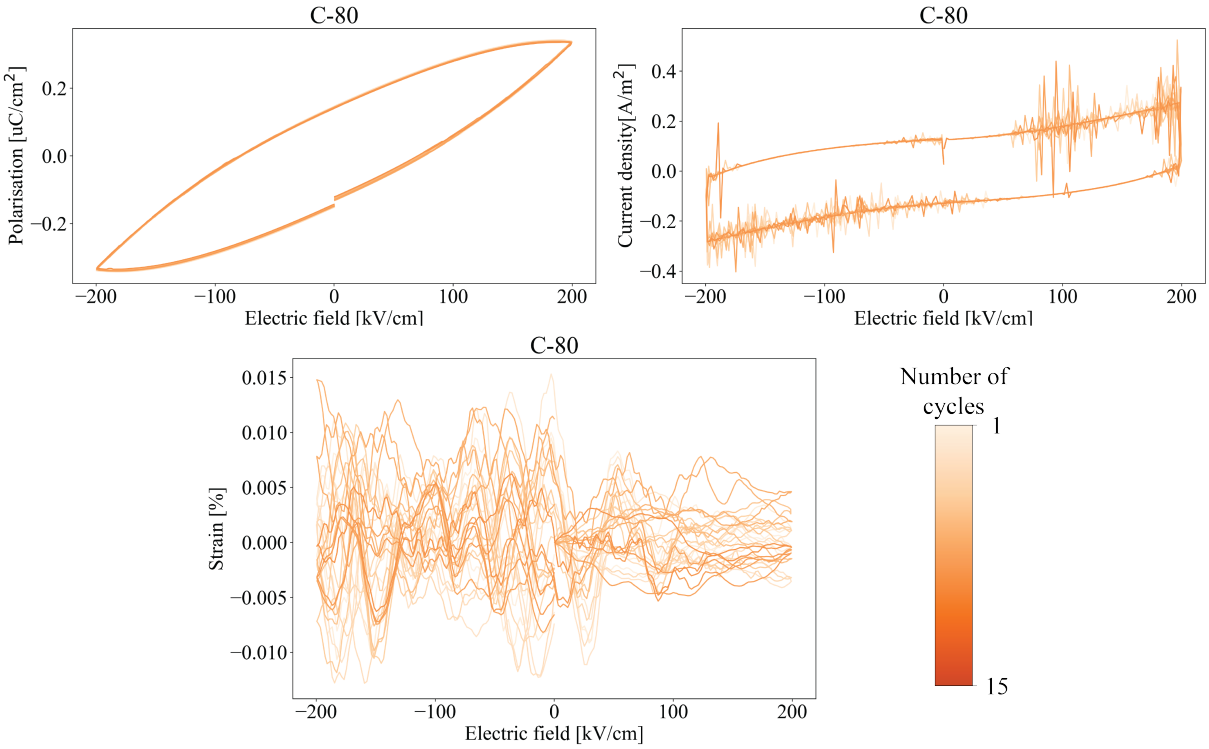

Figure C.3: P-E, J-E and S-E data for P-80 at 200 kV/cm.

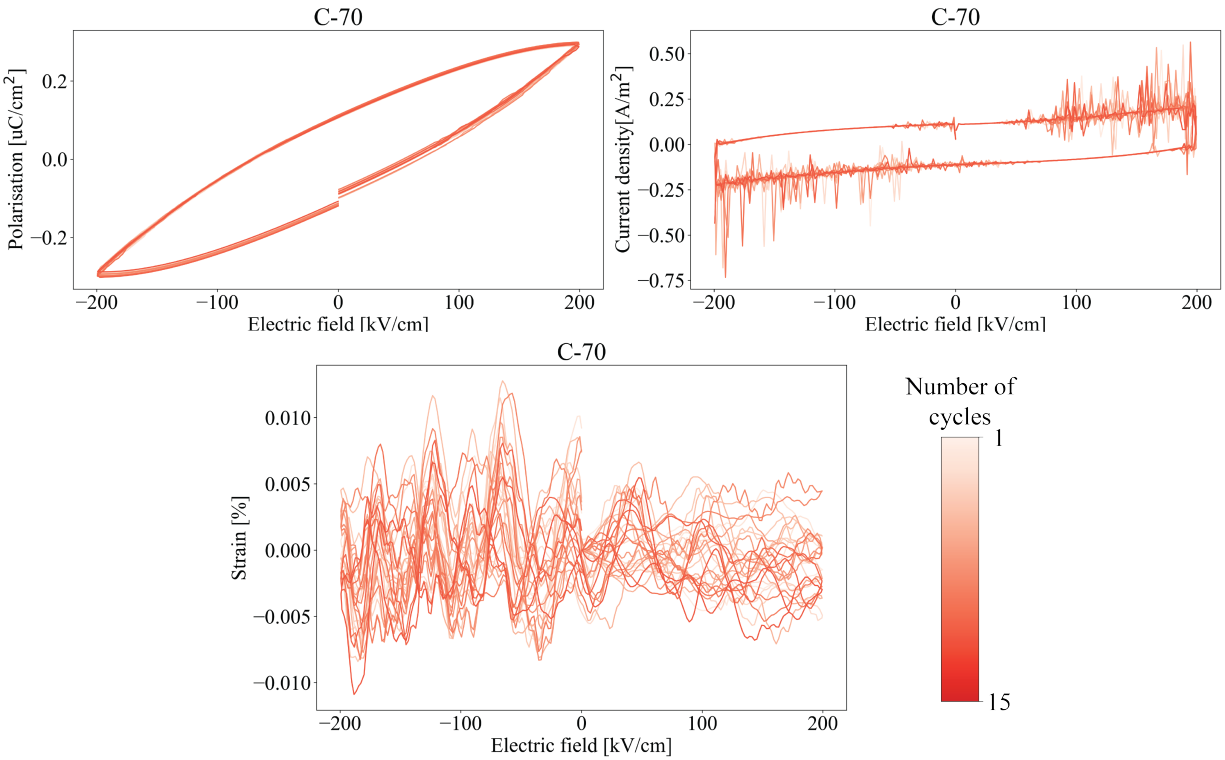

Figure C.4: P-E, J-E and S-E data for P-70 at 200 kV/cm.

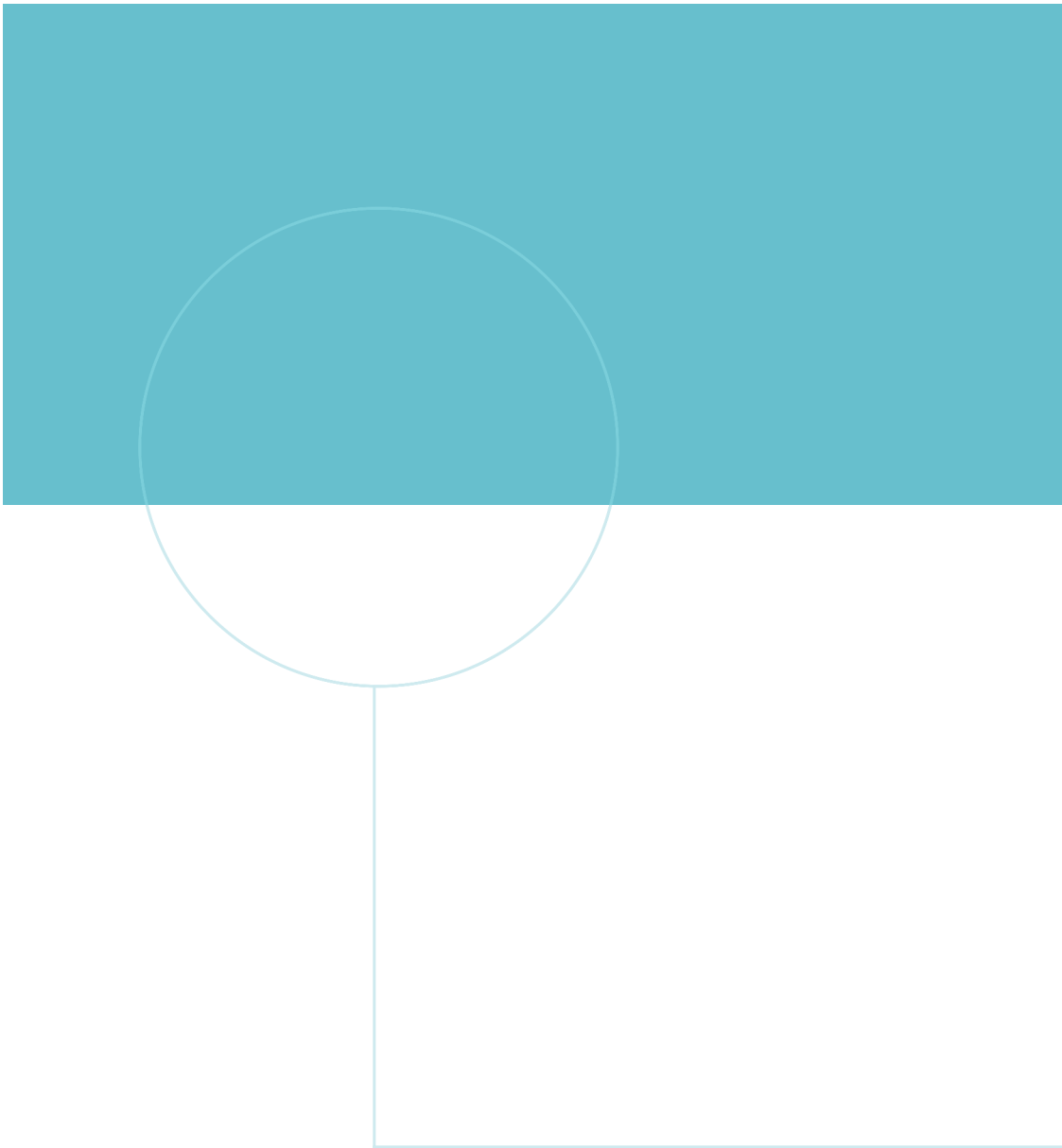

NTNU

Norwegian University of
Science and Technology